Dissertation

submitted to the
Combined Faculty of Natural Sciences and Mathematics
of the Ruperto Carola University Heidelberg, Germany
for the degree of
Doctor of Natural Sciences

Presented by
M.Sc. Martin Zauser
born in Ravensburg
Oral examination on July 26, 2021

Communication in Plants: Analysis and Modeling of Calcium Signatures in *Arabidopsis thaliana*

Referees: Prof. Dr. Ursula Kummer

Dr. Jürgen Pahle

"Imagination is more important than knowledge. For knowledge is limited to all we now know and understand, while imagination embraces the entire world, and all there ever will be to know and understand."

Albert Einstein

"Essentially, all models are wrong, but some are useful."

George Edward Pelham Box

Summary

Plants have a sessile lifestyle and cannot run away when attacked. They have therefore developed various defense systems to deal with potential predators or bacteria and fungi. But heat, drought or high concentrations of salt in the water also mean stress for the plant. Calcium plays an important role as a signaling molecule in the transmission of the stress stimulus within the plant. Plants of the species *Arabidopsis thaliana* can be genetically modified so that their calcium concentration is visible under the microscope. These plants were stimulated by my cooperation partners with various biotic and abiotic stress stimuli and recorded with the camera. As a response, the time-lapse recordings show a locally limited increase in the intracellular calcium concentration close to the root tip, which runs in waves through the plant. The aim of my work was to analyze the wave qualitatively and quantitatively and to investigate the connection between the type of stimulus and the spatio-temporal pattern of the wave, the calcium signature. By means of modeling, I investigated how this wave can propagate at high speed across cell boundaries and how different responses to a calcium signal can be triggered at the protein level.

The course of the calcium wave can be displayed as a kymograph, a space-time diagram. Using the kymograph, I managed to quantify the wave and to determine characteristic parameters such as start time, start position, and speed. The image series of the individual experiments show a high variance with respect to intensity and shape of the calcium wave. To the purpose of convenient evaluation, I designed an analysis script that quantifies the calcium wave automatically. Firstly, the root is detected in an image series. Secondly, a kymograph is created from the mean calcium concentration along the root. Finally, the calcium wave is plotted as a thin, sharply outlined line. This so-called crestline plot highlights the characteristic properties of the individual wave and allows an easy approximation of aforementioned wave parameters. The analysis of the experiments revealed that stimulation with salt leads to an immediate, short-term increase in the calcium concentration, while bacteria or fungi trigger a delayed calcium wave that propagates at a speed of a few µm/s.

It is known from the literature that after stimulation of the root with elevated levels of salt, the wave moves through the plant at a high speed of around 400 µm/s. A combined signal transmission of intracellular calcium and extracellular reactive oxygen species (ROS) is suggested as a possible explanation. Together with my cooperation partner, I designed a corresponding mathematical model and adapted it to the different cell sizes in the root tip. We were able to show that wave propagation based only on intracellular calcium is sufficient for the much slower calcium wave after stimulation with bacteria or fungi. However, the calcium wave after stimulation with salt requires additional components. Based on a simulation, I was able to demonstrate that the plasmodesmata, the narrow tubes between adjacent cells, slow down the expansion of the wave considerably and should not be ignored.

The plant can use calcium-dependent protein kinases (CPKs) to decode the calcium signal and translate it into protein phosphorylations as a starting point for further reactions. For example, the closing process of the stomata is based on the calcium-regulated activation of CPKs. Based on experimental data, I developed a CPK protein model for different CPKs. In a computer simulation, I coupled calcium time series from a stimulation experiment of guard cells and epidermal cells to my protein model and examined the activity of the CPK proteins. I was able to show that by varying the calcium signal, different CPK proteins can be addressed and the stress response of the plant can be adapted to the type of stimulation.

Zusammenfassung

Pflanzen pflegen einen sesshaften Lebensstil und können nicht einfach weglaufen, wenn Sie angegriffen werden. Sie haben daher verschiedene Abwehrsysteme entwickelt, um mit potentiellen Fressfeinden oder Bakterien und Pilzen fertig zu werden. Aber auch Hitze, Trockenheit oder hoher Salzgehalt des Wassers bedeuten Stress für die Pflanze. Bei der Weiterleitung des Stressreizes innerhalb der Pflanze spielt Calcium als Signalmolekül eine wichtige Rolle. Pflanzen der Art *Arabidopsis thaliana* können genetisch so modifiziert werden, dass ihre Calciumkonzentration unter dem Mikroskop sichtbar ist. Diese Pflanzen wurden von meinen Kooperationspartnern mit verschiedenen biotischen und abiotischen Stressreizen stimuliert und dabei mit der Kamera aufgezeichnet. Die Zeitrafferaufnahmen zeigen als Reaktion einen lokal begrenzten Anstieg der intrazellulären Calciumkonzentration nahe der Wurzelspitze, welcher wellenartig durch die Pflanze läuft. Ziel meiner Arbeit war es, die Welle qualitativ und quantitativ zu analysieren und einen möglichen Zusammenhang zwischen der Art des Stressreizes und dem räumlich-zeitlichen Muster der Welle, der sogenannten Calcium-Signatur, zu erforschen. Mittels Modellierung untersuchte ich, wie sich diese Welle mit hoher Geschwindigkeit über Zellgrenzen hinweg ausbreiten kann und wie auf Proteinebene unterschiedliche Reaktionen auf ein Calciumsignal ausgelöst werden können.

Der Verlauf der Calciumwelle kann als Kymograph, als Raum-Zeit-Diagramm, dargestellt werden. Mittels computergestützter Auswertung des Kymographen war es mir möglich, die Welle zu quantifizieren und charakteristische Kenngrößen wie Startzeitpunkt, Startposition und Geschwindigkeit zu bestimmen. Die Bilderserien der einzelnen Experimente weisen eine hohe Varianz bezüglich Intensität und Erscheinungsbild der Calciumwelle auf. Um deren Auswertung zu erleichtern, habe ich ein Analyseskript entwickelt, das die Quantifizierung der Calciumwelle vollautomatisch durchführt. Dabei wird zunächst die Wurzel in den Bilderserien detektiert, aus der mittleren Calciumkonzentration entlang der Wurzel ein Kymograph erstellt und darin dann die Calciumwelle als dünne scharf umrissene Linie eingezeichnet. Dieser sogenannte Crestline-Plot macht die charakteristischen Eigenschaften der einzelnen Welle deutlich und erlaubt eine einfache Abschätzung der oben erwähnten Kenngrößen. Die Analyse der Experimente ergab, dass Stimulation mit Salz zu einer sofortigen kurzzeitigen Erhöhung der Calciumkonzentration führt, während Bakterien oder Pilze eine Calciumwelle auslösen, die mit Verzögerung einsetzt und sich mit einer Geschwindigkeit von wenigen µm/s ausbreitet.

Aus der Literatur ist bekannt, dass sich die Welle nach Stimulation der Wurzel durch eine Erhöhung der Salzkonzentration mit einer Geschwindigkeit um die 400 µm/s durch die Pflanze fortbewegt. Als mögliche Erklärung wird eine kombinierte Signalweiterleitung aus intrazellulärem Calcium und extrazellulären Reactive Oxygen Species (ROS) genannt. Zusammen mit meinem Kooperationspartner habe ich ein entsprechendes mathematisches Modell erstellt und an die unterschiedlichen Zellgrößen in der Wurzelspitze angepasst. Wir konnten zeigen, dass eine nur auf intrazellulärem Calcium basierende Signalweiterleitung für die wesentlich langsamere Calciumwelle nach Stimulation mit Bakterien oder Pilzen ausreichend ist während die Calciumwelle nach Stimulation mit Salz die Einbeziehung zusätzlicher Komponenten erfordert. Mittels Computersimulation konnte ich demonstrieren, dass die Plasmodesmata, die schmalen Verbindungsgänge zwischen benachbarten Zellen, die Ausbreitung der Welle erheblich bremsen und nicht vernachlässigt werden dürfen.

Die Dekodierung des Calciumsignals und dessen Übersetzung in Proteinphosphorylierungen als Ausgangspunkt für weitere Reaktionen kann in der Pflanze durch Calcium-abhängige Proteinkinasen, sogenannte CPKs, erfolgen. Zum Beispiel basiert der Schließvorgang der Spaltöffnungen auf der Calcium-gesteuerten Aktivierung von CPKs. Auf der Grundlage von experimentellen Daten aus der Literatur habe ich ein CPK-Proteinmodell für verschiedene CPKs entwickelt. In einer Computersimulation habe ich Calcium-Zeitreihen aus einem Stimulationsexperiment von Schließzellen und Epidermiszellen an mein Proteinmodell gekoppelt und die Aktivität der CPK-Proteine untersucht. Ich konnte zeigen, dass durch Variierung des Calcium-Signals unterschiedliche CPK-Proteine angesprochen werden können und damit die Stressantwort der Pflanze auf die Art der Stimulierung abgestimmt werden kann.

Acknowledgments

I would like to thank Prof. Dr. Ursula Kummer and Dr. Jürgen Pahle for their support and supervision of my thesis. In particular, I thank Dr. Jürgen Pahle for his great encouragement and guidance of this project. I would also like to thank the other two members of the defense committee, Dr. Frederik Graw and Prof. Dr. Thomas Greb, for their effort and time.

My thanks also go to my two mentors, Dr. Sarah Kaspar and Dr. Irina Surovtsova, who gave me great support.

I want to thank all members of the Biological Information Processing Group at Heidelberg University for their support and advice. Dr. Guido Grossmann, Dr. Rik Brugman and Janos Löffler from the Centre for Organismal Studies Heidelberg provided me excellent support with the lab stuff. Rik is the great expert on the *Arabidopsis* experiments and knows best how to interpret a result. Janos supported me a lot with the coding and testing of the models.

A very special thank you goes to Dr. Arne Schoch, my fellow student and work group colleague, who always supported me morally and technically and without whose really outstanding support I would not have been able to finish this work.

I would like to say thank you very much to Dr. Irina Surovtsova, who was a very valuable help to me and actively supported me in completing my thesis.

I am also very grateful to Dr. Ruth Großeholz, who always supported me with ideas and her vast wealth of experience in plant research.

Finally, I thank my colleagues Sirac Baz, Jonas Förster, Nicolas Huber, Anika Liu, Janos Löffler and Michael Zengerling for their great ideas and fruitful discussions and for providing important input.

Contributions

The best and most sophisticated computer simulation is useless if it is not based on real world data. With this in mind, I consider myself very lucky that several wet labs provided me with data for my thesis. I am deeply indebted to Dr. Guido Grossmann and his team, who invested a lot of time and energy in microscopic examination of *Arabidopsis* seedlings under various biological conditions. Guido's lab in Heidelberg was just a stone's throw away from my office and we often met and exchanged views on the subject. The time-lapse image series from Guido and his team members Dr. Rik Brugman and Janos Löffler are the source on which my doctoral thesis is largely based (Rik has now completed his PhD thesis, Janos his master's thesis and Guido has accepted a full professorship at Heinrich Heine University in Düsseldorf). Rik did a lot of the microscopy tasks (Janos as well) and Janos wrote the code for the simulation of the combined calcium and ROS model under my guidance. In addition to the manual evaluation of the images, Rik had already coded a partially automated analysis using ImageJ/Fiji scripting, which I was allowed to use as a reference for my fully automatic analysis of the images in MATLAB and later in R. The image series from Guido's laboratory host a wealth of biological information. I devoted a large part of my work to analyzing these images. First I tried to evaluate the images as accurately as possible and to convert pixels into mathematical formulas. This is not always easy with biological material - not only because of the measurement uncertainties of the microscope and the restrictions, that highly magnified images bring with them, or the fact that untreated calcium ions are actually not visible and can only be made visible thanks to the R-GECO1-sensor, but also due to the natural variations that living organisms bring with them. The main difficulty was to extract useful values from the images. For this I developed the so-called crestline algorithm. And in order to evaluate the data as objectively as possible, I designed a pipeline for automatic image evaluation.

From the laboratory of Dr. Melanie Krebs in Heidelberg I got the calcium time series data from stimulated guard cells and epidermal cells, which she had already published in a figure in her publication (Keinath et al., 2015) and which I was allowed to use as raw data input for my computational models of CPK proteins. With kind permission of Dr. Dietmar Geiger in Würzburg I could use the in vitro kinase assay data of CPK proteins from his publication (Geiger et al., 2010)
In my work, I first created a mathematical model from the steady-state data, in which the CPK activity is approximated as a function of the calcium concentration by means of a Hill curve, and then ran simulations using a computational mass-reaction-based model. I also showed how the dynamics of CPK-activation could look like and I outlined possible downstream effects of a calcium-triggered signaling cascade with respect to the differential regulation of CPK proteins. Finally, I combined both data sets, the calcium data from Dr. Melanie Krebs and the CPK data from Dr. Dietmar Geiger, and investigated the extent of the calcium-mediated activation of the CPK proteins.

Contents

I Introduction

1 Introduction

1.1 Communication in plants

1.1.1 Interactions of plants with their environment

Plants are living organisms which comprise about 391,000 species and involve a biomass of around 450 Gigatons of carbon worldwide (Barker et al., 2016; Bar-On et al., 2018). The kingdom of plants covers a large variety of organisms including lower species like green algae, hornworts and mosses. However, if we speak of plants in a general sense we mostly refer to the recent species of the seed plants. Most species form multicellular photosynthetic organisms with a complex morphological structure and highly organized molecular networks.

Plants interact with their environment in multiple ways. They take up carbon dioxide and consume sunlight and release oxygen in return. Additionally, they consume a lot of nutrients like nitrogen, potassium and phosphor which they mainly extract from the soil. To ensure a constant supply with nutrients and energy, plants have evolved different strategies for finding nutrients and optimizing supply. The need for presenting a large surface to collect light resulted in a sessile lifestyle of the plants. Since they cannot move, it is quite important for them to quickly adapt to changing environmental conditions (Bohnert et al., 1995; Lawlor, 2011; Lamers et al., 2020). Plants are able to deal with heat, cold, drought and salinity by sophisticated mechanisms, they grow into the direction of light and spread their roots into the direction of increasing concentration of nutrients (Darwin, 1880; Pedmale et al., 2010; Gruber et al., 2013; Giehl and Wirén, 2014). Elastic shoots and branches guarantee high flexibility even if large vents or snowstorms hit the plants (Read and Stokes, 2006; Gardiner et al., 2016). Producing unsaturated fatty acids prevents cellular fluids from getting frozen (Wardlaw, 1972; He and Ding, 2020). For improving the uptake of nitrogen, some plants collaborate with bacteria or fungi in a symbiosis or attract insects to digest animal proteins (Nap and Bisseling, 1990; Adamec, 1997; Płachno et al., 2009; Soto et al., 2011).

1.1.2 Stress response in plants

If the environmental conditions of a plant deviate above or below the optimal range for a longer period of time, we speak of plant stress. Stress can be caused by abiotic factors like light, water and temperature and biotic factors like animals, microbians and herbal parasites (Balachandran et al., 1997; Zhu, 2016; Lamers et al., 2020). The most common abiotic stress factors are a shortage of light or water. Similarly, too much water, extreme temperatures, ultraviolet radiation or salinity as well as mechanical forces, e.g. caused by storms, can damage the plant. In contrast, biotic stress factors range from large herbivorous mammals to insects, right down to bacteria, fungi and plant viruses that colonize the plant in large numbers and extract sugar or other nutrients or even need the plant as a host for reproduction.

In the course of evolution, plants have developed a wide variety of mechanisms to cope with stress (He et al., 2018; Isah, 2019; Gong et al., 2020). The stress response of the plants consists of several lines of defense and involves many metabolic and morphological adaptations. In addition to permanently installed preventive passive mechanisms that defy the rigors of the weather and prevent animal enemies from eating the plant, there is also an active defense of the plant, which is activated as soon as an attack is detected (Howe and Jander, 2008; War et al., 2012; Xiao et al., 2019).

One of the most important preventive adaptations to harsh climates is protection against water loss and protection against frost (Scarth and Levitt, 1937; Beck et al., 2004; Ding et al., 2019). Large parts of the plants, that are exposed to the air, such as leaves, are often covered with a thin protective layer to prevent dehydration (Yeats and Rose, 2013). As for the liquid cell compartments, they are also supported by soluble compounds like sucrose, oligosaccharides, polyamines and others to develop stress tolerance against drought and cold (Krasensky and Jonak, 2012; Nägele and Heyer, 2013). Plants can also protect themselves against potential predators. Some plants store bitter substances in their cells, which make the plants uneatable, while others protect themselves through mechanical defense systems such as spines or thorns (Bennett and Wallsgrove, 1994; Hanley et al., 2007; Erb and Kliebenstein, 2020).

The active defense of plants consists of a sophisticated alarm system that responds to locally applied biotic or abiotic stress by generating a secondary systemic response which affects all parts of the plant (Hutcheson, 1998; Heil and Ton, 2008). Biotic stress triggers the systemic acquired resistance which is similar to the innate immune system in animals and stimulates the plant to prepare for defence against the pathogens (Ryals et al., 1996; Conrath, 2006; Vlot et al., 2021). Plants use pattern-recognition receptors to detect evolutionary conserved microbial structures which trigger a systemic signal transduction (Zipfel, 2014; Saijo et al., 2018). The resulting signals lead to the activation of a large number of genes also in distant parts of the plant. The systemic acquired resistance is effective against a broad spectrum of pathogens.

The plant hormone salicylic acid is involved in the generation of a global response (Klessig et al., 2018; Tripathi et al., 2019). The activation of the acquired resistance is based on the accumulation of endogenous salicylic acid which triggers the signaling pathway. Also, the plant hormone jasmonic acid plays an important role in the regulation of the plant defense againts herbivores and is activated after wounding of the plant (Gundlach et al., 1992; Koo and Howe, 2009; Zhu et al., 2014).

1.2 Calcium signaling

1.2.1 Calcium - an universal component of nature

Elementary calcium is a shiny, silvery white metal belonging to the group of alkaline earth metals. Calcium only occurs in bound form in the environment, for example in limestone, marble, gypsum or calcite. As part of limestones it is particular abundant in inanimate nature, e.g. it forms entire mountain ranges such as the Limestone Alps.

As an essential component of living organisms, calcium is involved in the structure of bones and teeth in the form of hydroxyapatite and fluorapatite. The exoskeleton of mussels, con-

sisting of two hinged shells, is also almost entirely made of lime. Calcium is also found in the leaves of plants in the form of calcium carbonate, e.g. as a coating for the leaf hairs of the common dogwood (*Cornus sanguinea*).

In chemical compounds, calcium is found almost only in oxidation state +2. Calcium compounds are soluble in water. In contrast, in the cytosol of animal and plant cells, calcium occurs particularly in the form of unbound Ca^{2+} ions. This so-called free calcium plays an important role in signal transmission. Whenever the term "calcium" is used in the following, it always means free Ca^{2+} ions in the cytosol.

1.2.2 Calcium as a fundamental intracellular messenger

Calcium signaling is a complex biological process which plays an important role in various eukaryotic cell types including plant cells (Berridge et al., 2000). Calcium signaling is involved in fertilization and cell death as well as in information processing and storage in the brain (Berridge et al., 1998). Calcium also plays an important role in muscle movement in mammals. Here, calcium is released in an explosive manner from the intracellular calcium stores and initiates muscle contraction. Calcium is also involved in the release of transmitters and neurohormones in neurons. In plants, calcium is primarily known as an intracellular transmitter of the stress response.

A characteristic property of the intracellular calcium concentration is that it is capable of extremely rapid changes. As a result, calcium signals often manifest as a series of short pulses of high concentration in quick succession. This rapid change in concentration is also known as the calcium transient. It should be noted here that a permanently high concentration of calcium would be toxic to the cell since calcium ions can chelate negatively charged molecules in the cell and thus promote cell death. It is therefore vital for the cell that calcium signals are quite short.

Most investigations in plant calcium signaling were carried out using *Arabidopsis thaliana* plants. *Arabidopsis thaliana*, in the following simply called *Arabidopsis*, serves as a convenient model plant in biology because it is comparably handy to seed in the laboratory and can be easily genetically modified. Although *Arabidopsis* is considered as a simple plant it has about 27,000 genes whereas in the mouse only about 22,000 genes are counted (Swarbreck et al., 2008; The UniProt Consortium, 2019). The design of genetically encoded calcium sensors enabled a large variety of insights into the role of calcium signaling in plants (Monshausen et al., 2008; Kanchiswamy et al., 2014; Keinath et al., 2015). In this way, the concentration of calcium can be made visible through miscroscope lenses on a cellular scale and allows detailed spatio-temporal analysis.

1.2.3 Information encoding and decoding by calcium

The repertoire on signal variations of calcium signaling is quite extensive. In response to an extracellular stimulus the concentration of cytosolic calcium can show temporal patterns like bursts or oscillations (Woods et al., 1986). Moreover, calcium signaling reveals spatio-temporal patterns like sparks and puffs, emerging as short repetitive spike-like increases in calcium concentration (Cheng and Lederer, 2008). Calcium signaling is also involved in

long distance signal propagation affecting the regulation of physiological responses. It is assumed that the information, encoded in amplitude, frequency, duration and shape of the signal, allows calcium ions to control different molecular targets in different ways. Over the past years many experimental and theoretical setups were established to decipher this code (Larsen and Kummer, 2003; Smedler and Uhlén, 2014). Although calcium signaling is a well-studied process many details are not fully understood. Numerous in vivo studies on neurons in mammals reveal how difficult it is to correctly interpret the meaning of the calcium signal (Ali and Kwan, 2020). However, there are already studies in plants that establish a specific connection between the form of the calcium signal and the response of the plant (Allen et al., 2001; Kudla et al., 2010; Singh and Pandey, 2020).

Calcium signaling affects many processes on the cellular and subcellular level. It involves a large number of molecular components revealing a complex network structure (Clapham, 2007; Dodd et al., 2010). It is also known that stimulation of cells by external triggers leads to a stimulus-specific response in the cell, which can be explored by measuring the intracellular concentration of free calcium (Webb et al., 1996; McAinsh and Hetherington, 1998). Therefore, it is suspected that the information about the stimulus is encoded in the calcium signal itself and might be recovered by downstream decoding processes (Batistič and Kudla, 2012). Spatio-temporal patterns of calcium are able to encode the stimulus-specific information by varying amplitude, frequency and location of the intracellular concentration of calcium (Hetherington and Brownlee, 2004). This property has led to the spatio-temporal calcium signals also being referred to as "calcium signatures".

The high number of calcium buffers in the cytosol has the consequence that the mobility of free calcium ions might be quite low (Schwaller, 2010). Investigations revealed that the encoding and decoding process of the calcium signal is located in restricted areas of the membrane, called microdomains or nanodomains (Rizzuto and Pozzan, 2006; Demir et al., 2013; Diaz et al., 2016)

1.2.4 Molecular components of calcium signaling in plants

Plants provide a rich set of molecular tools that actively effect the intracellular concentration of calcium: channels, transporters, pumps and buffer proteins. Calcium channels generate the increase, energy-consuming calcium transporters and pumps support the decrease of the concentration of intracellular calcium. Calcium channels can be opened in different ways: some types of ion channels are activated by phosphorylation, others by electrical voltage, and still others by an increase in the calcium concentration itself. By varying the combination of channels and transporters and their operation times the cell is able to create different patterns in response to different stimuli. In the model plant *Arabidopsis thaliana* five families of calcium channels and four families of calcium transporters have been identified at the present time (Ward et al., 2009). Recent experiments confirmed the fine-tuning and waveform-shaping potential of this regulatory system (Costa et al., 2017; Yang et al., 2017).

The second essential pillar of the information transfer is a proper decoding system consisting of a calcium sensor and an effector which performs the encoded operation (Larsen et al., 2004; Kudla et al., 2018). To date, a notable number of calcium sensing proteins in plants have been identified (DeFalco et al., 2009; Hashimoto and Kudla, 2011; Pirayesh et al., 2021). Calmodulin (CaM), CaM-like proteins (CMLs), calcineurin B-like proteins (CBLs) along with CBL-interacting protein kinases (CIPKs), and calcium-dependent protein kinases

(CDPKs) are prominent examples of calcium-dependent proteins that are involved in nutrient sensing and acquisition, stress tolerance and immune response (Harper et al., 2004; Schulz et al., 2013; Ranty et al., 2016; Delormel and Boudsocq, 2019).

Calcium signaling is based on the fact that under unstimulated conditions the calcium concentration in the cytosol is relatively low compared to the concentration in the intercellular space or to the concentration in enclosed compartments such as the vacuole. It increases rapidly to an approximate 10-fold higher concentration when the signaling is triggered and immediately falls back to its original level. This high concentration peak can be repeated several times forming a burst or a continous oscillation. For this, not only calcium stores with a high calcium concentration are necessary but also channels and transporters that bring the calcium into the cytosol and back again on command. The vacuole mainly serves as a calcium store in the plant. The concentration of calcium in the vacuole is estimated to be between 10 mM and 100 mM. Precise measurements are difficult because only a fraction of the calcium is actually available as free ions. Further calcium is present as cofactor in complexes or strongly bound to other compounds (Clarkson, 1984; Leigh, 1997; Paiva, 2019).

Calcium is absorbed from the soil via the apoplastic (extracellular) way and from there it is transported into the cells and stored in specific compartments such as the endoplasmic reticulum or the vacuole (White and Broadley, 2003; Conn et al., 2011). In the cytosol, permanent high concentrations of calcium would be harmful. Therefore, in order to maintain a low concentration in the cytosol, calcium is actively removed by specific pumps also known as Ca^{2+}-ATPases (Kabała and Kłobus, 2005). A variety of Ca^{2+}-ATPases are located in the membrane of different intracellular compartments of the plant cell. Calcium is transferred from the cytosol into the extracellular space/apoplast by P-Type-ATPase IIA (ECA). It is pumped into vacuole by P-type-ATPase IIB (ACA) and CAX protein and into the endoplasmatic reticulum (ER) using Ca^{2+}-ATPases and H^+/Ca^{2+}-antiporters (Geisler, Markus et al., 2000; Kabała and Kłobus, 2005; McAinsh and Pittman, 2009; Dodd et al., 2010).

A prominent player in shaping calcium signatures is TPC1, a membrane protein of the vacuolar membrane. It was first described as a cation channel with slow kinetics which is responsible for the release of calcium from the vacuole into the cytosol, hence originally referred to as SV channel (slow vacuolar). Due to its molecular structure consisting of a two-pore-channel it is now referred to as TPC1 (Hedrich and Neher, 1987; Peiter et al., 2005; Hedrich and Marten, 2011; Hedrich, Rainer et al., 2018). An increased cytosolic concentration of calcium is required to activate TPC1 in plants. The presence of calcium on the cytosolic side lowers the voltage threshold of the TPC1 channel and thus leads to an overall increased opening probability (Hedrich and Neher, 1987). Opening one channel can increase the cytosolic calcium concentration by opening additional channels.

The dissociation constant of cytosolic calcium for TPC1 is above the physiological calcium concentration in the cytosol, i.e. an additional trigger event is necessary for the initial activation of the TPC1 channels (Schulze et al., 2011; Hedrich and Marten, 2011). Besides calcium, inositol trisphosphate (IP_3), abscisic acid (ABA), calmodulin, adenosine triphosphate (ATP) and cyclic adenosine monophosphate (cAMP) are able to trigger the opening of the TPC1 (Pottosin et al., 2009). Hydrogen peroxide (H_2O_2), on the other hand, significantly reduces the probability of opening of TPC1 (Pottosin et al., 2009). The TPC1 channel is also regulated by calcium on the inside of the tonoplast on the lumen side. If the concentration of calcium within the vacuole rises to millimolar levels, the channel is blocked (Beyhl et al., 2009; Dadacz-Narloch et al., 2011; Kintzer and Stroud, 2018).

1.2.5 Calcium Waves

An effective stress-induced system response which puts the whole plant on alert requires a fast long-distance information system. Information can be transported through the plant by passive signals based only on the chemical or physical properties such as diffusion or water pressure or by signals which are actively regenerated by specialized mechanisms consuming energy such as the ATP-binding cassette (ABC) transporters, which are responsible for the translocation of the phytohormone cytokinin to the shoot (Ko et al., 2014).

Plant systemic signals can use different mechanisms covering a wide range of propagation speeds. For example, plants can use physical systems like hydraulic signals for fast long-range communication about water availability (Christmann et al., 2013). Although plants have no central nervous system the occurence of electrical activity is reported in response to salt stress or wounding (Felle and Zimmermann, 2007; Mousavi et al., 2013; Bricchi Irene et al., 2012; Salvador-Recatalà Vicenta et al., 2014). Wounding of leafs in combination with stimulation by inorganic ions causes apoplastic spreading of electrical signals through the plant (Zimmermann et al., 2009). Additionally, Wounding can lead to a local calcium response which is propagated systemically by the vascular system of the plant (Kiep Victoria et al., 2015). Calcium waves are also observed after stimulation with high concentrations of salt (Choi et al., 2014; Xiong et al., 2014). Also the combined action of calcium signaling and wave propagation by electric potentials in the phloem system of the plant is reported (van Bel et al., 2014).

In order to convert a small calcium pulse into a long-distance calcium signal in the sense of a continuous wave, an active amplification of the calcium concentration is necessary. This can be done by means of a series of calcium-dependent calcium channels sitting next to one another, which was first described as calcium-induced calcium release (CICR) in the sarcoplasmic reticulum of muscles of vertebrates (Endo, 1977; Berridge, 1993). CICR is a mechanism based on a positive feedback loop, in which an activated channel opens and releases calcium ions, that diffuse to the neighboring channels and cause them to open (Figure 1A). In this way the wave can propagate along the channels over a long distance. Diffusion through cell-cell-connections such as gap junctions or plasmodesmata allows the wave also to travel from cell to cell through the whole tissue.

In many organisms CICR is a common mechanism for amplifying calcium signals and generating long-distance waves. In plants CICR uses calcium sensitive calcium channels which release calcium from internal stores such as the vacuole or the endoplasmatic reticulum or from external stores located in the intercellular space into the cytosol. The vacuolar channel TPC1 is assumed to support calcium waves by means of CICR (Ward and Schroeder, 1994).

An important detail here is the so-called refractory period of the channel. For proper wave generation by CICR it is necessary that the calcium channels close after release and remain insensitive for a certain period of time. Otherwise retriggering or self-activation of the channel would lead to a constant high concentration of calcium in the cytosol and thus promote cell death.

A key factor in stress response is speed. In animals calcium waves travel with a speed of 10-30 µm/s (Jaffe, 2008). In plants, in which the cytosol is very narrow due to the presence of the vacuole, and where the shoot area is also filled with chloroplasts, one would expect a considerably slower wave. However, in plants calcium waves were observed traveling with a

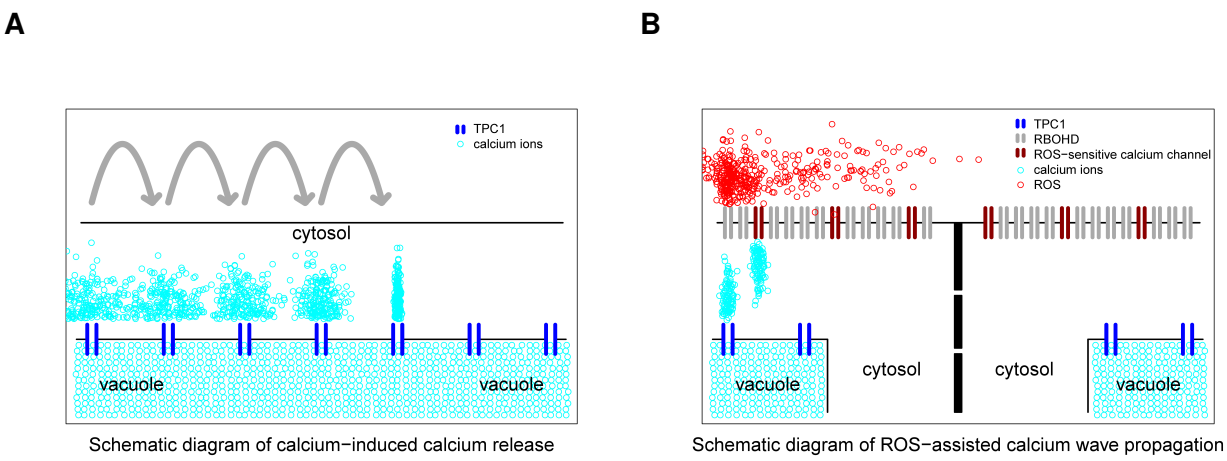

Figure 1. Scheme of calcium-induced calcium release (**A**) and ROS assisted calcium wave propagation (**B**).

speed of 400 µm/s after stimulation with high salt (Choi et al., 2014; Xiong et al., 2014). In *Arabidopsis* seedlings the wave runs through the cortical and endodermal cell layers from the root tip to the shoot (Choi et al., 2014). There is a relationship between the concentration of TPC1 and the speed of the wave. *tpc1-2* knockout mutants show a 25-fold reduction of the wave speed, but not a total elimination of the wave. In contrast, TPC1 overexpression led to an increase in the propagation speed up to around 700 µm/s (Choi et al., 2014). However, a self propagating calcium wave based on calcium diffusion and CICR is too slow. Also, clustering of the vacuolar channel TPC1 or cytoplasmic streaming cannot explain the observed velocities (Evans et al., 2016).

The underlying molecular mechanism supporting this high speed is not known so far. One assumption is, that it is actually an electrical wave which, as a side effect, triggers an increase in the intracellular calcium concentration via a depolarization on the plasma membrane (Hedrich, Rainer et al., 2018). One shortcoming of this hypothesis is, that the plasma membrane is not in direct contact with the tonoplast on which the TPC1 channels are located. In addition, an increase in the electrical potential alone is not enough to trigger the TPC1. Furthermore, the cytosolic calcium concentration must also be increased. Once triggered, the release of calcium into the cytosol could trigger further channels, which could lead to an amplification of the calcium signal, which in turn could support the electrical wave.

Another hypothesis was suggested by Dubiella et al.: they proposed a model which combines the activities of signaling by calcium and signaling by reactive oxygen species (ROS) thus facilitating rapid cell-to-cell communication in response to pathogen attack (Miller et al., 2009; Dubiella et al., 2013). In this model the increase of intracellular calcium triggers the respiratory burst oxidase homolog D (RBOHD) which is located in the plasma mebrane and produces O_2^- radicals via electron transfer across the membrane (Dubiella et al., 2013). RHOBD can be activated by CDPKs (Romeis and Herde, 2014). Active RBOHD in turn is able to continuously generate O_2^-. Evans et al. pursue a similar approach, postulating a coupling of the calcium signal with a ROS signal for the speed increase of the wave (Evans et al., 2016). Figure 1B depicts the molecular processes that characterize a ROS-assisted calcium wave propagation.

1.3 Downstream response to calcium signaling

1.3.1 Plant response to calcium signaling

Signaling by calcium ions plays an extremely important role in plants. This can be concluded from the fact that plant cells have complex mechanisms for maintaining calcium homeostasis and harbor numerous calcium sensor proteins. The calcium-dependent proteins either directly control cellular processes or regulate the activity of other proteins, which in turn affect cellular processes. There are many examples in which calcium signaling acts on transcription factors as a result of plant stress and thus leads to an altered gene expression (Braam, 1992; Luit et al., 1999; Kaplan et al., 2006). In addition, post-transcriptional modifications were observed as a result of the stress-related calcium signaling (Iida et al., 2004; Palusa et al., 2007; Walley and Dehesh, 2010). Examples of direct reactions to stress-induced calcium signaling are the activation of glutamate decarboxylase, the impact on sodium homeostasis by regulating the activity of Na^+/ H^+-antiporter and H^+-ATPase, and the acceleration of stomatal closure (Zik et al., 1998; Yang et al., 2019; Huang et al., 2019).

1.3.2 Stomata closure as an example of a direct effect of plant stress

Plants have small closable openings in the epidermis on the bottom side of the leaves, so-called stomata, which separate the intercellular space of the plant from the outside air. Since the epidermis of the plants is covered by an air-impermeable layer of wax, the cuticle, the gas exchange of the plant mainly takes place via the intracellular space, which is connected to the surrounding air via the stomata. Carbon dioxide is absorbed, oxygen and water are released. The plant can regulate this gas exchange by the closing mechanism of the stomata. The stomata are opened or closed depending on the light intensity, water content and carbon dioxide content of the air. The number of stomata per area also plays a role in controlling the gas exchange. During the development and growth of the plant, the formation of stomata is regulated by the plant hormones auxin, abscisic acid, and brassinosteroids (Qi and Torii, 2018).

Stomata can be found on all plant organs that are exposed to the outside air and are involved in anabolic metabolism. They are therefore primarily located in the lower epidermis of leaves, but also on the stem and on the petals. Roots have no stomata. Stomata are found in shoot plants (Kormophyta) but also in some deciduous mosses (Bryophyta) and fern-like plants (Pteridophyta). As a rule, they are located on the underside of the leaf, but they are only found on both sides of the leaf in grasses and on the upper side of the leaf in floating leaf plants. The stomata also play a role in the transport of water and nutrients. The evaporation through the stomata creates a transpirational pull which sucks the water and nutrients from the roots into the leaves and thus distributes the nutrients within the plant. The resulting evaporation cold also cools the leaves and protects against tissue damage.

Stomata consist of two bean-shaped cells, the guard cells, which enclose an intercellular pore. They are usually surrounded by other specifically designed secondary cells which, together with the guard cells, form the stomatal complex. The closing function of the stomata is effected by the irregular thickening of the cell walls of the two guard cells, which cause the bean-shaped cells to stretch and thus close the pore if the osmotic pressure inside the cell is low enough. The osmotic pressure, also called turgor pressure, usually causes the cytosol

and vacuole to swell, thereby pressing the plasma membrane close to the cell wall. In the case of the stomata, the cell wall of the guard cell acts like a spring that is bent by the turgor thus opening a gap to the intercellular air space. With a low turgor, the spring returns to its straight position and is tightly connected to the cell wall of the guard cell next to it.

However, the stomata also represent a gateway for small pathogens such as bacteria or fungi. In order to avoid the entry of pathogens, the plants developed a mechanism as part of their stress response that closes the stomata when bacteria are recognized. The plant detects the pathogens on the basis of molecular compounds such as oligogalacturonic acid, chitin/chitosan, lipopolysaccharide and flagellin and reacts by closing the stomata (Lee et al., 1999; Klüsener et al., 2002; Melotto et al., 2006). In summary, stomata not only close when humidity is low or when there is an increased concentration of carbon dioxide, but also when a large number of pathogens populate the surface of the leaf.

1.3.3 The role of calcium and CPKs in stomatal closure

The mechanism by which plants close their stomata in response to drought, thus reducing evaporation, has been well studied. In a first step, water stress leads to an increase in the pH value in the intercellular space (Geilfus, 2017). As a consequence, the apoplastic-located plant hormone abscisic acid dissociates into its anionic form. The negatively charged abscisic acid ions are trapped within the alkaline apoplast (Slovik et al., 1995). Because the biosynthesis of abscisic acid is increased during drought, abscisic acid ions accumulate in the vicinity of the guard cells. The negatively charged abscisic acid ion binds to a G-protein-coupled receptor protein on the plasma membrane of guard cells (Pandey and Assmann, 2004). This activates the G-protein and triggers the opening of calcium channels in the membrane (Pandey et al., 2007). Calcium ions flow into the cytosol from the intercellular space. In addition, the G-protein activates phospholipase C and thus leads to the release of IP_3, which in turn promotes the influx of calcium from the vacuole and from the endoplasmic reticulum into the cytosol (MacRobbie, 2000; Dietrich et al., 2001). Both reactions cause a rapid increase in the calcium concentration in the cytosol (Staxén et al., 1999). Final consequence of this increase in calcium is the closure of the stomata (Gilroy et al., 1990; McAinsh et al., 1990; Huang et al., 2019).

Research has shown that calcium-dependent protein kinases are involved in stomatal closure (in general, calcium-dependent protein kinases are abbreviated to CDPKs, while calcium-dependent protein kinases in *Arabidopsis thaliana* are abbreviated to CPKs). In particular, CPK3, CPK6, CPK21, and CPK23 play a role in the signal transduction triggered by the increase of intracellular calcium (Mori et al., 2006; Geiger et al., 2010). These CPK proteins as well as the calcium-independent open stomata 1 protein kinase (OST1) target the S-type anion channel SLAC1, which is expressed in the guard cells of the stomata and is embedded into the plasma membrane. Phosphorylation of the N-terminal domain of SLAC1 by CPK3, CPK6, CPK21, CPK23 or OST1 induces a conformational change of its phenylalanin gate. The channel SLAC1 opens and chloride ions (Cl^-) leave the cytosol towards the intercellular space causing a depolarization of the plasma membrane. The depolarization in turn activates outwardly directed voltage-gated potassium channels in the plasma membrane. The opening of these channels causes an outflow of potassium ions. The efflux of potassium ions is accompanied by an efflux of water from the cytosol followed by a decrease in turgor pressure. The guard cell returns to its original shape and closes the pore.

CPK21 and CPK23 are closely homologous. An analysis with the alignment tool BLAST showed a similarity of around 83 % (Altschul et al., 1990). In my thesis, I focus on the calcium-dependent activation of CPK21 and CPK23.

1.4 Computational models for calcium signaling

Computational modeling is a common tool for investigating different aspects of biological processes and can reveal insight into so far poorly understood areas. The strength of the modeling is not based on exactly reproducing the experimental data in silico, but on testing hypotheses and making predictions about questions that cannot be answered experimentally or only with great effort. The model must be checked for its suitability on the basis of existing data, whereby the type and structure of the model depend on the question to be answered.

Biological models can be roughly divided into deterministic models and stochastic models. Deterministic models are based on mathematical or physical laws and are used for simulation at the population level, i.e. assuming a large number of individuals involved. The same starting values always lead to the same results. Stochastic models are based on a probability distribution and are useful when the number of individuals involved is low and individual events can determine the overall result. Here, identical output values in different simulation runs can lead to different results. Furthermore, models can be divided into spatially homogeneous and spatially distributed models.

When modeling calcium, the focus is mostly on its function as an intracellular signaling molecule. The dynamics of intracellular calcium is based on the difference in concentration between the cytosol and the surrounding compartments. A large number of molecular components is involved in the generation of calcium signaling in different ways, which can lead to a broad range of signal types of the calcium signal. For example, opening individual calcium channels leads to a brief increase in the intracellular calcium concentration, which causes further calcium-dependent calcium channels to open. This process is basically a local stochastic event, which leads to the observed calcium spikes and bursts, but which can extend to global oscillations at the level of the whole cell or even groups of cells (Woods et al., 1986; Toescu, 1995; Dupont et al., 2011). If the release is spatially restricted, waves of increased intracellular calcium can propagate from the release site to other parts of the cell forming a globally travelling wave. Calcium dynamics is structured hierarchically, starting with single interacting stochastic events. Depending on the biological question, it can make sense to use a deterministic or a stochastic model, a spatially homogeneous or a spatially distributed model.

In the literature one can find a variety of models which are devoted to the exploration of calcium signaling, especially with regard to the emergence of calcium oscillations (Sneyd et al., 1995; Schuster et al., 2002; Falcke, 2004; Dupont et al., 2011). In many models, the oscillation is caused by an IP_3 receptor-controlled calcium release from intracellular calcium stores or via the plasma membrane (Cuthbertson and Chay, 1991; Meyer and Stryer, 1988; Sneyd et al., 1995). Some models can simulate chaotic oscillations and even complex chaotic bursting (Shen and Larter, 1995; Borghans et al., 1997; Houart et al., 1999; Kummer et al., 2000). The number of stochastic models is steadily increasing, which is also related to the increasing availability of single-cell data (Young and Keizer, 1992; Nguyen et al., 2005; Kummer et al., 2005; Solovey et al., 2008; Swaminathan et al., 2009; Ullah et al., 2012). An

interesting question is whether calcium transmits information using frequency modulation or amplitude modulation. (Schuster et al., 2002). Some models take into account not only the calcium influx into the cytosol but also the recovery of the base concentration by means of calcium buffers and pumps thereby quantitatively reproducing the experimental data (Bose et al., 2011). A promising approach is the coupling of real experimental calcium data to a computer model of a calcium-dependent enzyme, which allows the estimation of the information content transferred by calcium (Pahle et al., 2008). However, literature on what information is actually transmitted via calcium and how the information content is related to the trigger event is very sparse, probably due to the lack of quantitive experimental data. Also, the knowledge about the molecular details of the propagation of calcium waves is poor.

In computer-aided biology, different modeling techniques can be used depending on the complexity of the system: In addition to model approaches consisting purely of mathematical equations, techniques can also be applied that simulate the behavior of individual entities such as cells or even molecules. I used different methods in my work. For the simulation of the CICR-based calcium wave and the calculation of the propagation speed, I used the diffusion equation according to the computations in the literature (Evans et al., 2016). To investigate the influence of plasmodesmata on the diffusion of calcium and in particular on the propagation speed of the calcium wave I applied the cellular automaton technique. I also used a cellular automaton to simulate the transfer of information from cell to cell and to calculate the information content of the wave. Finally, I modeled the binding of calcium to the CPK proteins using ordinary differential equations (ODEs).

1.4.1 ODE models

Experimental data of biological reactions are often composed of time series that describe how the concentration of an ensemble of chemical particles such as atoms or molecules changes over time. Such data series of a species can be described in a mathematical formula using ODEs. Each chemical reaction is modeled separately by noting the equations for the increase and decrease of the affected species according to its reaction rate. Usually, only the dimension of time is taken into account. It is assumed that diffusion of the particles within the compartment takes place in a much faster time scale than the chemical reaction itself and that the species is therefore always homogeneously distributed in space. In addition, the reactions are only considered at the population level and modeled deterministically assuming a sufficient large number of particles per species.

Given the initial conditions, the concentration of a species can be approximated by numerical integration using ODE solvers such as LSODA (Petzold, 1983). LSODA, as its full name "Livermore Solver for Ordinary Differential equations with Automatic switching for stiff and non-stiff problems" says, is a solution method that automatically switches between methods for stiff and non-stiff differential equations as required and is thus able to solve stiff, i.e. numerically unstable, differential equations very well. For easy handling of large numbers of species and reactions ready-to-use open-source software is available such as COPASI, which by default simulates time series deterministically using the implemented LSODA algorithm (Hoops et al., 2006).

Many biological processes can only be described sufficiently if one considers the change in concentration of a species depending on several variables, e.g. time and space. An equation that comprises derivatives with respect to several variables is called a partial differential

equation (PDE). Using a PDE, non-homogeneously distributed discrete spatial structures such as molecules or cells are approximated by a continuous density distribution.

1.4.2 Cellular automata

If the underlying biological process is complex and contains many unknown variables and parameters, cellular automata are well-suited as a first step of mathematical modeling. Building up a cellular automaton model from scratch enables us to reduce the observed phenomenon to its core properties and to check the sufficiency of the implemented rules for the occurence of the observed pattern. If the cellular automaton model resembles the experimental data it can be used as a starting point for a more detailed mathematical model based on ODEs or PDEs. Furthermore, missing parameters can be explored or verified by targeted experimental setups. Cellular automaton modeling is a computational modeling approach that provides a simple intuitive graphical representation of the modeled system. It allows an immediate comparison with experimental data by manual inspection. This is quite helpful especially if the experimental data exhibit pattern formation in space or time. A hypothesis or putative mechanism can be formalized in a comprehensible way without the need of solving differential equations. The direct visual feedback also allows a rough estimation of hidden parameters just by "guess and try". Cellular automata are easy to implement with elementary programming skills. In general, the simulation is quite fast and can be performed by state-of-the-art computers.

A cellular automaton is a computational modeling system based on a grid of discrete cells which interact with their neighboring cells according to simple rules but are able to reveal complex behavior. Cellular automata are characterized by a fully discrete structure of all components including space, time and state. The idea of cellular automaton modeling was originally developed by the mathematicians Stanislaw Ulam and John von Neumann (Von Neumann and Burks, 1966). Cellular automata are able to mimick the rules of nature for example self-reproduction and self-similarity (Langton, 1984; Takahashi, 1992; Hutton, 2010).

Cellular automata are composed of four components: an n-dimensional grid of cells, a finite number of elementary states for each cell, a local neighborhood and a local function which calculates the state of each cell according to its neighborhood. Most cellular automata are based on a two-dimensional or multi-dimensional grid, but one-dimensional cellular automata are also possible. Cellular automata usually employ deterministic rules. Only the initial state of the cells might be chosen randomly. However, it is also possible to implement stochastic probabilities for the local function (Agapie et al., 2014).

Cellular automata can be used for modeling a variety of processes, for example the growth of snow crystals, the spreading of diseases or forest fires or the occurence of traffic jams on a motorway (Nagel and Schreckenberg, 1992; Reiter, 2005; Pfeifer et al., 2008). A very famous example of a two-dimensional cellular automaton is Conway's "Game of Life" which is a simple simulation of an artifical population (Gardner, 1970). Similarly, Stanisław Marcin Ulam described the generation of complex morphological patterns from simple rules (Ulam, 1962). An example of a simple one-dimensional cellular automaton is the Nagel-Schreckenberg model, which is used to calculate traffic flows and is intended to prevent traffic jams (Nagel and Schreckenberg, 1992). There are also applications which are closer to nature. Cellular automata employing threshold-based rules were used to mimic the electrophysiological re-

sponses of neurons (McCulloch and Pitts, 1943; Hopfield, 1982). There were studies which used cellular automata to simulate complex behavior like recognition and learning (Minsky and Papert, 1969; Cun, 1986). Many complex patterns found in nature like snowflakes or mollusc shells can be simulated by using cellular automata (Wolfram, 1984). Furthermore, one publication claims that plants use a calculation system of the gas exchange by stomata which is similar to a computer-based calculation based on a cellular automaton (Gardner, 1970). Fibroblasts - specialized cells of the connective tissue in animals - can also be considered as cells of a cellular automaton because they only interact with their direct neighbors (Bouligand, 1986). Following an idea of Gerard 't Hooft, even quantum mechanics might be deterministically simulated by cellular automata (Hooft, 2016).

II Materials and methods

2 Materials and methods

2.1 Stimulation experiments

2.1.1 Plant stimulation using microfluidic technology

Experiments were performed by my collaboration partners Rik Brugman, Guido Grossmann and Janos Löffler in the lab of Guido Grossmann at Heidelberg University. *Arabidopsis thaliana* seeds were surface sterilized and germinated on cut pipette tips, prefilled with solidified Hoagland's medium (Sigma-Aldrich, www.sigmaaldrich.com). Under controlled temperature and light conditions (90 to 120 $\mu E\,m^{-2}\,min^{-1}$; 16-h-day/8-h-night cycle) the roots grew gravitropically into the conical medium-filled plastic cylinders. After five days the pipette tips were plugged into a microfluidic device (RootChip®) together with the seedlings. Roots grew from the solid medium in the pipette tips into the horizontal observation chamber of the RootChip, which was prefilled with liquid Hoagland's medium. The pipette tips were slightly tilted, so that there was only an angle of 60 degrees with respect to the horizontal observation chamber, to make it easier for the roots to grow from the vertical tip into the chamber. As soon as the roots reached the entry of the chamber, they were perfused with half strength liquid Hoagland's medium at low flow pressure (1 to 2 p.s.i.).

Image acquisition and root stimulation were performed seven days after germination. Imaging of the roots was started 3 to 5 minutes in advance before treatment. Treatments were done with 5-min square pulses of different types of stimuli: bacterial peptide flg22 (1 µM), sodium chloride (NaCl, 100 mM), fungal cell wall components chitin and C8 (1 µM). The elicitors were dissolved in half strength liquid Hoagland's medium. A detailed description of the chemicals and the microfluidic device can be found in Grossmann et al. (2011) and Keinath et al. (2015).

The microscope was a spinning disk epifluorescence microscope Nikon Eclipse Ti2 with a Fluor 10x differential interference contrast (DIC) objective. Images were captured with a digital CMOS camera Hamamatsu C11440-22C using the software NIS-Elements AR version 4.2 from Nikon. Images of the root were taken over a period of about 20 minutes starting 3 to 5 minutes before the treatment. The resolution of the raw data images was 512×512 pixels, 16-bit single channel, pixel size 1.6 µm×1.6 µm (datasets from the publication of Keinath et al. (2015): 550×98 pixels, 24-bit RGB, pixel size 2.63 µm×2.63 µm). The frame rate of the image acquisition was 2 Hz for treatment with sodium chloride, 1 Hz for C8, 0.67 Hz for flg22 0.67 Hz for for chitin.

2.1.2 CPK in vitro assays

The experimental data were taken from Figure 4B of Geiger et al. (2010) with the kind permission of Dietmar Geiger from Würzburg. I got the values by measuring the data points in the PDF file of the publication. As described in the publication, in vitro kinase assays were performed using recombinant proteins. CPK21 and CPK23 were subcloned into a recombinant expression vector and transformed into *Escherichia coli*. The calcium-dependent

phosphorylation activity of CPK21 and CPK23 was determined by counting radioactivity of excised gel slices harboring the GST-tagged N-terminus of the anion channel SLAC1 (SLAC1 NT). A detailed description of the experimental procedure can be found in the methods section of the publication of Geiger et al. (2010).

2.1.3 Guard cell and epidermal cell stimulation

Experimental data were kindly provided by Melanie Krebs from Heidelberg. Calcium-dependent signal changes in response to flg22 and chitin in leaves of 14- to 16-day-old seedlings were measured by analyzing fluorescence images of R-GECO1 at the top of the leaf. Treatment was 100 nM flg22 or 100 µg/ml chitin applied 30 minutes after starting data acquisition. Concentration values were calculated from normalized R-GECO1 fluorescence intensities ($\Delta F/F$) according to the formula described in Wang et al. (2015), Figure S2 (B). A detailed description of the experimental procedure can be found in the methods section of the publication of Keinath et al. (2015).

2.2 Image analysis and modeling

2.2.1 Computational setup

I developed the algorithms using the open-source programming language R (version 4.0.2) on macOS Catalina (version 10.15.7) on a MacBook Pro with an Intel 2,5 GHz Quad-Core i7 processor (R Core Team, 2020). For the import of images I used the package png in version 0.1.7 and tiff in version 0.1.5 (Urbanek, 2013a, b). The source code of my algorithms is freely available for download in my heiBOX library at https://heibox.uni-heidelberg.de/library/59834a18-c5f8-4a20-9e27-e4b6130e9398/calcium%20modeling/.

For modeling the activity of the CPK proteins I used the software COPASI (COmplex PAthway SImulator; version 4.29 build 228) and the corresponding R package CoRC (version 0.8.0) which provides a convenient developer's API for the biochemical modeling tools of COPASI (Hoops et al., 2006; Förster et al., 2021). The software tool COPASI/CoRC was also used to fit the experimental data. I ran parameter estimations on a compute cluster with Linux (CentOS 6.4 x86 64-bit Kernel 2.6.32) using Sun Fire AMD Opteron and IBM Quad Intel Xeon CPUs.

For performing simulations with a cellular automaton I created a software framework consisting of a set of self-written R functions which allow an efficient and convenient modeling of various scenarios (see file cellular_automaton.R in my heiBOX library). This framework comprises a function for the simulation itself, a function for plotting the final state of the simulation and a couple of examples how to wrap the automaton rules into a local function including "game of life" and 2D diffusion. The local function is comitted to the simulation function as an argument, therefore it is easily possible to run the simulation with custom-designed local functions. The idea was to keep the code as simple and handy as possible at an acceptable performance. Therefore, I used only the base package of R for coding, even for the graphical representation of the results.

2.2.2 Data sources

For my work, 69 image datasets were available as raw data kindly provided by the experimentalists of the Grossmann Lab, which could be used directly as input for my algorithm (21 × flg22, 9 × chitin, 28 × C8, 11 × NaCl). In addition, I applied my algorithms to two datasets provided in the supplemental section of Keinath et al. (Keinath et al., 2015). These two datasets were downloaded as video files from the website of the Journal *Molecular Plant* at *ScienceDirect* (https://ars.els-cdn.com/content/image/1-s2.0-S1674205215002397-mmc7.mp4; https://ars.els-cdn.com/content/image/1-s2.0-S1674205215002397-mmc8.mp4). I used the open source software ffmpeg (https://www.ffmpeg.org/) in version 3.3.1 for macOS Sierra 64-bit Intel (http://www.ffmpegmac.net/) to convert the video files back into a series of single images. I used default parameters for conversion resulting in png image files with lossless compression (commands: ./ffmpeg -i 1-s2.0-S1674205215002397-mmc7.mp4 %04d.png and ./ffmpeg -i 1-s2.0-S1674205215002397-mmc8.mp4 %04d.png). The flg22 dataset consists of 998 images with a size of 550×98 pixels, the chitin dataset of 911 images with a size of 550×98 pixels. For a detailed description of the image acquisition see also "Experimental Procedures" section of Keinath et al. (2015). I developed my own conversion algorithm for converting the two image series back from the color representation to a monochrome representation corresponding to a raw data input (see file image_preprocessing.R in my heiBOX library).

2.2.3 Colormap

For an excellent illustration and an intuitive understanding of the analysis all results in matrix form were printed as colored images. Images, kymographs, surface plots and crestline plots were depicted using a colormap which is composed by a linear interpolation of the following nine RGB colors: #352A86, #0362E0, #1483D4, #05A5C7, #33B8A0, #8CBE74, #D2BA58, #FDCA30, #F8FA0D (Figure 2). This colormap is a simplified version of the colormap *parula* which is known to be very convenient (MathWorks, 2014). In particular, it is perceptually uniform, can be converted into grayscale without loss of information and is also clearly recognizable for colourblind people. I chose this colormap because it highlights the different intensity values much better than a pure grayscale colormap.

Figure 2. Colormap used for the output of the wave analysis. This is an example colorbar for the interval [0, 1] showing the colormap which is used for all the graphical outputs of the wave analysis. The image data are scaled for the output in such a way that the lowest intensity value corresponds to 0 and the highest value to 1, low values therefore appear in dark blue, high values in yellow.

III Results

3 Image analysis of calcium waves in plant roots

3.1 Chapter introduction

This chapter describes a computational approach for calcium wave visualization and quantification which is capable of processing time-lapse image stacks of fluorescence microscopy images of plant roots and analyzing the intensity changes caused by increased concentrations of intracellular calcium. I developed an algorithm for automated image analysis and applied it to different high-resolution microscopy images of genetically modified *Arabidopsis thaliana* plants stably expressing a calcium sensor (Figure 3).

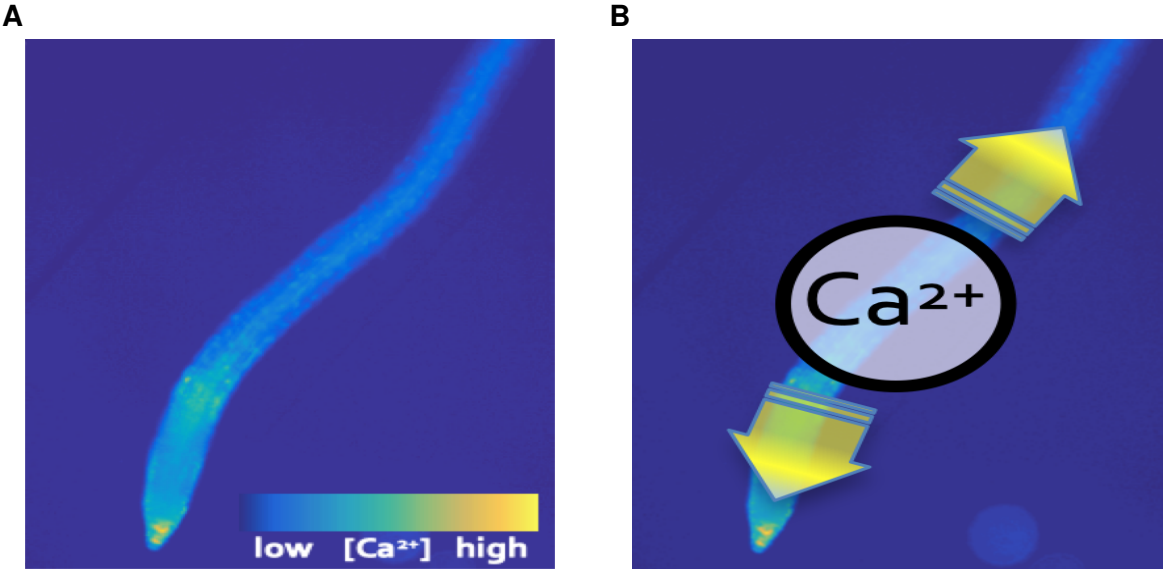

Figure 3. Fluorescence microscopy image of a root tip of an *Arabidopsis thaliana* seedling before stimulation (**A**). After the seedling has been stimulated with an elicitor such as flg22 or chitin, a calcium wave runs through the root, as indicated in the sketch (**B**). The plant used here stably expresses the calcium sensor R-GECO1 in the cytosol. High concentrations of intracellular calcium are visible in the outermost root tip and in a zone around 0.5 mm behind the tip. The image size is 1.4 mm x 1.4 mm. High concentrations of intracellular calcium show up in yellow, medium concentrations in green and low concentrations in dark blue (for a detailed description of the colormap see Section 2.2.3). The sketch in panel **B** shows in which directions the calcium wave propagates after stimulation.

The algorithm comprises three key contributions:

- Automated generation of a time-space diagram (kymograph) by detecting the outline of the root and calculating the mean intensity at each position perpendicular to the axis of the root (Figure 4A; detailed description in Section 3.3).
- Position-related scaling of the kymograph resulting in a distinct representation of the calcium wave called the "crestline plot" (Figure 4B; Section 3.4).
- Algorithm for analyzing the crestline plot by identifying key parameters of the calcium wave such as the starting position and starting time of the wave and the propagation speed into both directions (Section 3.5).

The kymograph as well as the crestline plot can be easily visualized as a 3D-like surface plot (Figure 5). The analysis is augmented by a quality check of the image data including a detection of artifacts or defective datasets.

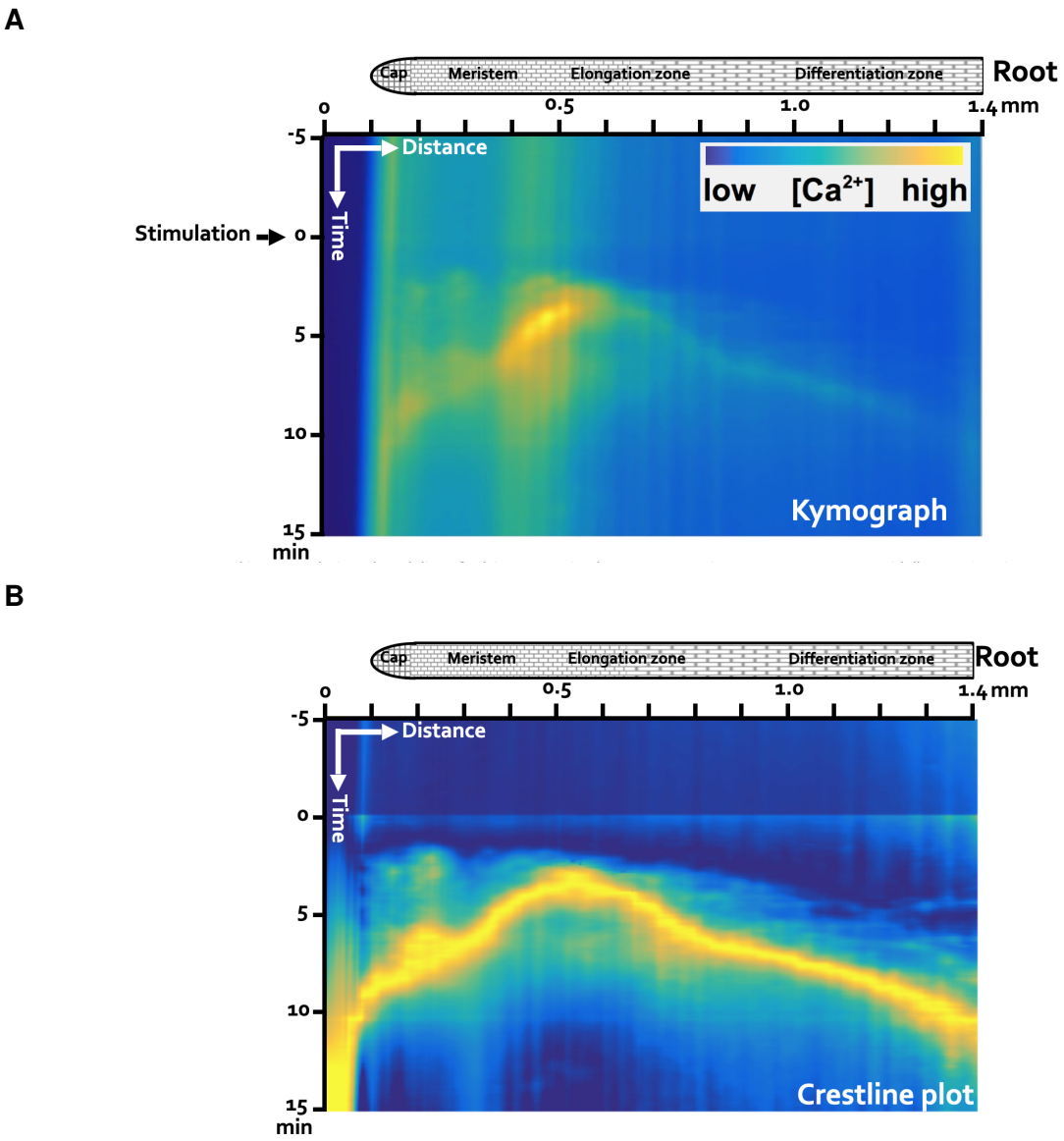

Figure 4. Representative display options of the automated image analysis using an example image series of a stimulation experiment with flg22: kymograph (**A**), crestline plot (**B**).

3.1.1 Calcium signature detection

The main part of my thesis is dedicated to the analysis of calcium waves in *Arabidopsis* seedlings in response to stimulation by environmental stress. These calcium waves have already been described in several publications (Choi et al., 2014; Keinath et al., 2015). One difficulty is to make these waves properly visible in order to measure and analyze them. My collaborators from the Grossmann Lab used their microscopy and camera setup with a RootChip for monitoring R-GECO1-expressing *Arabidopsis* seedlings (for a detailed description of the method see Section 2.1.1). This setup makes it possible to create time-lapse recordings that depict the different intracellular calcium concentrations which form the basis for the calcium waves.

My aim was to create a mathematical model of the calcium waves and to use this model for answering biological questions. To do this, I first had to "extract" these waves from the images, which can be done by plotting the calcium concentration as a function of space and time. A common way of displaying such functions is the kymograph. From the kymograph one can infer parameters such as the starting point, duration and intensity of the calcium wave. Both steps - the generation of the kymograph from the microscopy images as well as the extraction of the parameters from the kymograph - effectively mean a reduction of the data with the aim of limiting it to the desired information content. By leaving out irrelevant information, the characteristics of the wave should become more visible and clear.

The data reduction process can be done in different ways. So far, the creation of the kymograph was performed partially automatically using a Fiji/ImageJ script. The resulting curve was analyzed manually using ruler and pencil. I automated these steps deploying an R script in order to make the interpretation more objective and, in particular, to test various evaluation options quickly and easily. The evaluation from different points of view can lead to a better overall understanding of the calcium wave.

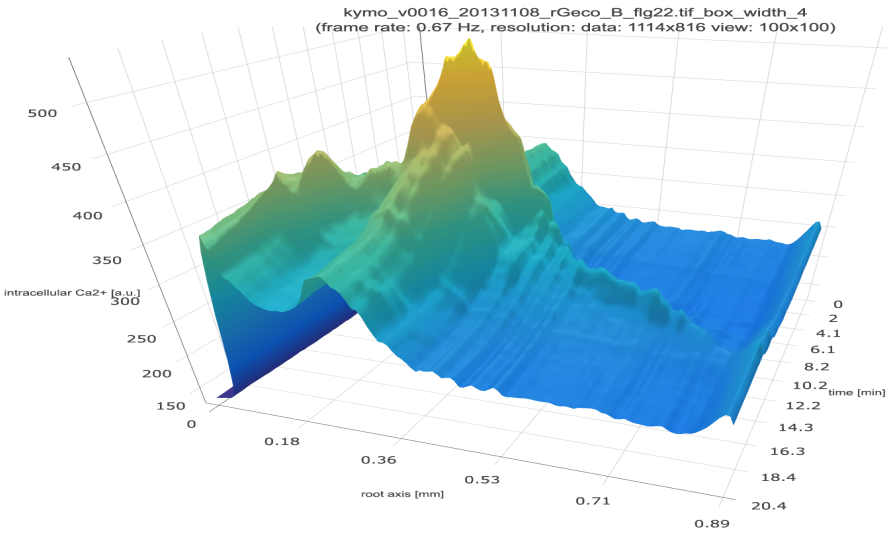

Figure 5. The surface plot is a 3D-like representation of the kymograph and gives the viewer an impressive idea of the course of the calcium wave.

3.1.2 Plant stimulation

The investigation of calcium waves started with the stimulation of *Arabidopsis* seedlings in the wet lab. NaCl was chosen to provoke an abiotic stress response in the plant. flg22, chitin and C8 were chosen as biotic stimuli.

The flagellin peptide flg22 is a so-called pathogen-associated molecular pattern (PAMP), which consists of a 22 amino acid long peptide chain of flagellin and is known to trigger the innate immune response in plants (García and Hirt, 2014). The globular protein flagellin is an essential component of the bacterial flagellum. In *Arabidopsis*, flagellin binds to the receptor protein kinase FLS2 (LRR receptor-like serine/threonine-protein kinase FLS2), which in turn induces the binding of BAK1 to FLS2 and thereby triggers the innate immune response (Chinchilla et al., 2007).

Chitin is a component of the fungal cell wall and elicits the plant's stress response to fungi. Chitin is a polymer consisting of N-acetylglucosamine monomers. Its chemical formula is $(C_8H_{13}O_5N)_n$. The number of monomers in natural chitin can vary. In addition, the degree of acetylation of the monomers can vary. This means that natural chitin is usually not a uniform polymer, but a statistical mixture of D-glucosamine and N-acetylglucosamine, so not every amino group is acetylated. C8 in turn is a particular form of chitin, that consists of exactly 8 N-acetylglucosamine units (chemical formula $(C_8H_{13}O_5N)_8$).

To make the changes in the concentration of intracellular calcium visible at all, genetically modified *Arabidopsis* seedlings were used, which stably express the calcium sensor R-GECO1 in the cytosol. This enables calcium to be visible using fluorescence microscopy. For the experiment, *Arabidopsis* seedlings were put into a microfluidic device (RootChip) and stimulated with the aforementioned stimuli. Over a period of about 20 minutes, a series of time-lapse images was captured with the microscope camera, which comprises between 800 and 1200 single images depending on the type of experiment.

3.1.3 Algorithms for automated image analysis

If we talk about automated computer-aided image analysis, we usually think of the identification and inspection of objects in a live image. A prominent example is the automated recognition and verification of license plates. Automated image analysis is used in the manufacturing industry to identify products and test them for certain properties, e.g. the size of components or the fill level of bottles. In principle, detection of calcium signatures in microscopy image stacks is a similar task: the roots of the *Arabidopsis* plant should be recognized and measured and the calcium concentration of their cells should be determined.

The detection and recognition of objects is a demanding visual task which is investigated by a large and rapidly evolving community. Precise detection of objects can be challenging and there are lots of algorithms available depending on the aim of the task. At present, the prevalent approach is object recognition by local appearance. The object in question is assigned to an object class which is defined by a collection of small visual particles. Part-based models are a common object recognition technique based on local appearance (Figure 6). In the part-based model approach the particles are embedded into a configuration model which includes the relative position of the particles to link them to each other representing well-defined parts of the overall object (Burl et al., 1998; Sali and Ullman, 1999). Another

technique based on a collection of particles is the bag-of-features model (Figure 7). With this approach, the particles are used without any information about their position in the object (Lowe, 1999; Sivic and Zisserman, 2003). Shape detection is an important element of these algorithms (Belongie et al., 2002).

State-of-the-art detection algorithms use convolutional neuronal network or machine-learning techniques for object detection which require training and test datasets containing images with sample objects (Dollar et al., 2009; Felzenszwalb et al., 2010; Girshick et al., 2014; Redmon et al., 2016; Xiao et al., 2020). However, for detecting a plant root in an image local appearance technique is unhelpful because the contrast of the image is very low and the local structure of the root tip is very similar to the local structure of the background. But, the global shape of the root is very prominent and can be easily recognised by its outline. Furthermore, the root is the only object in the image and the object recognition task can essentially be boiled down to the detection of a single closed outline in the image.

The essential step towards global shape detection is to extract the outermost edges of the object. Many algorithms are available for edge detection: Prewitt filter, Sobel filter, Canny edge detector and combinations or extensions of them (Sobel and Feldman, 1968; Martin et al., 2004; Gonzalez and Woods, 2017). However, in case of poor contrast most methods fail to precisely detect the outermost outline of an object. Depending on the chosen threshold for the filtered image they either detect many edges within the object or detect only fragments of the overall outline. For my purpose a simple but robust detection of the shape of the object would be sufficient, especially because the images are one-channel images (grayscale). Therefore, I simply applied global thresholding directly to the image after smoothing the image with a minimum or median filter and then calculated the outline of the remaining object (Gonzalez and Woods, 2017; Umbaugh, 2017).

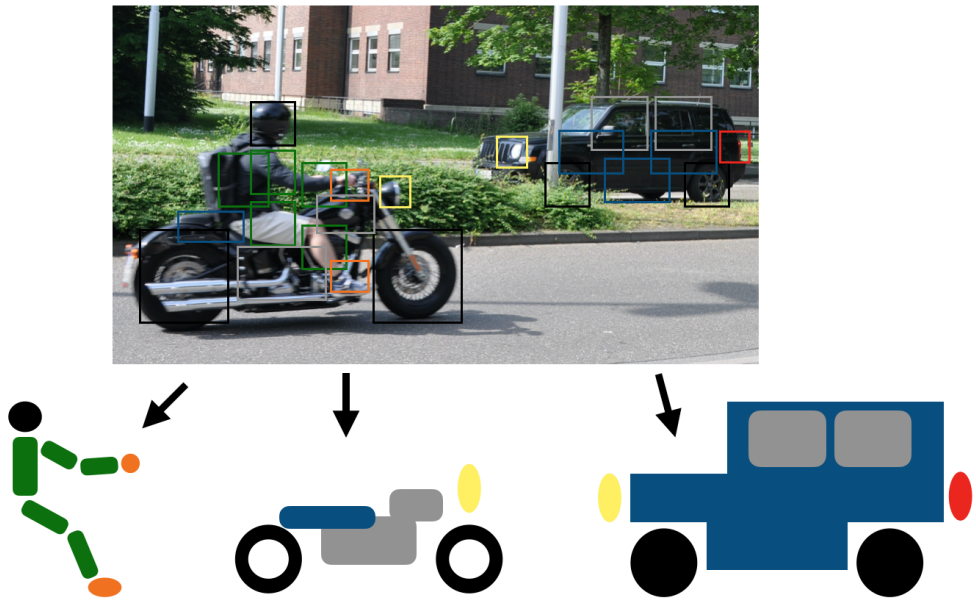

Figure 6. Part-based models combine methods that use different parts of the image to determine whether and where an object of interest is present. One of these is the constellation model, in which a small number of features and their relative positions are used to detect the object.

Figure 7. With the bag-of-features method, an object is described by an orderless collection of quantized local features. The object is recognized based on the appearance of these characteristic features in the image to be classified. Although the method is relatively simple and does not require any spatial information about the features, the detection performance is quite high.

3.2 Analysis workflow

The investigation of the calcium signatures is based on two pillars: the stimulation experiment in the wet lab, in which the image data are created, and the analysis of the images on the computer. In order to standardize the results and make them reproducible, they were carried out according to a standardized workflow (Figure 8).

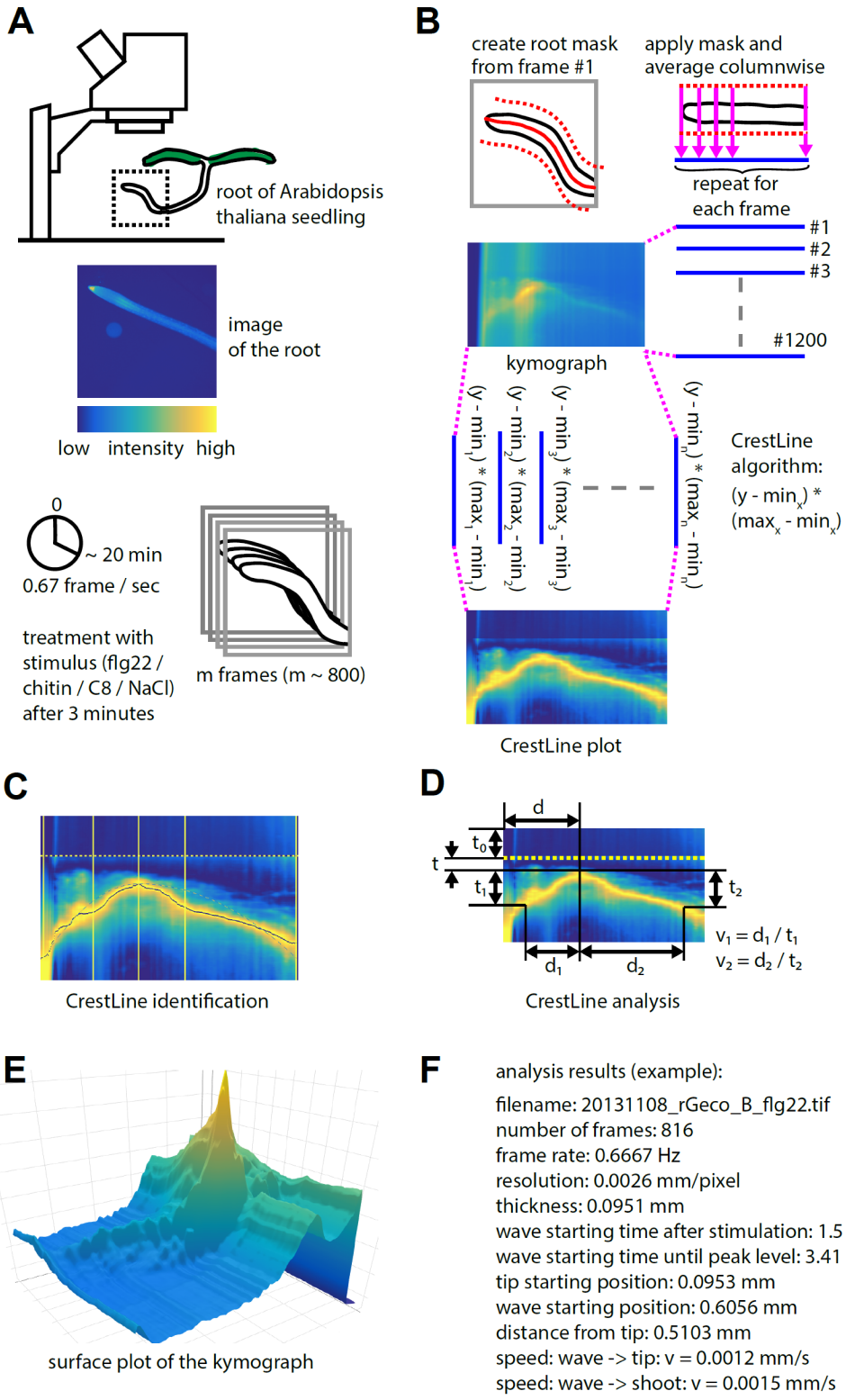

Figure 8. Workflow of the automated image analysis: (**A**) Experimental setup: about 800 to 1200 single channel images will be created during the experiment with a frame rate between 0.1 and 2 frames per second. (**B**) The image stack is converted into a kymograph by averaging the image intensity along the axis of the root. Subsequently the crestline algorithm is applied to the kymograph. (**C**) The track of the crestline is identified. (**D**) The crestline is analyzed with respect to starting time t and starting position d of the wave. t_0 denotes the time delay before the stimulus is applied. The speed of the wave towards the tip (v_1) and towards the shoot (v_2) is calculated. (**E**, **F**) Screenshot of the output of the R script: interactive surface plot of the kymograph (**E**) and console output with analysis results (**F**).

3.3 Kymograph generation

The first prominent part within the context of image processing is the preparation of a kymograph from the raw data image stack which reduces the dimensionality of the data by one and converts the time-lapse-movie of the stimulation experiment into a two-dimensional space-time-diagram. The generation of a kymograph requires a reliable detection and calculation of the axis of the root. My approach applies an object detection algorithm to the image to detect the shape of the root and calculate the outline. The outline is then used to calculate the longitudinal axis of the root.

From a mathematical point of view, the kymograph consists of a two-dimensional matrix of intensity values. Each image of the image stack is represented in the matrix by a one-dimensional vector containing the averaged image intensities along the axis of the plant root. Interpreting the matrix values as pixels results in the typical kymograph image (Figure 4A). A three-dimensional representation with a 3D effect can be achieved by interpreting the intensity values as height values and generating a surface plot from them (Figure 5).

The kymograph generation process is subdivided into several successive steps. Table 1 gives an overview of the successive operations and the algorithms used. In Figure 9 the most important steps are shown schematically using original data.

Table 1: Workflow and algorithms used for generating a kymograph from raw data images. The algorithms are applied one after the other, starting from the raw image. The output of one algorithm serves as input for the next algorithm.

purpose of the operation	algorithm
image rotation: root tip on the left	root tip detection, if necessary: rotation
background noise reduction	smoothing filter (5×5 minimum filter)
intensity outlier detection and removal/restriction	global threshold: the maximum intensity is limited by the threshold
binarization of the image	global threshold
outline detection	perimeter calculation using the binary image
object detection	connected component labeling
artifact removal	classify objects by size and remove small ones
centerline calculation	sliding window: k-medoids with $k = 2$, midpoints between the two centroids
angle calculation of the centerline	sliding window: angle between outermost points of the centerline segment
The centerline is only determined using the first image. To create the kymograph, the centerline is used to calculate the mean intensity for each image of the image stack.	
image quality check: replace bad images	compare background intensity of two consecutive images
kymograph calculation: applied to all images of the image stack	sliding window: averaged intensity of a sliding box along the centerline

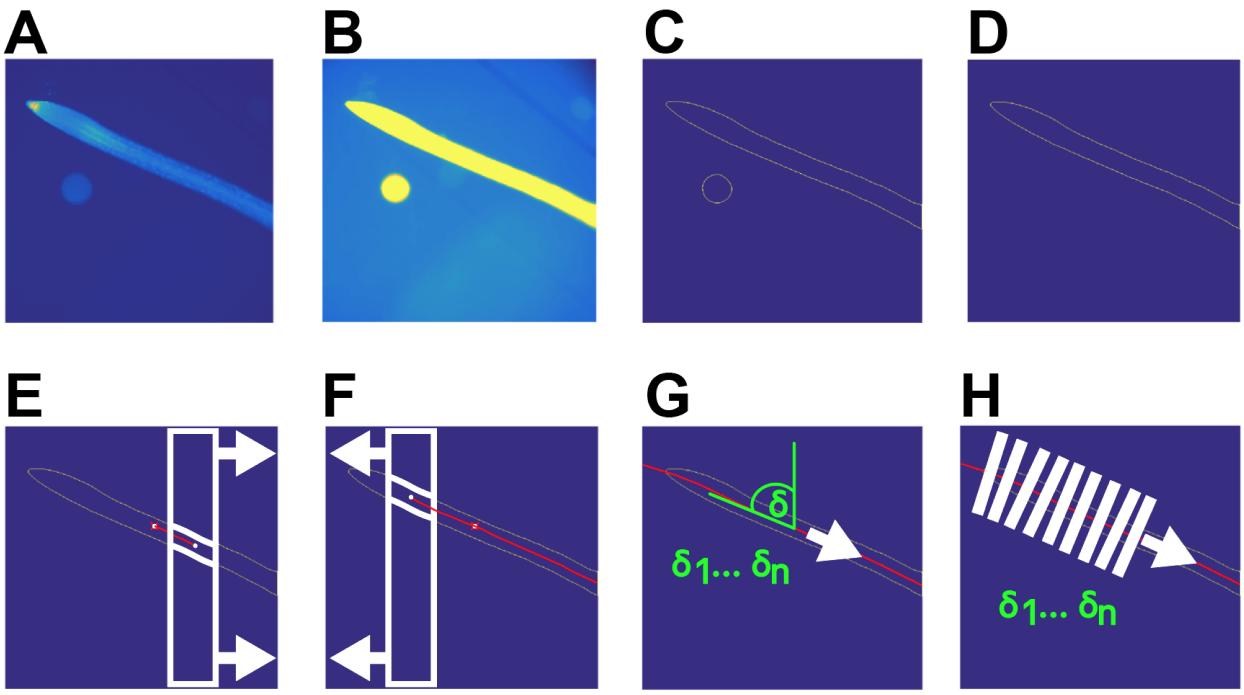

Figure 9. The kymograph is generated in several consecutive steps by calculating the averaged image intensity along the axis of the root. (**A**) Raw image (image size: 1.4 mm×1.4 mm). (**B**) Image after application of a 5×5 pixel minimum filter and an intensity outlier removal algorithm. This image serves as the basis for the binarization by means of an intensity threshold. The image may contain clearly visible artifacts, such as a drop of water (round spot). (**C**) Outline of the binarized image. (**D**) Artifact removal of connected components smaller than 50 % of the largest component. (**E**, **F**) Centerline calculation using a sliding window and a k-medoids calculation with $k = 2$ starting from the center of the image. (**G**) Angle calculation along the centerline. (**H**) Kymograph calculation by averaging the intensity along the centerline using a sliding box with a width of 13 µm. The width of the box determines the smoothing factor.

The prerequisite for the creation of a kymograph is the detection of the outline of the root. Assuming that the root is in a fixed position during the time of the experiment I use the first image of the image stack as a reference. Although the root is slightly growing during the time span of the experiment it is meaningful to use an identical reference for all images to facilitate the combining of the processed data of all individual images to a kymograph matrix. The first image is well suited as a reference because it can be assumed that the camera settings were checked manually before starting the experiment. The image quality of the first image should therefore be optimal.

3.3.1 Image rotation based on tip detection

In preparation for the generation of the kymograph, I apply a tip detection algorithm to the image to find the orientation of the root. The tip of the root is characterized by its high intensity, even in the unstimulated state. I look for the area of the image with the highest intensities and, if necessary, arrange for a rotation of the entire image stack. For better comparability of the kymographs of different experiments with each other, the convention was made that the root tip should always be on the left and the shoot always on the right. In the raw image, however, the root can be in any orientation on the image plane. In order

to avoid mix-ups in the subsequent evaluation steps, especially when calculating the speed of the wave along the root, the image is aligned at this point with the root tip. Image rotations in 90-degree steps can be achieved easily for pixel graphics without loss of accuracy and are fully sufficient for the required purpose. Therefore, depending on the result of the tip detection the raw images are rotated by 90, 180 or 270 degrees to ensure the tip being in the left half of the image, as close as possible to the left border of the image.

3.3.2 Background noise reduction by minimum filtering

The raw images captured by the CMOS or CCD camera of the microscope often reveal a lot of noise caused by the equipment itself (light source, amplifier, sensor). For appropriate image analysis it is necessary to remove or at least reduce this noise. The background noise strongly depends on the technical installation and its quality and therefore its reduction has to be adjusted according to the equipment used.

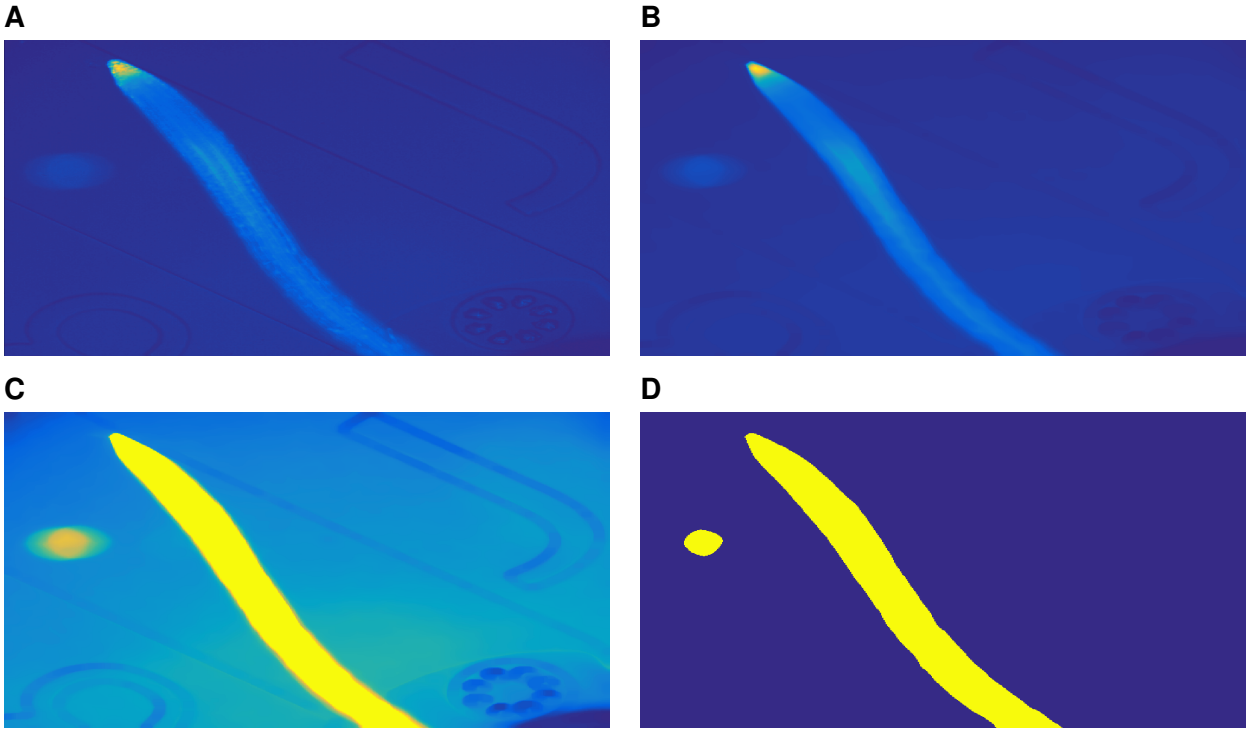

Figure 10. In order to improve the object detection of the root and to increase the contrast of the image, the background noise has to be filtered out and high intensity values must be reduced. An example raw data image is shown in panel **A**. After applying a 5×5 minimum filter, the image is smoothed and the contours of the root emerge more clearly (**B**). Very high intensities, as can often occur in the root tip or due to defective sensor pixels in the camera, hamper the outline detection of the root. Therefore, the maximum intensity is limited to twice the intensity of the background pixels (**C**). Due to the clearly recognizable borders between background and foreground, the image can be binarized by using a fixed global threshold (**D**).

Based on the data, I chose applying a 5×5 pixel minimum filter to the raw data (Figure 10). This means that each pixel is replaced by the darkest pixel (smallest intensity value) of all 25 pixels surrounding it, including the pixel itself. The minimum filter improves the identifiability of the background but does not affect the foreground substantially. Minimum

filtering is based on the assumption that the expected intensity value of the background is very low. Statistical variations of the intensity caused by the camera sensor lead to a positive peak of a few pixel values. This error is corrected by the minimum filter which decreases the noise in the background area and therefore improves the detection of the foreground. In my project a 5×5 pixel minimum filter yielded best noise reduction without loosing too much information of the image structure. Future cameras and microscopes might produce less background noise.

Additionally, an outlier detection and removal algorithm is applied to the image to disregard pixels which are incorrect due to defective sensor pixels or other technical flaws. For this purpose I approximate the intensity value of the background of the image and cut off all values which exceed double of the background. This step is necessary because defective sensor pixels lead to extremely high intensity values which impair the image quality in a substantial manner. This algorithm also solves another issue: there is often a very high calcium concentration in the cells close to the root tip and therefore very high absolute intensities. The intensity of the other cells is quite weak and only slightly larger than the background intensity. By limiting the maximum intensity, the high intensity values of the root tip are diminished and the overall contrast of the image is improved.

3.3.3 Outline detection

The overall fluorescence intensity of an image of the root is quite small because the calcium sensor R-GECO1 is expressed only in the cytosol and the cytosol in plant cells has a relatively small volume compared to the vacuole. Therefore, the object detection of a root can be challenging. A key step of my detection algorithm is the generation of a binarized image of the root that will later be used to calculate the outline of the root (Figure 10D).

A binarized image, i.e. a black and white image, is based on an intensity matrix that only contains the values 0 or 1. In order to transform the raw image from a grayscale image into a black and white image, I use a global threshold for the intensity values. A suitable choice of the threshold should separate background pixels from object pixels, i.e. pixels that belong to the root should have the value 1 and pixels that belong to the background should have the value 0. From a mathematical point of view, all intensity values of the raw image that are above or equal to the threshold are set to 1 and all values that are below are set to 0.

During the development of my analysis script, I programmed and tested three alternative methods for determining the global threshold:

- threshold calculation based on an intensity histogram of all pixels (default method)
- threshold as a fixed offset of the background intensity
- threshold calculation based on the usual foreground to background ratio

In the main method, which has proven to be the most stable and which I also use by default for my work, the threshold value is calculated using an intensity histogram of the image. This method is based on the assumption that the histogram has a tub-shaped form: many low intensity values (background), many high intensity values (root) and a wide transition area with relatively few values per bin. So I am assuming that the original image already has kind of a binarized structure and that the medium intensity values are mainly located at the transition points from the background to the object, i.e. at the edges of the object.

Using a histogram with 100 bins I determine the discrimation point between background and root by calculating the bin-to-bin-difference based on a sliding average over 5 bins. Now I look for the transition area from the background to the object by determining the value, starting from low intensities, at which the bin-to-bin difference stops falling continuously. From there I look for the point at which the bin-to-bin difference begins to rise continuously. In analogy to the tub, I am looking for the two lower edges of the tub. Finally, I define the intensity value, which is located in the middle between these points, as the threshold for the binarization of the image.

When parameterizing the analysis script, one of the two following methods for determining the threshold can alternatively be selected. The first alternative method selects a small square background part of the image to determine the average background intensity and then calculates the threshold as averaged background intensity plus a fixed offset.

The second method takes into account the absolute image size and the default thickness of an *Arabidopsis* root tip of about 100 µm (Müller-Reichert, 2010). From this I can estimate the area of the image which is covered by the root assuming the root stretches from one border of the image to the other and does not bend. Then I sort the pixels of the image by increasing intensity. To get a binarized representation of the image I use the intensity value as a global threshold which corresponds to the ratio of area covered by the root.

Applying a perimeter function to the binarized image finally yields an image matrix only containing the outline of the objects in the image (Figure 9C).

3.3.4 Artifact removal

The outline detection algorithm calculates the outline of any objects visible in the binarized image including artifacts like water drops or labels of the laboratory equipment. Such unrelated objects should be excluded from the analysis (for an example see Figure 11B). Therefore, I added an artifact removal function to the image analysis pipeline.

The artifact removal function is actually a determination of the size of all the individual objects present on the image. All detected objects are sorted by size. The assumption here is that the root is the largest of all objects in the image. All significantly smaller objects, if any, have nothing in common with the root and can be ignored. Therefore, in a first step I classified all objects in the image by size which in turn is estimated by the length of the outline in pixels. In the following step, all objects smaller than 50 percent of the size of the largest one were removed. The 50 percent threshold ensures that only small parts are removed and avoids unwanted removal of parts of the root in case the outline of the root is split into several parts.

For classifying the objects I used a connected component approach which assigns all pixels to the same object given the respective pixels are connected. As a criterion for whether two pixels are connected to each other, I have chosen the Moore neighborhood with a Chebyshev distance of 1. In the Moore neighborhood, which is named after the American mathematics and computer science professor Edward Forrest Moore, all pixels in a square grid that touch either via a common edge or a common corner are considered to be adjacent. In particular, pixels lying diagonally to one another also apply here as neighbors. The Chebyshev distance, named after the Russian mathematician Pafnuty Lvovich Chebyshev, is a measure in the unit of pixels for the distance between two pixels on a square grid. In contrast to the geometric

(Euclidean) distance, diagonal steps are counted exactly the same as horizontal or vertical steps. In connection with the Moore neighborhood, the Chebyshev distance specifies the maximum distance in pixels that can be two pixels apart in order to be considered neighbors. Effectively, a Chebyshev distance of 1 is the smallest possible distance and means that the pixels must be directly adjacent to one another and no gaps are allowed between them. In summary, a Moore neighborhood with a Chebyshev distance of 1 means that all pixels that are horizontally or vertically or diagonally immediate neighbors are considered to be connected to one another.

3.3.5 Centerline calculation

A central element for creating the kymograph is the calculation of the centerline along the longitudinal axis of the root. The centerline is an imaginary line that runs from the tip along the middle of the root to the point at which the root leaves the image. This line is required later for the calculation of the mean concentration at each point of the root. The centerline serves as kind of a track for a sliding window that calculates the mean intensity for each position along the axis.

The centerline itself is also determined by means of a sliding window in the following named the "preliminary window" that, starting from the center of the image, slides horizontally or vertically across the image to the right and left. Thus, the track for the preliminary window are just the centerlines of the whole window in x- or y-direction. Whether the window is sliding horizontally or vertically depends on the orientation of the root and changes dynamically during the calculation process.

The calculation of the centerline comprises several individual steps:

- Calculation of the slope of the root in the center of the image. This is required for the starting orientation of the sliding window (top-bottom or left-right).
- Calculation of the right-hand section of the centerline from the center of the image to the end of the root at the border of the image (Figure 9E). The line is calculated using a rectangular sliding window that moves forward in a horizontal or vertical direction depending on the current angle of the root and follows the path of the root in a stepped line.
- Calculation of the left-hand section from the center of the image to the tip of the root (Figure 9F).
- Union of the two sections into a single line. The centerline is now available as a vector of x/y-coordinate pairs.

In detail, the computation of the centerline works as follows: The basis of the preliminary sliding window calculation is a rectangle whose sides are parallel to the border of the image. Its longitudinal side spans the total range of the image. The narrow side of the window has a fixed length of 10 percent of the corresponding side of the image. Therefore, the area covered by the preliminary sliding window is always $x \times y \times 0.1$ pixels.

The rectangular area of the window serves as a binary mask which cuts down the outline into two separate lines if the root crosses the window perpendicularly. The goal is now to find the point that is exactly centered between these two lines. To do this, I look at the two lines

as two independent geometric objects, the centers of which can be described mathematically by the centers of mass of all the respective pixels. The desired center point of both lines then lies halfway along an imaginary line between the two centers. In short, the two centers of mass of the lines are determined first and then the center point between the two centers of mass.

To determine the two centers I apply a k-medoids function with $k = 2$ to the coordinates of the pixels in the mask. The output of the k-medoids function are two pairs of coordinates which represent the center of the corresponding centroids. The center point of a line between these two centers is considered being part of the centerline of the root. Thus, each window produces a single pair of coordinates of the centerline.

Moving the preliminary window along the root provides the points forming the centerline. Since I do not know the centerline in the start and cannot use them as a track - I just want to calculate them - I set the track for the preliminary sliding window dynamically. Starting in the center of the image I move in a two-step approach into two opposite directions and combine the two parts of the centerline afterwards.

I assume that the root extends from one side of the image to the other and therefore either crosses the horizontal or the vertical centerline of the image or both. However, it is not known at which angle the root intersects the central axes of the image, i.e. whether the root is oriented from top to bottom or from left to right. This information is required to decide whether the sliding window should start horizontally or vertically. Before the main calculation, I do a preliminary k-medoids and center point calulation with a horizontal sliding window starting from the center of the image, which is used to determine the orientation of the root. I shift the window slightly to the right along the horizontal axis of the image and again calculate the centroids of the k-medoids and its center point. If I have collected a sufficient number of data points I calculate the angle between the first and the last data point.

I use this angle to adjust the direction and position of the sliding window. If the absolute value of the angle is equal or smaller than 45 degrees I continue using a horizontal sliding window. If the angle is larger than 45 degrees I turn the sliding window by 90 degrees and also move it towards the top of the image (in an analogous manner: if the angle is smaller than minus 45 degrees to the bottom of the image). After computing and storing the position of the centroid I recalculate the angle and apply the same procedure again. Depending on the angle of the current data points, the sliding window will continue moving horizontally or vertically until it reaches the border of the image. The stepwidth of the sliding window is one pixel.

In a second step, I restart from the center point of the image and move the sliding window into the opposite direction (starting with movement to the left) until I reach the border again. Finally, I concatenate these two sets of coordinates to a single two-column vector of data points representing the centerline of the root.

In the course of the calculation, some special cases must be taken into account: If the root tip does not touch the border of the image and the root terminates within the image the k-medoids calculation will probably fail and result in an incorrect value. An incorrect value can be detected by checking the distance to the previous value. If the distance is large ("jump") I assume that center point calculation was not successful. I use this feature to detect the root tip by applying a threshold for the maximum distance of two points of the

centerline and the maximum angle of the data points. If the end of the root was determined in this way, the sliding window terminates.

To ensure a proper definition of the centerline of the root tip I connect the root tip to the border of the image by a straight line tilted by the last angle passing the threshold. This is also important insofar as the root grows slightly into the direction of the tip during the experiment and the centerline calculation of the first image serves as a reference for all consequent images. By extending the center line beyond the tip, values can also be calculated for images in which the root is slightly longer compared to the root in the first image.

After calculating the coordinate pairs of the center line, I compute the angle of the centerline in relation to the horizontal in each point. I also use a sliding window for this. The value for the angle results from the angle of the two outermost points within the window. For practical reasons, I defined the width of the sliding window over a distance of 75 coordinate pairs (corresponds to 0.10 mm - 0.15 mm depending on the angle and the image resolution).

Finally, the result of the centerline calculation is a two-dimensional array that holds the coordinates of the centerline and a one-dimensional array of the same length that holds the angles in each position of the centerline.

3.3.6 Thickness calculation

The root tip of an *Arabidopsis* plant is about 100 µm thick (Müller-Reichert, 2010). I use this information to perform a plausibility check for the root detection and to draw conclusions about the quality of the images. If the measured thickness is significantly above or below this value, it can be assumed that the examined object is not a root or that the detection of the root failed. In addition, the root thickness is required later when calculating the kymograph to select the size of the sliding window.

For measuring the average thickness of the root I use a similar approach as for creating the kymograph itself based on a sliding window along the centerline (for a detailed description of the algorithm see Section 3.3.8: Kymograph generation by line tracking). However, for thickness calculation I only use a small set of eleven windows at predefined positions in the inner area of the root (eleven positions in a range between 25 % and 75 % of the length of the centerline with a step size of 5 %). At each position I mask the outline of the root by a rectangular box perpendicular to the centerline and apply a k-means algorithm with $k = 2$ to the masked data. The box has a width of 8 pixels. It is as long as the largest side of the image. For each window the thickness is calculated as the Euclidean distance between both centroids. Finally, the overall thickness of the root is calculated as the median of the thickness values for the individual sliding windows.

3.3.7 Quality control

One advantage of an automated analysis is, that it can be easily applied to any dataset fulfilling the formal requirements for analysis. However, the image data may be invalid or of poor quality. In extreme cases, the images could also be empty or contain other objects such as leaves instead of roots. The basic assumption of a root analysis algorithm is that it is only applied to images of roots. If someone applies the algorithm to an image series of leaves the results will not be meaningful. Therefore, the minimum requirement for applying the

algorithm is that the images show actually roots. The user of the algorithm is responsible for ensuring that this condition is met.

In addition, there are less obvious assumptions that truely require proper quality control. One additional assuption is that the images show only one single root stretching from one end of the image to the other. This assumption is violated in the case of a root that bends and grows into the opposite direction (Figure 11A). A manual observer can easily detect the problem and remove the dataset from the analysis or adjust the analysis to such special cases. However, the algorithm has no magic eye and is not able to detect the fault. It treats the bending root as one large piece of root which of course leads to wrong results.

One possible but time-consuming solution would be to extend the line tracking algorithm towards detecting any shape of the root. I decided to use a simpler approach: At different points of the algorithm I set up quality check routines which doublecheck the intermediate results and classify the results as wrong if the check is not passed. A bending of the root with growth in the opposite direction is detected by measuring an exceptionally large thickness. This also works if the two parts of root do not touch each other directly and there is some space in between, since the maximum distance between the object boundaries within the measuring window is used to measure the thickness. On the other hand, if the root is only slightly curved, the thickness can be measured correctly. In this case the sliding window simply follows the course of the root.

In order to detect curvatures of the root and similar issues that lead to a reported thickening of the root, I introduced a threshold value for the valid thickness. The common value for the thickness of an *Arabidopsis* root tip is about 100 µm (Müller-Reichert, 2010). By examining various series of images, I learned that the thickness does not deviate more than 20 percent up or down. I added a small safety margin to this value and applied a range of default thickness ± 50 % as a quality check point.

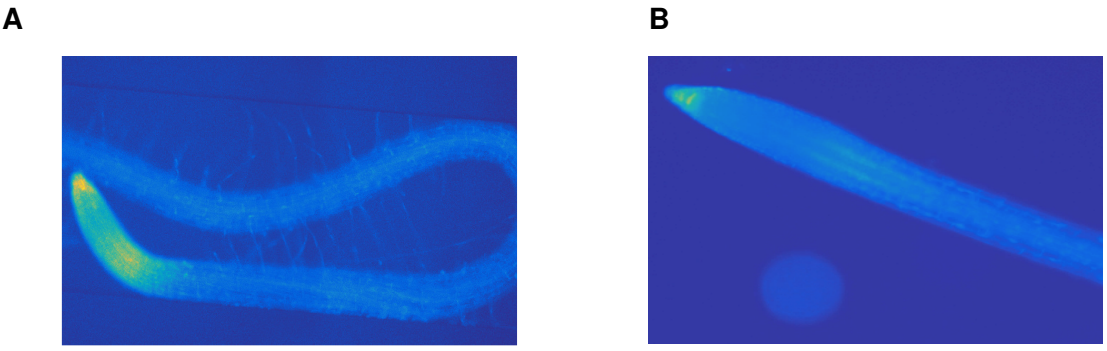

Figure 11. Examples for the necessity of automated image quality control: bending root (**A**), waterdrop (**B**). A bending root cannot be processed properly by the object detection algorithm and would lead to incorrect results in further calculations. However, it will not pass the quality check point. Results from the detection algorithm are dismissed because the measured thickness is not in the common range of 100 µm ± 50 %. Artifacts like waterdrops are detected by the outline detection and removed automatically.

The quality check described above is only applied to the first image of the image stack and decides whether the image data set can generally be used for the automatic analysis. It

happens, however, that the first image is of perfect quality, but some subsequent images are unusable. In this case, the data set can be used when the defective images are sorted out. For this purpose, I applied an automatic quality detection of the images by comparing the mean intensity of the background of an image with the mean background intensity of the previous one. Images classified as bad quality due to high differences in background intensity were replaced by the previous image. In order not to impair the time axis of the kymograph, unusable images cannot simply be discarded, but must be replaced by similar images. A warning message in the R console informs the user about the decision of the algorithm. Such failures can occur by human errors e.g. accidentally switching on the lights or opening the door of the microscopy chamber.

3.3.8 Kymograph generation by line tracking

After the preprocessing calculations have been completed, the kymograph can finally be created. The essential part here is the calculation of the mean intensity along the centerline. At this point it is important to mention that the preprocessing (calculation of the center line) is only done for the very first image. The result of this calculation is then used as a reference for all images. This approach unifies the calculation and improves the performance of the algorithm.

For the kymograph calculation algorithm I apply a sliding window of a fixed width (default value: 6.4 µm) and a height of two times the thickness of the root along the centerline. The width of the sliding window has an influence on how much the kymograph is smoothed. The wider the window, the stronger the smoothing. The smoothing in turn is related to the recording quality of the camera equipment. The worse the image quality, the more useful a higher smoothing is. On the other hand, the smoothing should of course be chosen as small as possible in order to achieve the highest possible accuracy. In my computations, I based the width of the window on a 15th of the default root thickness (100 µm) and rounded it to whole pixels. For example, using images with a resolution of 1.6 µm/pixel this results in a window width of 4 pixels corresponding to 6.4 µm.

The angle of the sliding window is perpendicular to the centerline. The step width has a fixed value of 0.5 pixels.

Calculating the mean intensity of each window provides a single vector of floating point values. This calculation procedure is repeated for all images of the time-lapse movie. Although the root is growing over time and therefore slightly moving I use the same track for all images for easy comparability of the values. Since the long side of the sliding window is twice as large as the root thickness, slight moves of the root will not affect the result. The matrix composed of all vectors is the mathematical representation of the kymograph.

3.3.9 Intensity shift detection and correction

Because the creation of the crestline plot (see Section 3.4) is sensitive to intensity flaws and artifacts they must be detected and removed. Abrupt changes in intensity are mostly caused by interfering light in the experimental chamber (e.g. someone turns on the lights) or by changes in the setup of the microscope during the experiment. These artificial changes

are not caused by biological processes and should be removed from the data before further processing.

In my experience, an artifact can be assumed if the change of the overall intensity between two consecutive images is larger than ten times the average change between each pair of consecutive images. I correct this obvious error by calculating the size of the intensity shift and subtracting it as an offset from all subsequent images. To do this, I calculate a vector of intensity differences of each pair of images along the spatial axis of the kymograph. Then I calculate the sum of the absolute values of the individual differences for each vector. The global change in intensity from one image to the next is described here by a single number. As a reference I use the mean value of all global changes in intensity. If the global change in intensity from one image to the next exceeds ten times the mean value, I assume an external incident and set the global change in intensity at this point in time to zero.

From a mathematical point of view, I take the difference vector of two consecutive rows in the kymograph matrix as an offset and subtract these differences from all subsequent rows, starting with the row in which the jump in intensity, i.e. an extraordinarily high difference to the previous row, was determined. After applying the intensity shift correction, this row contains exactly the same values as the previous row, so in the graphical representation the kymograph shows two identical lines at this point in time.

If there are several jumps in intensity during the experiment, the correction procedure is repeated several times, whereby shifts upwards and shifts downwards can occur. The new offset is simply added to or subtracted from the previous one. As a result, a temporary increase and decrease of the intensity caused by turning on and off the lights will be removed almost completely. However, a significant intensity change which affects only one single image frame will not be removed assuming a single technical outlier. This outlier might be caused by errors of the image acquisition and therefore is assumed to not affecting the kymograph data unduly.

Ideally, the intensity shift detection should be applied to the raw image data because here one would be able to detect an artificial change of the intensity by analyzing the background intensity. However, I decided to do this correction after kymograph generation for practical reasons: Due to the modular structure of my algorithm I can apply it to cases for which I do not have the raw data but only the kymograph data (for example to kymograph data from publications). Furthermore, the calcium sensor R-GECO1 is only expressed in the cytosol. The cytosol in turn covers only a small fraction of the plant cell. As a consequence, a large amount of background data is already incorporated in the calculation process of the kymograph. In other words, a strong increase in the overall background intensity also leads to a significant increase of the intensity covered by the kymograph data. Therefore, no disadvantages are to be expected if I do not already apply this correction to the raw data but to the matrix of the kymograph data.

Since the intensity shift correction is only relevant for the further processing of the data, I applied the correction algorithm to a copy of the kymograph data, which then serves as input for creating the crestline plot. The original kymograph data array is not modified. Therefore, intensity artifacts are only removed temporarily for processing of the data but are still visible for the user if he visualizes the kymograph data.

3.4 Crestline plot

The calcium wave is formed by an increase in the intracellular concentration of calcium, which spreads from its starting point in both directions along the root. However, the maximum concentration that is reached over time at a certain position is not the same for all positions of the root. The global maximum is reached around the starting point of the wave. With increasing distance from the starting point, the maximum value decreases and the wave weakens. Therefore, for a proper analysis of the wave it is necessary to incorporate the distant parts of the wave accordingly.

If you imagine the kymograph as a topographical map of a landscape in which the geographic height is described by the calcium concentration and the two spatial axes are represented by time and the position along the root, then the result is the image of a mountain range with a summit in the center. A ridge in the form of a slightly curved crestline descends from this summit in two directions. If you now look at the intensity profile in the time direction, which corresponds to a vertical section through the mountain range along the respective axis, the following graph results: the intensity remains at approximately the same level for a certain time, then the intensity rises steeply, reaches a sharp peak and then drops again to return to the basic level (Figure 13C, D). This profile is similarly found at all positions of the wave along the root. The further away the position is from the starting point of the wave, the flatter the rise and fall and the smaller the peak is compared to the intensity profile of the starting point of the wave. To compensate for this weakening of the wave with increasing distance I decided to scale the kymograph according to its local maximum over time at each position. Following the mountain vocabulary I called the scaled kymograph "Crestline Plot" (Figure 4B, 13A, 13B). In the crestline plot the calcium wave, which spreads over a large area on the kymograph, shows up as a thin, clearly recognizable line. The crestline plot is the graphical representation of a matrix c_{ij} which is calculated by scaling each column k_{*j} of the kymograph matrix k_{ij} according to its minimum and maximum:

$$c_{ij} = \begin{cases} \frac{k_{ij} - \min(k_{*j})}{\max(k_{*j}) - \min(k_{*j})} & \text{for } \max(k_{*j}) > \min(k_{*j}) \\ 0 & \text{for } \max(k_{*j}) = \min(k_{*j}) \end{cases} \tag{1}$$

In the following I name the processed data c_{ij} "crestline matrix" and its graphical representation "crestline plot".

3.5 Wave analysis

The analysis of the calcium wave is based on the crestline matrix of the kymograph and comprises several consecutive steps: detection of the crestline, calculation of starting point and time and the wave speed into both directions. The resulting values of the analysis are printed to the console and presented as a graphical output based on the crestline plot (Figure 9D, F). The graphical output consists of a modified version of the crestline matrix c_{ij} with additional marks and lines. Furthermore, the analysis function returns the resulting values as a list for further data processing.

For a proper analysis of the wave I need the coordinates (row and column indices) of the actual crestline within the crestline matrix. The simplest approach to find the crestline

would be to just find the maximum in each column which equals 1 per definition. However, in practice this method is not optimal because the peak in each column extends over several data points along the time axis, all of which have a similarly high intensity value, and cannot be clearly attached to a specific point in time. In addition, the maximum value does not necessarily coincidence with the center of the peak. Therefore, I applied a center-of-intensity algorithm to the crestline matrix inspired by the center of mass of physical objects. I calculated the crestline vector p as the row index p_j of the peak of the wave at each column from the crestline matrix c_{ij} with n_i rows and n_j columns as follows:

$$p_j = \begin{cases} \lfloor \frac{\sum_{i=1}^{n_i} c_{ij} * i}{\sum_{i=1}^{n_i} c_{ij}} + 0.5 \rfloor & \text{for } \sum_{i=1}^{n_i} c_{ij} > 0 \\ 0 & \text{for } \sum_{i=1}^{n_i} c_{ij} = 0 \end{cases} \tag{2}$$

In order to make the exact position of the crestline vector visible in the graphic output, the pixels of the crestline vector were colored dark blue and can therefore be easily recognized as a thin line (see blue line in Figure 14A, B).

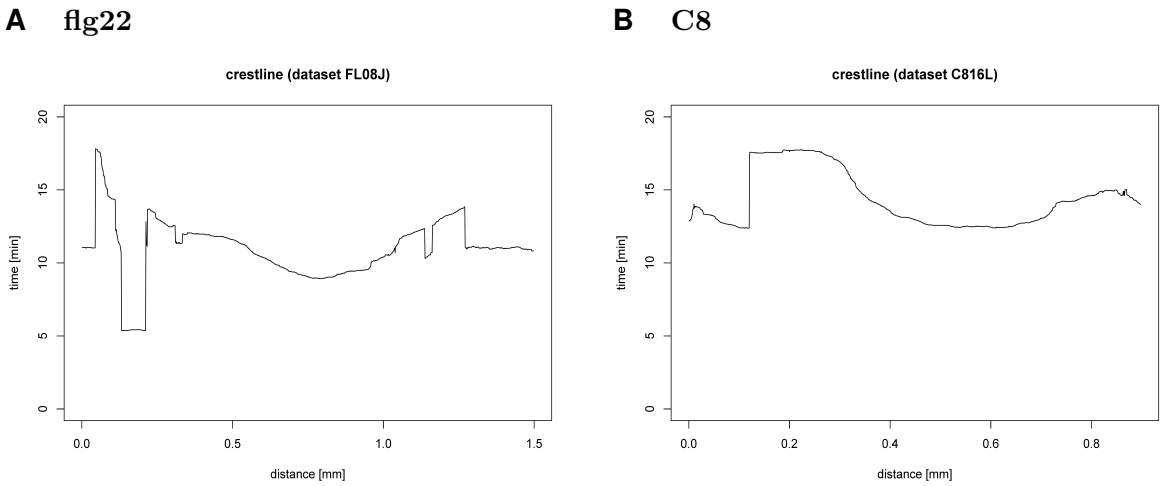

Figure 12. Crestline vector: The crestline can be plotted as a function of the distance from the root tip. Two crestlines of a stimulation with flg22 (**A**) and the chitin variant C8 (**B**) are shown as examples (see Figure 13A and 13B for the corresponding crestline plots). The starting point of the wave is characterized by a minimum of the crestline vector.

The crestline vector builds the base for the further analysis of the wave (Figure 12). For the following calculations I consider the crestline vector as a function of time in the Cartesian coordinate system: the x-axis represents the position along the root, the y-axis the time at which this position of the root reaches the crestline, i.e. its highest intensity (in the Cartesian coordinate system, the time axis points from bottom to top while in the kymograph it points from top to bottom). In this view, the ideal crestline vector has a U-shape, with the beginning of the calcium wave being represented by the global minimum and the end by the two maxima. In addition, the following must be taken into account: In some experiments, an increased calcium concentration was also observed at the outermost root tip. It is possible that there is an additional small wave spreading from the tip. However, this has not yet been sufficiently clarified. For the analysis, I will therefore ignore a wave spreading from the tip.

The analysis of the calcium wave comprises the calculation of the following values:

- Start position
- Start time
- Propagation speed

3.5.1 Start position of the calcium wave

The first part of the analysis aims to determine the start position and time of the wave. The start position is calculated first, because the calculation of the start time is then made easier. Since the crestline vector often has an irregular course or has faults, I determine the start position in a two-step process, in which I gradually increase the accuracy: In a first step, I roughly determine the spatial area along the root where the wave starts. In a second step, I determine the exact starting point within this area.

To roughly determine the range of the starting point, I first smooth the crestline vector very strongly using a sliding median with a window width of 50 µm, so that small fluctuations have no influence on the following calculation. In particular, local minima and maxima that arise from small fluctuations will be eliminated. Then I look for all local minima and maxima that are on the smoothed crestline curve. In the ideal case there is only a single minimum, namely that at the starting point of the wave. If a secondary calcium wave also starts running from the root tip, then there is another minimum at the root tip. In order to exclude this wave from the analysis, I ignore all minima that are very close to the root tip, given there is at least one further minimum in the direction of the shoot. Analogously, I ignore minima that are in close spatial proximity to local maxima, since they are probably due to fluctuations or artifacts (distance to the maximum <200 µm). Such fluctuations tend to occur at the end points of the wave, since the calcium signal is weak there and fluctuations therefore have a stronger effect. The first minimum close to the root tip, which remains after these corrections, marks the position at which the starting point of the primary wave is roughly located.

Following my experience, I assume that in the first step the position of the starting point was determined with an accuracy of ± 100 µm. In the second step, I only slightly smooth the crestline vector with a sliding median of 20 µm width and determine the global minimum within the 200 µm wide range that was the result of the first calculation. The global minimum marks the position x_s on the root axis where the primary calcium wave starts.

3.5.2 Start time of the calcium wave

The starting position x_s represents the position along the axis of the root where the crestline has its minimum with respect to time. However, the actual starting time of the wave is even smaller because the crestline represents the maximum intensity at this position. The actual starting point is the point in time at which the intensity started to rise above the basal level. However, it is not easy to determine this point directly, as the increase in intensity usually takes place in a gentle curve accompanied by fluctuations. I therefore determine this point indirectly by going down from the top and interpolating linearly. To do this, I use the intensity profile of the kymograph at the start position x_s over time and calculate the

increase in intensity between a point in time with medium intensity and the point in time at which the intensity reaches its maximum (Figure 13). Assuming a constant increase in intensity during the entire process, I determine the point in time at which the straight line intersects the basal level. I define this point in time as the actual start time of the wave.

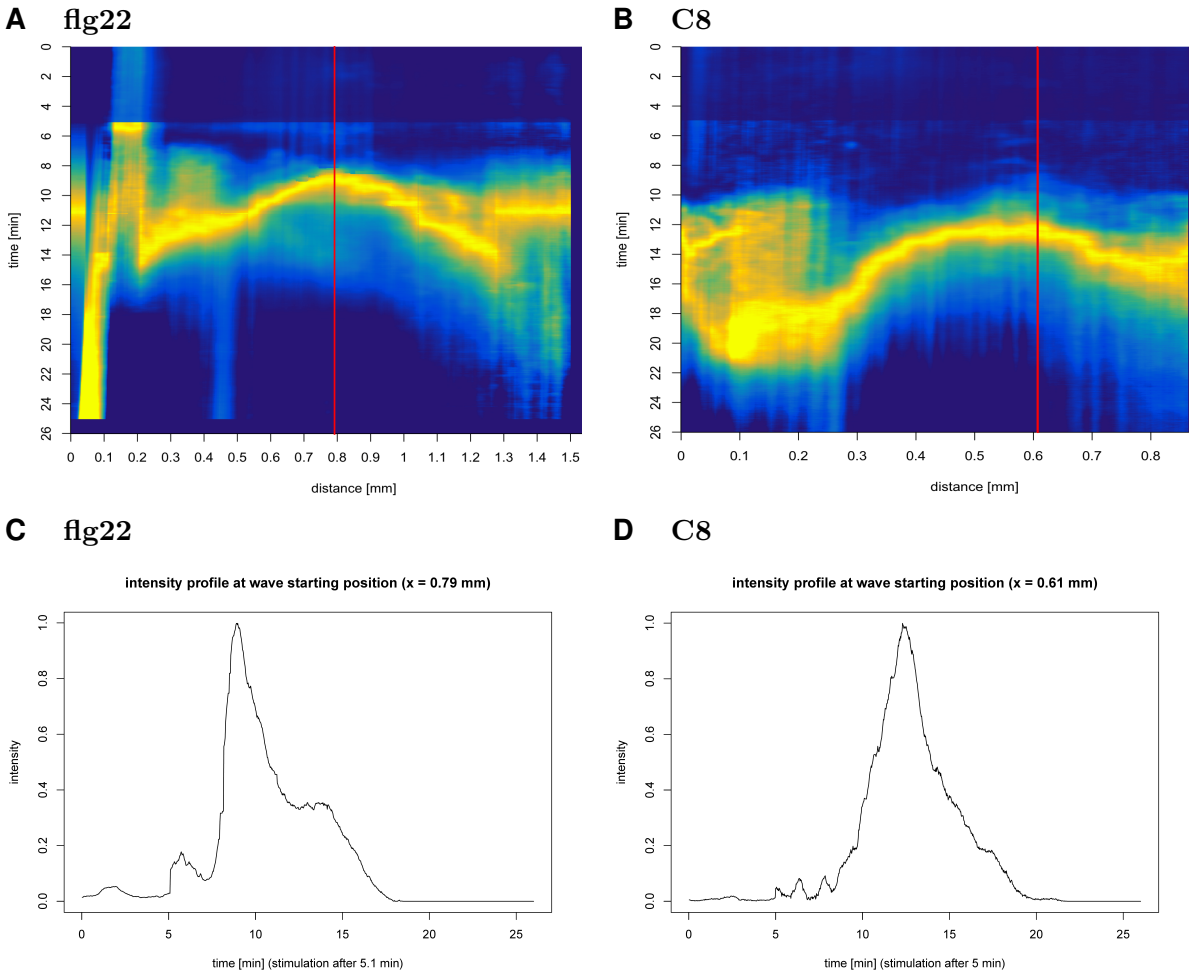

Figure 13. An intensity profile of the crestline plot is used to calculate the exact start time of the wave. Two crestline plots of a stimulation with flg22 (**A**) and the chitin variant C8 (**B**) are shown as examples. The red line in the crestline plot marks the position where the intensity profile for flg22 (**C**) and C8 (**D**) was extracted. An intensity value of 0 represents the lowest, a value of 1 the maximum intensity. One can clearly see how the intensity increases to the maximum after the stimulation and then falls back to the previous level. There are small fluctuations at the base of the slope, which make it difficult to determine the exact start time. For this reason, the starting time was determined by means of linear interpolation from the top downwards.

In detail, the calculation is done as follows: First, I exclude all values from the calculation before the time point of stimulation to avoid incorrect results caused by intensity artifacts or fluctuations. I limit the calculation to the remaining intensity values ks_{ij} which I named kymograph matrix after stimulation:

$$ks_{ij} = \begin{cases} k_{ij} & \text{for } i >= i_{\text{stim}} \\ 0 & \text{for } i < i_{\text{stim}} \end{cases} \tag{3}$$

To calculate the increase in intensity needed for the interpolation, I determine the time difference between half-maximum and maximum intensity. To do this, I have to find two defined points in time. The first one is the point at which the intensity first reaches half the value between minimum and maximum. This point is represented by the row index i_{half}. The second one is the point in time when the intensity is at its maximum. This point with the row index i_{max} corresponds to the value of the crestline vector p_j at the position $j = x_s$. Mathematically, the indices of the two points in time can be described as follows:

$$\begin{aligned} i_{\text{half}} &= i_1 = \min([i_1, i_2, ...i_n]), \\ &\quad [ks_{i_1 j}, ks_{i_2 j}, ...ks_{i_n j}] >= \min(ks_{ij}) + 0.5 \cdot (\max(ks_{ij}) - \min(ks_{ij})), j = x_s \\ i_{\text{max}} &= p_j, j = x_s \end{aligned} \tag{4}$$

The index i_{start}, which marks the start time of the wave, can be estimated by interpolation:

$$i_{\text{start}} = i_{\text{max}} - 2 \cdot (i_{\text{max}} - i_{\text{half}}) \tag{5}$$

Finally, the starting time of the wave is calculated as the delay between the time point of stimulation and the time point with the row index i_{start}. In the graphical output of the analysis, the time point of the stimulation is marked by a horizontal dashed line. The position of the wave start and the two end positions that were used to calculate the speed are marked as solid vertical lines.

3.5.3 Propagation speed of the calcium wave

The averaged speed of propagation in the direction of the tip and in the direction of the shoot is calculated from the time the wave took from the starting point to the respective ends. As end points, I define measuring points at a distance of 250 µm tipwards and shootwards from the starting point of the wave and calculate the speeds based on the associated time values of the crestline vector. Additionally, I calculate the wave speed into the direction of the shoot using the starting point and the last available value at the borderline of the image. Optionally, the intervals for calculating the speed can be determined by calculating the speed within a small sliding window starting from the starting point into both directions and stopping if the speed within the window drops below a threshold. This algorithm for finding the end points of the wave was applied to the example datasets presented in this thesis. The positions used for calculating the speed values are marked by vertical lines in the graphical output (Figure 14A, B). All results of the analysis are stored as a data structure in the software for further use and also printed in the console window (Figure 14C, D).

A flg22

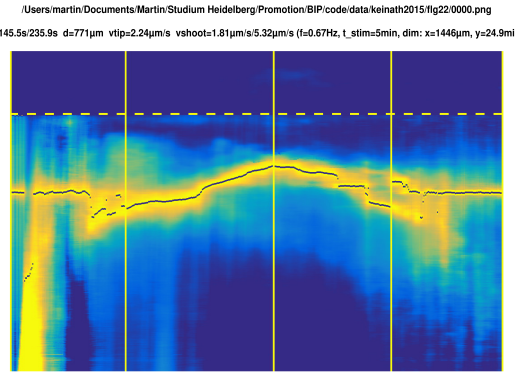

B chitin

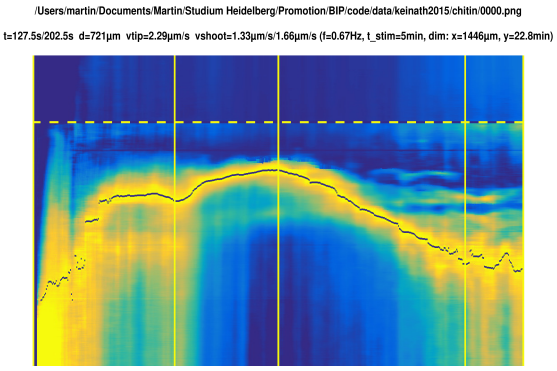

C flg22

```
> demo1()
WARNING: Image file 0444.png was removed due to bad quality.
WARNING: Image file 0445.png was removed due to bad quality.
filename: "0000.png"
wave starting time after stimulation: 2.42 min
wave starting time after stimulation (until peak level): 3.93 min
tip starting position: 0.0026 mm
wave starting position: 0.7732 mm
distance from tip: 0.7706 mm
speed: wave -> tip:   v = 0.0022 mm/s
speed: wave -> shoot: v = 0.0018 mm/s
speed: wave -> shoot border: v = 0.0053 mm/s
Image processing runtime total:  1.71  minutes.
```

D chitin

```
> demo2()
WARNING: Image file 0715.png was removed due to bad quality.
filename: "0000.png"
wave starting time after stimulation: 2.12 min
wave starting time after stimulation (until peak level): 3.38 min
tip starting position: 0.0026 mm
wave starting position: 0.7232 mm
distance from tip: 0.7206 mm
speed: wave -> tip:   v = 0.0023 mm/s
speed: wave -> shoot: v = 0.0013 mm/s
speed: wave -> shoot border: v = 0.0017 mm/s
Image processing runtime total:  1.54  minutes.
```

Figure 14. The result of the automated wave analysis is a modified kymograph in which relevant measures are marked with a line. In the examples of stimulation with flg22 (**A**) and chitin (**B**) the crestline, i.e. the point in time of the highest calcium concentration, is marked with a thin blue line. The time of stimulation is shown as a horizontal dashed line in yellow. Three vertical lines mark the positions along the root axis, which are used to calculate the average speed of the wave in the direction of the tip and in the direction of the shoot. The results of the calculation and other information are printed in the console window of the analysis script: exemplary text output of a stimulation with flg22 (**C**) and chitin (**D**).

3.6 Input requirements and data preprocessing

The raw data input of the algorithm for the image analysis has to be a tif-formatted file which contains a series of single images, or a series of single png-formatted files, the file names of which are numbered. The image intensity reflects the concentration of calcium in the root over time. Because the calcium sensor in the plant is a fluorescent protein that emits nearly monochromatic light the image series in general only provides data from one detector channel of the microscope. If the file contains several channels it is necessary to preprocess the image file with appropriate image editing software to either remove the irrelevant channels or to combine the existing channels into one channel by saving the image as grayscale image.

My algorithm was developed and tested on about 70 different datasets kindly provided by my collaboration partners from the Grossmann Lab. Since these datasets were unpublished at the date of starting my thesis I additionally used freely available data for the demonstration of my algorithm. With this I wanted to be able to provide practical examples for my publicly available algorithm. For this purpose, I applied my algorithm to two datasets provided in the supplemental section of Keinath et al. as video files (Keinath et al., 2015). My software works on microscopic raw data therefore I had to prepare the published data to convert them back into raw data. The provided videos do not consist of single channel grayscale images but of processed images converted into a 7-color heatmap (black, blue, cyan, green, yellow, red, white). Therefore I developed and applied a reconversion algorithm into grayscale images before starting the analysis. Additionally I had to remove the scale bar, the characters of the time log and the stimulus description from the images. I did this by duplicating a small area above or beneath the characters and copying it several times into the area of the characters. The coordinates of the area were manually chosen by visual inspection of the video. Manual inspection of the images also revealed that a small number of individual images were characterized by a abnormal high background and image intensity probably caused by accidentally turning-on the lights. I applied an automatic quality detection of the images by comparing the background of an image with the background of the previous one. Images classified as bad quality images were replaced by the previous image (image #444 and #445 for the flg22 dataset, image #715 for the chitin dataset). For correct application of my automated wave detection I needed additional information of the datasets such as resolution, frame rate, and timepoint and duration of the stimulation. I retrieved this parameters from the information given in the video. The capturing of the video starts with timepoint -5:00 (assumed time scale minutes:seconds). Treatment is 1 µM flg22 from 00:00 to 05:00 for the flg22 dataset, and 100 µg/ml chitin from 00:00 to 05:00 for the chitin dataset. Therefore the starting point of the treatment was set to 5 minutes with a duration of 5 minutes (the algorithm starts with timepoint zero as the beginning of the dataset). The period time of the image acquisition was manually calculated by dividing the overall acquisition time depicted in the last image of the video by the number of images (flg22 dataset: (19:55 + 05:00), 998 images, T=1.5 s; chitin dataset: (17:45 + 05:00), 911 images, T=1.5 s). The resolution of the images was calculated by measuring the scale bar in the first image (length flg22/chitin: 76 pixels). Assuming a scale bar length of 200 µm according to the legend of figure 6A and 6B in Keinath et al. (2015) I got a resolution of 2.63 µm per pixel and a size of the images of 1.447 mm × 0.258 mm. I also learned from manual inspection of the images that the root tip is on the left side of the image and the shoot on the ride side, therefore tip detection and putative image rotation was not necessary. These preparations enabled me to successfully test my algorithm on datasets that were not available as raw data images.

4 Analysis of calcium signatures in plants

4.1 Chapter introduction

The purpose of the automated image analysis algorithm is to facilitate the visualization of the calcium wave and to provide a robust and reproducible quantification of the wave.
By means of this algorithm I analyzed the image data of different stimulation experiments with biotic and abiotic stimuli. For the experiments *Arabidopsis thaliana* seedlings were used with a genetically built-in calcium sensor which makes it possible to monitor the concentration of intracellular calcium with the microscope. The plants were stimulated with different elicitors: high concentrations of salt, bacterial peptides, components of the cell walls of fungi. The stimulation triggers a signal response associated with an increase in the concentration of intracellular calcium which spreads in a wavy manner towards the tip of the root and towards the shoot.

In communications technology, the term wave is primarily known as an information carrier in the form of radio waves. Some researchers claim that the mechanisms in cell biology are similar to those in telecommunications engineering, and they also apply information theory to biological processes (Adami, 2004; Schneider, 2010; Wagner, 2017). Following this idea, I calculated the information content of the calcium wave using information-theoretic methods and examined whether the calcium wave was able to transmit information from one plant cell to another.

4.2 Outside assistance

I received outside assistance by my colleagues Rik Brugman and Janos Löffler from the Grossmann Lab. Rik, who carried out the laboratory experiments together with Janos, brought in his many years of diverse experience with *Arabidopsis* stimulation. Rik supported me in quantifying the kymographs of the various stimulations by manually recalculating the results of my automated analysis and checking them for plausibility. Irina Surovtsova from the Biological Information Processing Group at the BioQuant Center of Heidelberg University supported me in applying information theory.

4.3 Wave characteristics in response to different stimuli

The response to biotic and abiotic stimuli shows different characteristics (Figure 15). Using high-resolution epifluorescence microscopy the calcium wave can be observed very well in response to biotic stimuli. However, after stimulation with high concentrations of salt the plant responds with a steep increase of the intracellular calcium concentration, which immediately propagates throughout the whole root. The wave is so fast that a visualization is not possible due to the temporal resolution limit of the current microscopy setup ($f < 2$ Hz). Measurements from other research groups have shown, that the wave was running at a speed of 400 µm/s through the plant (Choi et al., 2014). For the quantitative analysis of the calcium wave, I therefore focused on experiments with biotic stimuli.

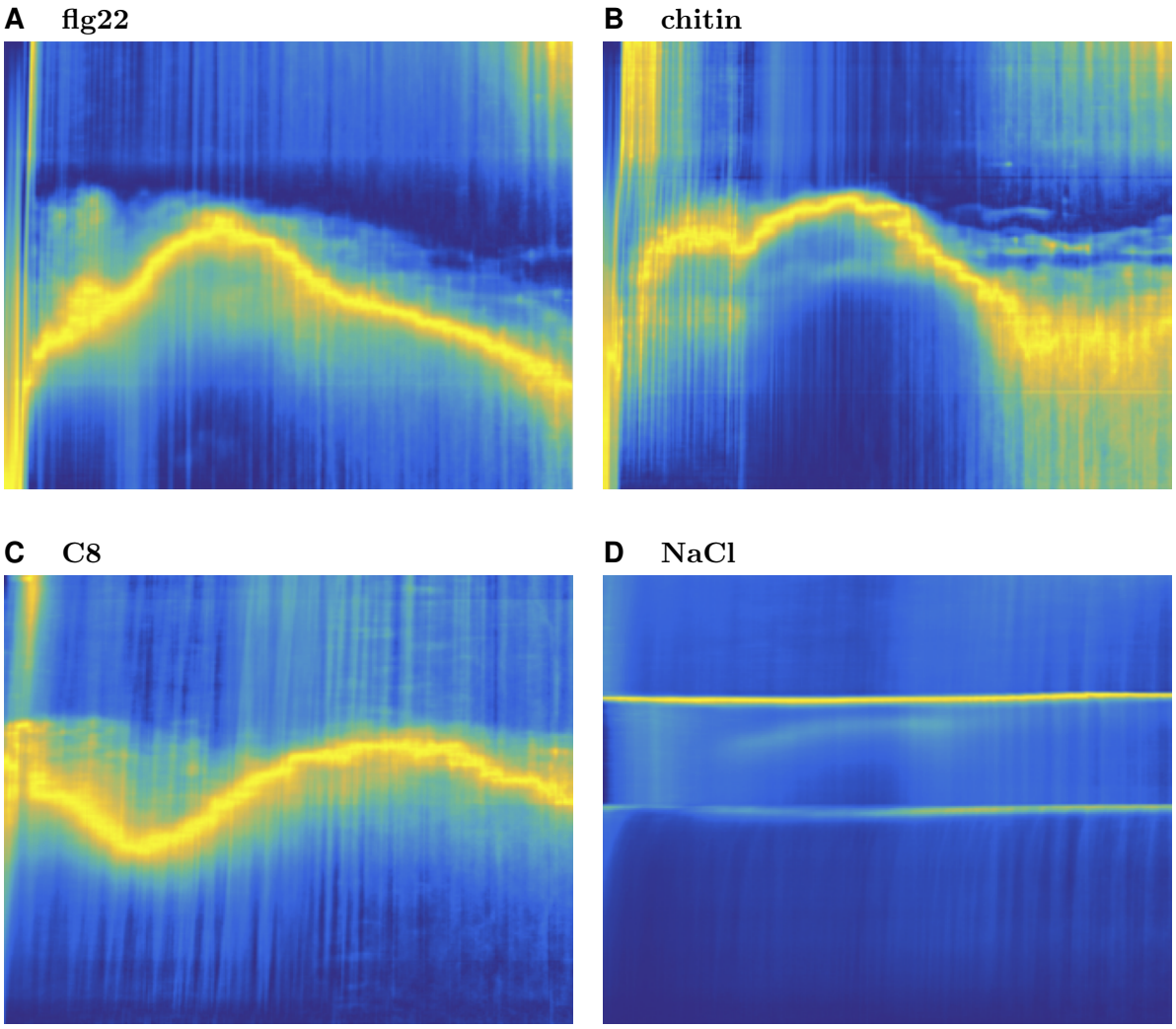

Figure 15. Representative crestline plots of the automated calcium wave analysis after stimulation with flg22 **(A)**, chitin **(B)**, C8 **(C)**, and NaCl **(D)**. While the crestline plots of flg22 and chitin or C8 show a certain similarity, the crestline plot of the stimulation with sodium chloride has a completely different appearance.

4.4 Information about different stimuli is encoded into calcium wave characteristics

In the following, I examined whether different stimuli lead to different wave characteristics. In the data one can see that abiotic and biotic stimuli exhibit distinct calcium responses. Biotic stimuli trigger a slow local wave with a speed between 1 µm/s to 5 µm/s. The wave fades out a few millimeters away from the starting point of the wave. The abiotic stimulus salt however triggers a global wave that can be detected in the upper parts of the plant. The speed of the wave is quite high and was not exactly measurable with the equipment of the lab of my collaboration partners. Literature data propose a speed of around 400 µm/s for a wave triggered by high concentrations of salt.

4.4.1 Local wave in response to a biotic stimulus

The local wave, triggered by flg22, C8 or chitin, has some striking characteristics: The main wave starts roughly 90 seconds after uniformly stimulating the entire root at a position within the elongation zone of the root around 500 µm away from the tip and then spreads into both directions, towards the tip and towards the shoot. At the same time, a smaller wave starts from the tip and runs towards the shoot until both waves merge. The intensity of the wave from the tip is significantly lower than the main wave and in some experimental datasets it is not detectable. The small wave from the tip is not subject to the automated wave analysis because its strength is too low.

The key point here is the fact that the overall delay after stimulation differs within the individual experiments but in all experiments the small wave at the tip and the main wave around 500 µm away start at exactly the same time. In this context it is important to mention that the stimulation treatment is applied to all parts of the root at the same time. The observed reaction, however, starts at one or two point-shaped positions of the root. So far there is no clear explanation for this phenomenon. All further discussion only refers to the main wave starting at a position in the elongation zone.

The averaged propagation speed of the wave is about 1 µm/s to 5 µm/s. The speed values in both directions are similar with the speed to the shoot being slightly faster than the speed to the tip. At the starting point the current propagation speed is larger than the average, but slows down during its way. The curve of the wave roughly follows a quadratic line. The intensity of the wave drops very fast with increasing distance from the starting point. Thus, the propagation range of the wave from the starting point is limited to roughly 1 mm. Stimulation experiments with flg22 and the chitin polymer C8 show only one wave, however for the ordinary chitin built-up by a variable number of N-acetylglucosamine monomers in many cases a small secondary wave can be observed starting about 5 minutes after the first wave. Interestingly, this secondary wave coincides roughly with the withdrawal of the stimulus (the stimulus ist removed 5 minutes after the start of the stimulation).

4.4.2 Global wave in response to high salt

The calcium wave in response to salt starts immediatedly after exposing the root to a high concentration of sodium chloride. There is no delay. The propagation speed of the wave seems very high. Due to the limited frame rate of the camera in combination with the limited observation window of the applied microscope it is not possible to calculate the speed and the starting point of the wave properly. The wave seems to start all over the root at the same time. However, from literature it is known that the wave travels with a speed of about 400 µm/s from the root to the shoot (Choi et al., 2014). Furthermore, there is no measureable variation of the intensity with respect to its starting position. The intensity increases at all positions to a comparably high level and drops a few seconds later to the previous level. A second wave can be observed five minutes later when the stimulus is removed from the plant. Due to the exact coincidence in time with the withdrawal of the stimulus, it can be assumed that this wave is also caused by the withdrawal of the stimulus and is not a late consequence of the application of the stimulus. The second wave is similar with respect to propagation speed and duration. The only difference is a slightly smaller overall intensity compared to the first wave.

Based on the plant's response to sodium chloride and its marked differences to the biotic stimuli it became clear to me that these wave is generated by a different mechanism. When the stimulation begins, the wave starts immediately and everywhere at the same time, the calcium concentration goes up and only seconds later it falls back to its previous level. The same process is repeated exactly at the moment when the stimulus is removed, only with a slightly weaker intensity. It is reasonable to assume that this wave is not a biological process at all but a physical reaction. That would imply that this is not a wave but a global reaction that takes place in the same way on all affected parts of the plant. Based on the experiments carried out by my collaboration partner I cannot ultimately prove or disprove that the observed response is a wave, in the sense that the calcium signal starts at a defined point of the plant and spreads from there to the other parts of the plant.

On the basis of personal communication with my collaboration partners, I understood that the analysis of our experimental data was not conclusive enough. Consequently, I approved the results of the literature claiming that the stimulation with sodium chloride triggers a very fast wave. That raised the question of how such a fast wave can be created biologically. I will deal with this question in Chapter 5.

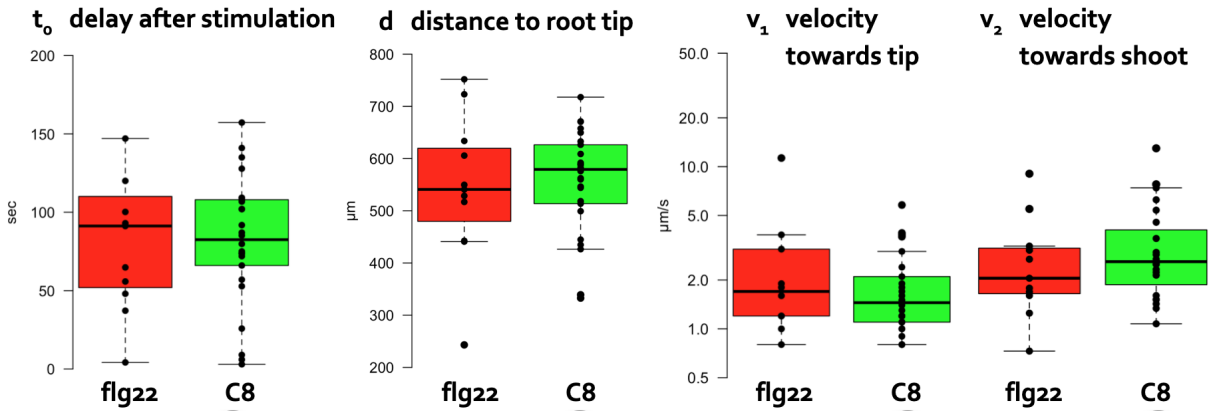

Figure 16. Wave characteristics of different stimuli: The results of the automated analysis of several stimulation experiments with flg22 (n = 9) and C8 (n = 19) were compared. On average, the characteristic parameters of the two different stimuli are similar: The delay after stimulation is between 50 seconds and 150 seconds for both stimuli. The starting point of the wave is around 550 µm for flg22 and approx. 600 µm for C8. The speed of the wave after stimulation with flg22 is around 2 µm/s, whereby the wave towards the tip is only slightly slower than the wave towards the shoot. For the stimulation with C8 the speed of the wave in the direction of the tip is around 1.5 µm/s and the speed in the direction of the shoot is around 3 µm/s.

4.5 Information theoretic analysis of the calcium wave

A basic idea that is always present in connection with calcium signaling is the ability of the calcium signal to transmit information. However, it is often not very clear how the information could be encoded. Should it be encoded in terms of amplitude, in terms of frequency, or in a mixture of both? A quite new way to quantify calcium signaling is the information-theoretic approach. Originally aimed at technical and electronic applications in the field of telecommunications it can also provide new insights into biochemical networks. Measuring the amount of information that is encoded in calcium fluctuations and that is transmitted to its target, can reveal emergent properties of the signaling pathway.

4.5.1 Transfer entropy

The information theory offers the so-called transfer entropy as a waveform-independent measure to determine the theoretically possible information content of a signal, which can be measured in bit, for example (Schreiber, 2000). By estimating conditioned transition probabilities it quantifies the information transfer from a dynamical system (e.g. calcium oscillations) to another system (e.g. enzyme activation). It considers the direction of the information transfer and the common history of both systems and is valid for linear and non-linear statistical dependencies. One challenge of applying a transfer information measurement is to estimate the probability distribution as close as possible to the real probability distribution which is generally not known. A further challenge is to deal with systems in which the current state depends on several previous states and therefore cannot be described by a Markov process of order one ("memorylessness"). The characteristics of a process in which the future depends only on the present but not on the past is termed the Markov property. In this study I only consider simple reaction systems that can be modeled as two dependent systems that satisfy the Markov property.

According to Schreiber (Schreiber, 2000) the transfer entropy $T_{J\to I}$ between two discrete processes I and J can be calculated from the conditioned transition probabilities of the single states i and j as

$$T_{J\to I} = \sum_{i_{n+1},i_n,j_n} p(i_{n+1}, i_n^{(k)}, j_n^{(l)}) log \frac{p(i_{n+1}|i_n^{(k)}, j_n^{(l)})}{p(i_{n+1}|i_n^{(k)})}. \tag{6}$$

The transfer entropy quantifies the deviation from independence by measuring the deviation from the Markov property of process I and has Kullback-Leibler divergence form. The Kullback-Leibler divergence indicates how much two probability distributions differ from one another, e.g. the probability distribution of the experimental data and the probability distribution estimated by using a model simulation. In the information-theoretical context, the Kullback-Leibler divergence quantifies the information capacity in bits that remains unused when coding data assuming a probability distribution Q, given the actually existing probability distribution P. For my study I only consider states which are dependent on the last previous state and are independent from all other previous states. On continuously-valued data the system holds the property of a Markov process of order one and k and l are set to 1.

4.5.2 Kernel density estimators

Because the real probability distribution of a system to be analyzed is usually not known, it must first be estimated. The easiest way to estimate a probability distribution is to create a histogram from the existing data. The disadvantage of the histogram as a density estimator is that a histogram is not continuous and can therefore only inadequately depict a continuous probability distribution. This issue is solved by using a kernel density estimator. A kernel density estimator is a uniformly consistent, continuous estimator of the probability density, which smooths the levels of the histogram by means of a kernel. Depending on the actual underlying probability, the shape of the kernel provides a more or less good estimate of the density. Common kernels are the rectangular kernel, the Gaussian kernel, and the Cauchy kernel.

4.5.3 Measuring the information content of the calcium wave

To quantify the information content of the calcium wave, I calculated the transfer entropy using a selected example of a data set of a stimulation with C8. An experimental kymograph and a kymograph from a simulation served as the data source for the transfer entropy calculation (Figure 17A, B). A cellular automaton was used to simulate the kymograph (a detailed description of the cellular automaton modeling can be found in Section 5.7). In a first step, the kymograph was binarized using a threshold value for the concentration of calcium. I applied the transfer entropy according to Schreiber to measure the dependence of the state of an information unit from the state of its neighbor (Schreiber, 2000). In this case one information unit corresponds to one pixel of the kymograph or one cell of the cellular automaton. Its state is represented by its concentration of intracellular calcium which increases and decreases as a result of the signaling process. In this case the signaling process is discretized by applying a threshold for the concentration. Then I calculated the transfer entropy of the binarized kymographs between the discrete signaling process J in one cell and the signaling process I in the neighbor cell from the conditioned transition probabilities of the single states i and j as described in Equation 6.

The results of the information-theoretic analysis of an exemplary kymograph of experimental data and a corresponding simulation with a cellular automaton revealed that the theoretical information that is contained in a small single unit was rather low with a value lower than 0.05 bit (Figure 17). A state in which you can choose between two equally probable decision-making options has the information content 1 bit. One must therefore assume that the calcium wave is hardly able to transport information at the level of individual information units such as the cell. The information about the stimulus becomes more clear when one analyzes the wave as a whole and evaluates global parameters, as was done in Section 4.4.

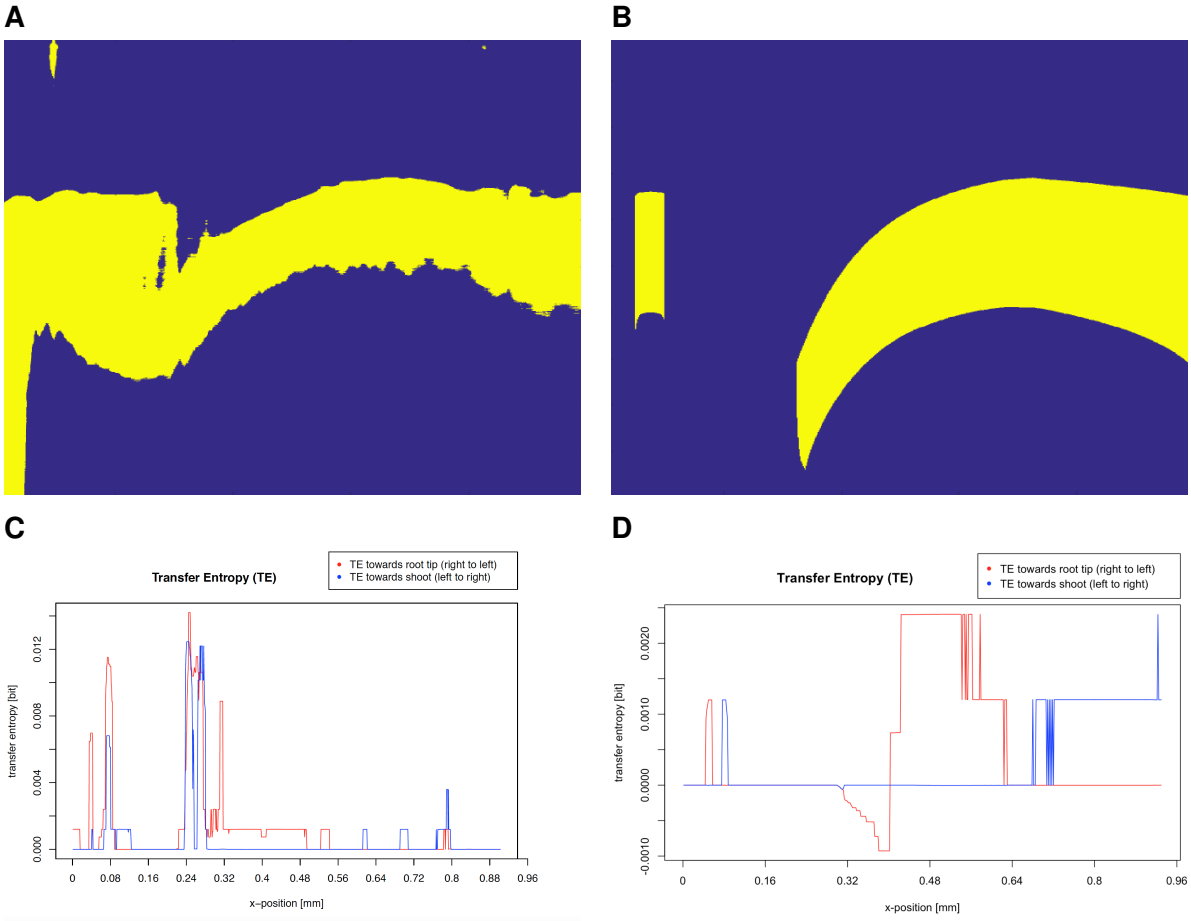

Figure 17. Binarized kymographs of a plant stimulation with the chitin polymer C8 based on experimental data (**A**) or a cellular automaton model (**B**) were used as input for a transfer entropy estimation (**C**, **D**). Root length depicted in the kymographs is 0.9 mm, total data acquisition/simulation time is 20 min. Before applying the information-theoretic algorithm the kymograph data were binarized using a threshold. The threshold was calculated as follows: Panel **A** (experimental data; for the original kymograph see Figure 15B): threshold = 0.5 × (maximum intensity – minimum intensity) + minimum intensity. Panel **B** (cellular automaton model): threshold = 0.2 × (maximum intensity – minimum intensity) + minimum intensity. To calculate the transfer entropy, the kymograph was considered as a matrix of binary pixels and split up into individual time series at each position along the axis of the root. A vertical column corresponds to a time series, i.e. the development of the calcium concentration at this position of the root over the examination time. The transfer entropy in the direction of the root tip shown in the graph is the vector of all individual values of the transfer entropy, that result from the information flow between process I at position x and process J at position $x-1$ according to the definition of the transfer entropy (see Equation 6). The transfer entropy in the direction of the shoot is the vector of all individual values of the transfer entropy which are derived from process I at position x and process J at position $x+1$. Transfer entropy was calculated by using a kernel density estimation algorithm with a rectangular kernel and a bandwidth of 0.2. Pixel position 0 is at the outermost tip of the root. In the simulation the signaling was triggered simulataneously at position 0.06 mm (root tip) and 0.70 mm (starting point of the primary wave).

5 Modeling of calcium signatures in plants

5.1 Chapter introduction

As I showed in the previous chapter, *Arabidopsis thaliana* plants react to high concentrations of salt or to attacks by bacteria or fungi with intracellular calcium signals. Just looking at the individual kymographs it became clear that the plant reacts differently to various stimuli. It is known from the literature that different stress factors trigger different reactions in the plant, especially at the level of gene expression through the activation of transcription factors. Abiotic stress such as salt stress mainly leads to the expression of genes that contribute to stress tolerance via the production of the plant hormone abscisic acid (Yamaguchi-Shinozaki and Shinozaki, 2006). In contrast, biotic stress tends to activate the hormones jasmonic acid, salicylic acid, and ethylene. However, it is also known that the signaling pathways of individual stress responses interact and that there is a crosstalk between them (Anderson et al., 2004; Atkinson and Urwin, 2012). It is tempting to assume that the type of stimulus is encoded into the wave, is passed on through the wave and can therefore trigger different reactions in the plant in the recipient organ. Actually, this question of the specificity of the calcium signal is very prominent in the scientific community in the field of calcium signaling (Scrase-Field and Knight, 2003; Dodd et al., 2010; Kudla et al., 2018). There is basically the possibility that other components also play a role here. Still, it is a popular hypothesis that the information about the stimulus is encoded in the temporal and spatial change of the intracellular calcium concentration as a so-called calcium signature (McAinsh and Pittman, 2009; Dolmetsch et al., 1998). Experimental evidence is still rare and there is also the opinion that the calcium signal is only an on-off alarm switch whose information content is only to put the cell in a state of defense (Scrase-Field and Knight, 2003; Plieth, 2005).

To test this hypothesis more closely, let's assume that calcium is the one and only carrier of stress response information. This requires that the individual plant cells are not only able to generate different calcium signals, but also to pass them on from cell to cell. The goal of my thesis was to find out more about how the plant can do this.

A prominent feature is the speed of propagation of the wave. From my evaluation of the experiments of my collaboration partners it was clear that the propagation speed of the wave with biotic stimuli is in the range of 5 µm/s. For stimulation with a high salt concentration, on the other hand, we expected a much higher speed. The image data from our stimulation experiments with salt allow two conclusions: either the stimulation with salt led to an impairment of our experimental system and thus to an unusable result or the wave rushes through the plant at such a high speed that our camera setup cannot detect. The literature supports the latter thesis: Choi et al. observed in their experiments that after stimulation with high salt concentrations, a wave runs through the plant at a speed of 400 µm/s (Choi et al., 2014). However, it is still unclear which molecular mechanism is behind such a speed.

In this chapter I want to shed a light on two questions: How can the plant generate different calcium waves and how can it pass the wave through its cells at such a high speed? I investigated these questions with the help of model simulations. For this I used various modeling techniques, on the one hand the computation of the wave propagation along a one-dimensional spatial axis based on the diffusion equation and on the other hand the simulation of the spread of calcium ions in two-dimensional space using a cellular automaton. I tried to reproduce individual aspects of the calcium wave in great detail and to create a model that

combines as many properties of the wave as possible.

It was challenging to model a wave that spreads over the cells at 400 µm/s. It is quite obvious that this high speed cannot be achieved with the diffusion of calcium alone. Evans et al. suggested that ROS could play a role in this and that the calcium wave is supported by a parallel ROS wave which together alternately trigger calcium and ROS channels. The decisive factor here is that, firstly, ROS have a higher diffusion speed and, secondly, the ROS wave runs in the intercellular space. This allows the ROS wave to easily overcome cell boundaries whereas the cell walls represent a large obstacle for the calcium wave or at least significantly slow down the propagation of the calcium wave.

By modeling calcium and ROS interactions in cooperation with the master's student Janos Löffler, who did a lot of the coding and testing, we were finally able to simulate these high speeds. In this way we could show that the combined propagation of calcium and ROS would be a feasible variant for calcium signaling. Using a cellular automaton, I was able to show how calcium spreads across cell boundaries and that the cell boundaries represent a significant obstacle to calcium signaling. With a simple model based on calcium-induced calcium release without the involvement of other components, I was able to reproduce the local wave that was observed with biotic stimuli measuring similar speeds as determined in the experimental data.

The diffusion was supported by a dense sequence of calcium channels, which pass the wave on from channel to channel and can keep it alive or even strengthen it. Another challenge was dealing with the different speed of the wave in both directions. With an extended model, which also simulates the different cell sizes of the cells within the different zones of the root, we were able to show that the speed of propagation correlates with the cell size, which in turn is based on the low calcium channel density in the transition between two cells. The smaller the cells, the slower the wave, the larger the cells, the faster the wave. The transition from cell to cell finally slows down the wave to such an extent that it comes to a halt and extends only a few millimeters around its starting point. It is therefore a locally limited wave that only affects a few cells in the immediate neighborhood. This model also coincides with the observation in our experiments that the local wave in response to biotic stimuli follows a non-linear course: at the starting point the speed of propagation is high and the speed increases with increasing distance. For the experiments with C8, which exhibit a very clear structure in the kymograph, the curve shape of the propagation can be described as approximately quadratic.

The results from the evaluation of different kymographs and crestline plots as well as the simulation results of the different models suggest that *Arabidopsis thaliana* plants can differentiate between different elicitors and react to them with different signaling. Basically, we are dealing with at least two different types of waves. Contact with bacteria or fungi leads, after a delay time of 2 to 3 minutes, to a locally limited slow wave emanating from a point in a relatively narrowly defined area near the root tip. This wave could put the tissue in alert to initiate appropriate measures. This could be a change in the direction of growth or protective measures against pathogens, for example.

Sensing high salt concentrations by the root, on the other hand, triggers an immediate signal response from the plant, which moves at a speed in the range of 400 µm/s towards the upper areas of the plant. The entire plant is alerted within a very short time and can react accordingly. The range of the wave can be interpreted as a criterion for which areas of the plant need to be alerted and which measures need to be initiated. While the local wave

can be considered more as a small correction task for the root, the global wave is able to put the entire plant on alert.

5.2 Outside assistance

Janos Löffler from the Grossmann Lab supported me in working on this chapter. As part of his master's thesis, Janos independently carried out stimulation experiments with *Arabidopsis* seedlings, the raw data of which he made available to me. Together with Janos, I first developed a model that reproduces the hypothesis of the combined ROS-calcium wave made by Evans in 2016. We then extended this model with the help of the parameters obtained from his experiments. The focus of Janos' work was on the acquisition of experimental data and the parameterization of the model, the focus of my work was on the programming of the source code for the model. Nevertheless, I would like to emphasize at this point that Janos has also worked his way into the depths of software programming with a lot of effort and has programmed large parts of the model himself and carried out and evaluated simulation runs.

5.3 Modeling intracellular calcium dynamics

When we speak of calcium dynamics, we refer to the change in the concentration of intracellular free calcium ions, which can take place in the millisecond range but also in the minute range and can develop forms such as oscillations, spikes and bursts. Intracellular calcium dynamics are determined by active and passive components: Active components are channels, Ca^{2+}/cation antiporters (CaCA) and pumps (P-type Ca^{2+} pump) proteins which control the release of calcium into the cytosol and its uptake as well as calcium buffering proteins (Geisler et al., 2000; Emery et al., 2012). They make it possible that a relatively low concentration of 100 nM prevails in the cytosol, while the concentration in the extracellular space and in the vacuole is around 100 times higher. The active elements in turn are coupled by diffusion of calcium ions. The diffusion characteristics of the receiving or storing compartment are the passive players in calcium dynamics. My goal was to create a computational model with which I could simulate the propagation of the wave through the plant and also measure the speed of propagation. Since initially only the longitudinal propagation along the vertical root-shoot axis played a role, I considered simulating the path of the wave from its starting point to the root tip or to the shoot as a one-dimensional propagation along a straight line. The wave was supposed to be passed on by means of calcium-induced calcium release through a combination of diffusion of calcium ions and calcium channels.

Evans et al. simulated this process in their seminal 2016 paper and came to the conclusion that a pure calcium wave cannot explain the observed speeds (Evans et al., 2016). They therefore postulated a mechanism in which the calcium wave is supported by ROS and thus achieves a higher speed of propagation. I wanted to use the model of Evans et al. as a basis and adapt it to the measurement data of my collaboration partners. In particular, I wanted to run simulations with this model in the area of the root tip (the lowest approx. 1.5 mm of the root), the area in which the image data of my collaboration partners were taken. In addition, I wanted to test the hypothesis whether the observed slow wave after biotic stimuli corresponds to a pure CICR-based calcium wave and the fast wave after stimulation with salt corresponds to the ROS-supported calcium wave. I accomplished this project together with

my cooperation partner Janos Löffler. Our goal was to create an expanded, more detailed version of the model by Evans et al., which takes different cell sizes into account and can also be parameterized for biotic and abiotic stimuli.

5.4 Simulating the calcium wave using a fire-diffuse-fire model

I started with a fire-diffuse-fire model that is based on pure calcium-induced calcium release (CICR), just like Evans et al. did (Evans et al., 2016). The term fire-diffuse-fire was first mentioned for the modelling of fertilization waves in *Xenopus* eggs and describes a model that consists of a number of point-shaped calcium sources that are embedded in a spatial continuum in which calcium ions diffuse (Dawson et al., 1999). My fire–diffuse–fire model can be split into three processes that are mutually dependent and alternate: the diffusion of calcium, the calcium-controlled opening of a calcium channel and the release of new calcium. I will now describe these processes in more detail in the following.

In general, spatial models of intracellular calcium dynamics are based on the following partial differential equation (PDE) which describes the diffusion of calcium within a compartment (Vaz Martins et al., 2013):

$$\frac{\partial c}{\partial t} = -F_{out}(c) + F_{in}(c) + D\nabla^2 c \tag{7}$$

The equation denotes the changes of the concentration c over the life time t based on a constant diffusion coefficient D. $F_{in}(c)$ and $F_{out}(c)$ describe the sum of fluxes of calcium ions into and from the compartment e.g. the cytosol.

For my purpose, I only wanted to investigate the expansion of the wave in the longitudinal direction, therefore I limited the simulation to one dimension. Furthermore I assumed, that there is no significant influx or outflux of calcium from or to the outside of our system. The diffusion equation for one dimension which describes the concentration $c(x,t)$ at a given position x and a time point t holds accordingly:

$$\frac{\partial c}{\partial t} = D\frac{\partial^2 c}{\partial x^2} \tag{8}$$

The theory of the diffusion equation was first described by Joseph Fourier to model the propagation of heat over a given area. That is why the diffusion equation is also referred to as heat equation or Fourier's equation. Diffusion describes the equilibrium of concentration differences of particles (atoms, molecules, ions) in a system over time. The cause of the equalization is the irregular and undirected movement of the particles due to their thermal energy, the so-called Brownian motion.

Solving the diffusion equation was challenging. As a first step, I aimed for a numerical solution using a finite-difference method. Finite-difference methods are a bunch of numerical methods for solving differential equations by a finite number of approximations. The spatial and temporal domain are discretized, the spatial range is sliced into a finite number of pieces and the temporal range is sliced into a finite number of time steps. At each step the value of the solution of the differential equation is approximated by the derivative at the discrete positions. For the model of calcium diffusion I used an implicit finite-difference method with homogeneous Dirichlet boundary conditions of zero. Homogeneous Dirichlet boundary conditions of zero means the concentration at both ends of the spatial line is always zero.

In the next step, I redesigned the model and replaced the numerical method by a calculation based on the fundamental solution. For every linear partial differential operator with constant coefficients there is a so-called fundamental solution. The fundamental solution for the one-dimensional diffusion equation reads:

$$H(x,t) = \frac{1}{(4\pi Dt)^{\frac{3}{2}}} e^{-\frac{x^2}{4Dt}} \tag{9}$$

$H(x,t)$ denotes the so-called heat kernel and D the diffusion coefficient of the diffusing substance. If the initial concentration $c_0(x)$ at time point zero is represented as a Dirac delta function, then the concentration $c(x,t)$ at location x and time t is calculated by convolution of the heat kernel H with the initial concentration $c_0(x)$:

$$c(x,t) = (H * c_0)(x,t) \tag{10}$$

The Dirac delta function, also called the unit impulse function, is defined in such a way that the function value is zero for all $x \neq 0$ and infinity for $x = 0$. The integral of the Dirac delta function over all x is 1. If one thinks of the opening process of an ion channel as an instant point-shaped particle release of strength n_0, which can be mathematically described as a Dirac delta function with an integral of size n_0, then the concentration $c(x,t)$ can be calculated as follows:

$$c(x,t) = \frac{n_0}{(4\pi Dt)^{\frac{3}{2}}} e^{-\frac{x^2}{4Dt}} \tag{11}$$

The total concentration at a position x at time t can be calculated by summing up the release concentrations of all channels that had already emitted calcium at this point in time. To do this, in the above formula, t must be replaced by $(t - t_i)$ and x by $(x - x_i)$ for every single channel, where t_i represents the opening time and x_i represents the position of the respective channel. From the perspective of code performance, the calculation of the concentration becomes more and more time consuming, the more channels have already been open.

Table 2: Determination of the diffusion coefficient of calcium in the literature. Most of the lab experiments and simulations were performed using eggs of frogs (mainly *Xenopus laevis*) or ascidians.

publication	diffusion coefficient	condition / application
Cheer et al. (1987)	10 µm²/s	modeling of calcium waves
Falcke et al. (1999), Falcke (2004)	20 µm²/s	modeling of calcium waves
Kroeger et al. (2008)	20 µm²/s	simulation of pollen tubes
Straube and Ridgway (2009)	20 µm²/s	simulation of calcium buffering
Evans et al. (2016)	20 µm²/s	modeling of calcium waves
Bugrim et al. (2003)	40 µm²/s	modeling of calcium waves
Dupont and Dumollard (2004)	40 µm²/s	modeling of calcium waves
Allbritton et al. (1992)	13 µm²/s to 65 µm²/s	for 90 nM to 1 µM calcium
Allbritton et al. (1992)	up to 220 µm²/s	for $\gg$ 1 µM calcium

To model the diffusion of free calcium ions, the diffusion coefficient of calcium in the cytosol is required. Various values appear in the literature (Table 2). Most values are in the range

between 10 µm^2/s and 65 µm^2/s. Albritton et al. demonstrated the dependence of the diffusion coefficient from the amount of free calcium and showed that the diffusion coefficient could even be increased to around 220 µm^2/s if enough calcium is added (Allbritton et al., 1992). However, at physiological concentrations the diffusion of calcium is inhibited by binding to immobile or slowly moving buffers, whose diffusion coefficient also determines the diffusion coefficient of calcium (Allbritton et al., 1992). The diffusion coefficient of these mobile calcium buffers is about ten times smaller than the diffusion coefficient of free calcium (Zhou and Neher, 1993; Burrone, Juan et al., 2002). In his 2004 review, Martin Falcke names a value of 20 µm^2/s for cytosolic calcium based on his modeling of calcium waves in frog eggs published in 1999, which Kröger et al. used in his simulation of the growth of pollen tubes (Falcke et al., 1999; Falcke, 2004; Kroeger et al., 2008). Simulations showing the diffusion of calcium taking into account stationary calcium buffer proteins and assuming 30 % molecular crowding also result in a value of approx. 20 µm^2/s (Straube and Ridgway, 2009). Following Evans et al., we decided to use a diffusion coefficient for calcium of 20 µm^2/s as well (Evans et al., 2016).

A prominent active player in plant calcium dynamics is the voltage and calcium-dependent two pore channel 1 (TPC1), which is located on the membrane of the vacuole and might allow calcium to flow from the vacuole into the cytosol when it is opened. This channel was described first as a slow vacuolar (SV) channel in the mid eighties (Hedrich et al., 1986; Hedrich and Neher, 1987). Although much is still unclear, this channel has been studied quite well by the scientific community (Hedrich and Marten, 2011; Hedrich et al., 2018). The researchers agree that the opening mechanism of TPC1 on the cytosolic side requires depolarization and activation by calcium binding. It is also undoubted that potassium ions flow from the vacuole into the cytosol through the open channel. However, it is still under debate whether calcium ions actually flow from the vacuole into the cytosol.

At current opinion the gating mechanism of TPC1 controlled by cytosolic calcium is as follows: Voltage-dependent opening via depolarization and cytosolic calcium work together in a synergistic manner. The resting electrical potential at the vacuolar membrane of -30 mV and the high concentration in the vacuole of about 10 mM calcium stabilizes the voltage-sensing domain of TPC1. An initial depolarization of the vacuolar membrane potential prepares the channel for opening: the voltage-sensing domains of the channel will be positively charged, unlock and slightly move towards the volume of the vacuole. The channel is now primed for opening but still closed. If cytosolic calcium increases the binding of calcium ions to TPC1 leads to a conformational change of the protein thereby dilating the pore and opening the passage.

As mentioned above, it is not entirely clear whether TPC1 really allows calcium ions to flow through. TPC1 has a binding site for calcium both on the cytosolic domain - which is used to activate the channel - and on the vacuolar domain which, in combination with the membrane potential, stabilizes the closed state. It is therefore difficult to experimentally investigate whether the channel lets calcium ions through. Experiments with *Arabidopsis* TPC1 channels expressed in the plasma membrane of HEK293 cells, in which the vacuolar domain was less calcium-sensitive due to genetic modification, lead to the conclusion that TPC1 actually is open for calcium ions in vivo (Guo et al., 2016; Schönknecht, 2013). On the other hand, Ranf et al. found no change in calcium signaling in plants in which the TPC1 channel was missing (Ranf et al., 2008). Choi et al. again see a change in the speed of propagation depending on the presence of TPC1, in its TPC1 knockout variant the calcium waves were still present in reponse to salt stress, but their speed of propagation was reduced

by 25 times (Choi et al., 2014). Overexpression, however, increased the propagation speed (Choi et al., 2014). The final experimental proof of the role of TPC1 as a decisive calcium channel in calcium-induced calcium release is still pending. It should also be mentioned at this point that TPC1 is a slow channel. The original experiments by Hedrich et al., who measured the activation behavior of the channel via the electrical current, show that the time it takes for the channel to be fully activated is in the order of seconds (Hedrich and Neher, 1987). This is not particularly helpful for creating a fast calcium wave. Hedrich et al. (2018) came to the conclusion in his review that it is very likely that TPC1 does not trigger a calcium wave in response to stress, but is involved in fine-tuning the signal propagation.

My model might help to shed light on this question. To do this, I first designed a model using TPC1 as a calcium-controlled calcium channel the opening of which is initiated by the fact that the calcium concentration at its position exceeds a fixed threshold value. The simplest way to simulate a wave with calcium-induced calcium release is a one-dimensional model based on pure diffusion, in combination with point-shaped calcium channels that are evenly distributed over the path. For my simulation I chose a total length of the root of 2000 µm and simulated over a period of 2 seconds (see Table 3 for a complete list of the model parameters). In order to keep the computing time within reasonable limits, I chose a spatial resolution of 0.2 µm and a temporal resolution of 1 ms (for modeling the slow local wave time was simulated over a period of 2 minutes with a resolution of 0.1 seconds).

Table 3: Modeling parameters for simulating a calcium wave based on calcium-induced calcium release using the vacuolar channel TPC1.

parameter	value slow wave model	value fast wave model
simulation time	120 s	2 s
temporal resolution	0.1 s	0.001 s
root length	2000 µm	2000 µm
spatial resolution	0.2 µm	0.2 µm

The TPC1 channel was modeled as a point-like calcium source on the root-shoot axis. If the calcium concentration at this point exceeds the value of 0.35 arbitrary units (a.u.) above resting concentration, the channel opens and releases calcium. I combined the opening, the outflow of calcium for a certain time and the closing of the channel in a single process, which instantaneously releases a fixed amount of calcium ions. After release the channel is inactive for the remaining time of the simulation mimicking the refractory period of the ion channel. Since there are no experimental data on the number of released calcium ions per opening process and it is not yet clear whether in vivo calcium ions are released at all, I had to define this value. I knew from the literature that the concentration near the vacuolar membrane can increase up to 1.5 µM when the plant is stimulated with mannitol or salt (Knight et al., 1997). I could therefore consider this release as a one-dimensional calcium microdomain of a very small width, i.e. I added a certain concentration of calcium to the existing concentration in a small area around the channel. From a mathematical point of view, the release of calcium ions was modeled as a point source of width 0, height ∞ and area 1 using the Dirac delta function, which for convenience I named a channel with the 'release strength' 1 a.u. of calcium.

I would like to point out that I simulated the calcium release of the channel as an instantaneous process, although the channel is a slow channel and the release of calcium may take a

considerable time. However, since I first wanted to use the model to check whether the high speeds described in the literature can be achieved by means of pure calcium-induced calcium release, I initially assumed the highest possible speed for calcium release. When analyzing the simulation results, I keep that in mind.

In addition to the calcium release of a TPC1 channel, another parameter plays an important role for the CICR model: the distance from channel to channel and thus the distribution of the channels over the root. It is clear that the speed of propagation of the wave is very much related to the channel spacing: the greater the distance, the slower the wave runs. I wanted to integrate a simple but realistic positioning of the channels in my model. I therefore placed the channels along the one-dimensional spatial axis in such a way that their distribution in the model can be parameterized with two values: one is the channel distance d_v between two channels within the vacuolar membrane and the other is the channel distance d_z between two cells, i.e. the distance between the last channel on the vacuole of one cell and the first channel on the other cell. The sequence of the distances in the model is d_v, d_v ... d_v, d_z, d_v, d_v ... d_v, d_z, d_v ... To gain a maximum of wave speed I assumed that calcium can diffuse in both directions without restrictions and cell walls or plasmodesmata do not hinder the spread. The only braking effect of the cell wall is due to d_z being larger than d_v.

Together with my cooperation partner Janos Löffler, I parameterized the model according to various conditions and performed simulation runs. For setting the parameters we stuck to the paper by Evans et al. and chose $d_v = 1$ µm and $d_z = 3$ µm to 4 µm (Evans et al., 2016). The exact value of d_z depends on the cell size (see below). Just like Evans et al. we also created an alternative model that simulates a *Arabidopsis* mutant in which the TPC1 channel is overexpressed. This model has exactly the same parameters as the main model, only d_v is set to 0.6 µm here. How often the distance d_v occurs in a row depends on the length of the cell in the axial direction. Especially in the root, the cells have very different sizes depending on the zone where the processes of cell division and growth take place. Figure 18 shows a diagram of the different sizes in the root tip. In order to get a smoother transition from the minimum cell size in the root tip to the maximum cell size in the differentiation zone we implemented the cell size as a function of the distance x from the root tip using a characteristic sigmoid-shaped function, the logistic function:

$$f(x) = \frac{L}{1 + e^{-k(x-x_0)}} \tag{12}$$

k represents the steepness and x_0 the midpoint and turning point of the sigmoid curve. In relation to the cell size, L_0 can be described as the minimum cell size $L_{\min}$ and $L_0 + L$ as the maximum possible cell size $L_{\max}$ with L being the difference between the maximum and minimum cell size. We defined the turning point x_0 as the ratio between the minimum and maximum cell size. We determined k using a factor c with respect to the maximum cell size: $k = c * (L_0 + L)$. The formula for calculating the cell size holds now:

$$f(x) = \frac{L_{\max}}{1 + e^{-c \cdot L_{\max} \cdot x}(\frac{L_{\max}}{L_{\min}} - 1)} \tag{13}$$

The parameters for the minimum and maximum cell size and the factor c are estimated from the publication by Lucas and Shaw, who experimentally determined the cell size in *Arabidopsis* roots (Lucas and Shaw, 2012). We set the parameters as follows: $L_{\min} = 5$ µm, $L_{\max} = 130$ µm, $c = 0.00008$.

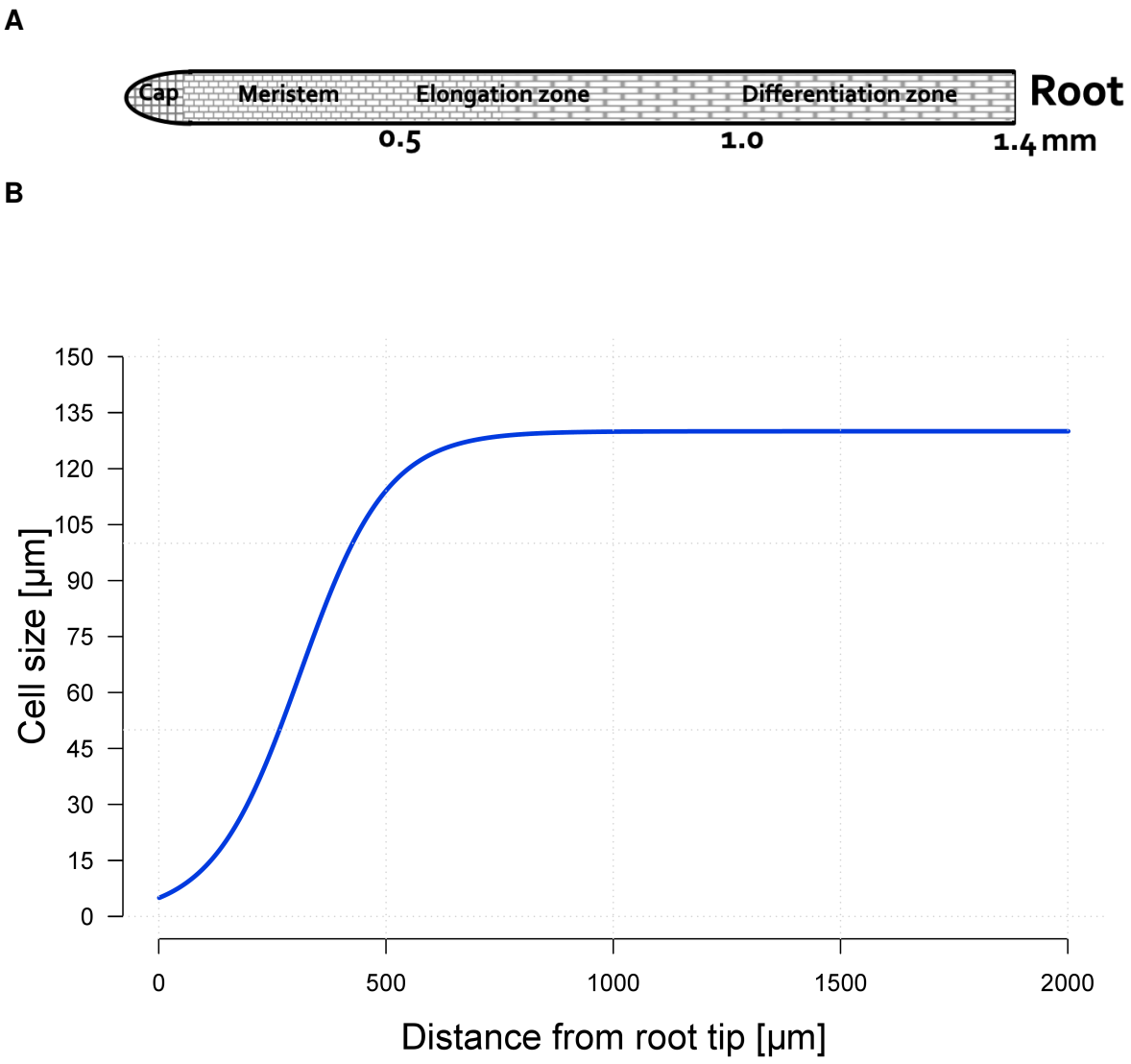

Figure 18. Cell size in root tip is different depending on the growth zone (**A**) cell size can be estimated applying a logistic function (**B**).

From our stimulation experiments we knew that the calcium wave in response to biotic stimuli starts in a very narrow zone about 0.5 mm from the root tip (Figure 16). We simulated the starting event by triggering the calcium release of a couple of TPC1 channels around a specific position. These channels then automatically launched the calcium wave by means of CICR. It should be mentioned that triggering a single channel might not be enough to start a wave, but that the triggering stimulus must have a certain strength. For practical reasons, we chose the start stimulation for our simulation by opening 10 channels simultaneously. We ran several simulations with different starting positions. We chose 0.25 mm, 0.5 mm and 1 mm distance from the root tip as representative starting positions. Thanks to the model structure, we could precisely calculate the speed of propagation at each position of the wave by measuring the time point at which the channel is triggered at that position. Using these values we could also graphically display the simulation as a kymograph (Figure 19).

We calculated the mean speed of the wave in both directions over a simulation period of 2 minutes at different starting positions (Table 4). Since the cell size and thus also the size

of the vacuole increases in the direction of the shoot and thus the wave can travel a larger and larger distance on the "highway" of the vacuole, it is inevitable that the speed in the direction of the shoot is greater than that in the direction of the root tip. The increasing cell size in the direction of the shoot also means that the speeds increase as the distance between the starting point and the root tip increases. The propagation speed measured by Choi et al. in the direction of the shoot of about 400 µm/s in response to the stimulation with salt can only be achieved if the starting point of the wave is shifted to 1 mm so that the cells all have their maximum size (Choi et al., 2014). In the stimulation experiments with high concentrations of salt (see Figure 15D for an example), the starting point of the wave could not be determined due to the time resolution of the camera. It actually may be at a position of 1 mm or larger in the direction of the shoot. This would justify our assumption to use a starting point of 1 mm distance to the root tip.

While the simulation of the wild type could achieve the described speed of 400 µm/s, the overexpression mutant only reaches around 526 µm/s instead of 700 µm/s described by Choi et al. For this variant, all parameters were set with respect to the highest possible speed: the calcium release of the TPC1 channels happens instantaneously, the channel-to-channel distance is very small at 0.6 µm, cell walls and plasmodesmata are ignored and a maximum cell size is assumed. Finally, with our extended model, which includes different cell sizes, we came to the same conclusion as Evans et al. that a wave based on pure CICR cannot be the source of the calcium wave as a response to stimulation with salt, but that further effects must be involved (Evans et al., 2016).

If we compare the results of the CICR simulation with the speeds determined in our experiments as a reaction to biotic stimuli, then these are again far above our experimental measurement data of approx. 5 µm/s (Figure 16). We therefore considered reducing the speed in our model by reducing the diffusion coefficient of calcium. Test runs with different values showed that with a diffusion coefficient of 1 $\mu m^2/s$ instead of 20 $\mu m^2/s$, we can reach the expected speed ranges. In the cytosol, calcium ions might not diffuse so slowly, but perhaps the transition from cell to cell through the plasmodesmata does not work as smoothly and quickly as expected. In consequence, I extended the model implementing diffusion through plasmodesmata (see section 5.6).

5.5 Combined calcium and ROS wave

A model based purely on calcium-induced calcium release cannot explain the propagation speeds observed in the experiment. Also, clustering of the calcium channel or cytoplasmic streaming cannot explain the observed velocities. Therefore, Evans et al. suggested that reactive oxygen species (ROS) should also be taken into account when modeling the calcium wave (Evans et al., 2016). They performed various experiments in which the production of ROS was suppressed and found that the speed of propagation of the wave became considerably lower. Among other things, they treated plant roots with ROS killers and inhibitors that inhibit the protein responsible for the production of ROS in the plasma membrane, the NADPH oxidase RBOHD. They also carried out experiments with an RBOHD knockout mutant. This mutant exhibited a decreased propagation speed of the calcium wave. In further experiments they found that the spread of ROS depends on both RBOHD and the ion channel TPC1. The activation of RBOHD in turn depends on cytosolic calcium (Ogasawara et al., 2008). Evans et al. came to the conclusion that the systemic stress response

in the *Arabidopsis* root is accompanied by a ROS-assisted calcium-induced calcium release, which is generated with the help of the NADPH oxidase RBOHD and the cation channel TPC1. They incorporated the ROS support into their extended model and thus were able to quantitatively reproduce the observed speeds of the calcium wave.

The idea of the ROS-assisted CICR is based on the following mechanism: intracellular calcium activates RBOHD in the plasma membrane. RBOHD produces extracellular ROS. The extracellular ROS activates ROS-sensitive calcium channels in the plasma membrane, causing calcium to flux from the extracellular matrix into the cytosol. In turn, the increased calcium concentration triggers the TPC1 channels in the vacuole, further calcium is released, the released calcium activates RBOHD in the plasma membrane. The key point here is that the intracellular calcium wave is accompanied by an extracellular ROS wave, which has a much higher speed and can overcome the cell boundaries in the extracellular space without any obstacles. The diffusion coefficient of ROS is roughly $1 \cdot 10^{-9}$ m^2/s = 1000 µm^2/s (Bhattacharjee, 2012). This diffusion coefficient is an estimate from the value of $1.7 \cdot 10^{-9}$ m^2/s ($1.93 \cdot 10^{-9}$ m^2/s for oxygen, $1.43 \cdot 10^{-9}$ m^2/s for hydrogen peroxide) , which was measured in an aqueous buffer solution, but one can assume that due to molecular crowding, similar to the diffusion of calcium ions, the diffusion decreases by 20% - 50%. (van Stroe-Biezen et al., 1993; Straube and Ridgway, 2009). A value of 1000 µm^2/s is also used in other publications modeling ROS-mediated signals (Vestergaard et al., 2012).

We expanded our model in order to support ROS-assistance. For this purpose we added a level of extracellular ROS diffusion to the calcium diffusion, which propagates along the same spatial axis. In the plasma membrane there are point-shaped ROS-sensitive calcium channels at regular intervals of 1 µm, which release calcium from the extracellular matrix into the cytosol when a certain ROS concentration is reached. At the previous calcium diffusion line, there is also the NADPH oxidase RBOHD, which, for the sake of simplicity, is also modeled as a point source. Similar to an ion channel, RBOHD instantly produces a certain amount of ROS when a specified calcium threshold is exceeded (Ogasawara et al., 2008; Chen and Yang, 2020). In the following we will therefore refer to our RBOHD model as a "channel" that "releases" ROS, even if it is physiologically an enzymatic process.

We assumed an identical spatial position for the plasma membrane and the vacuolar membrane in our model, which means that the spatial axis of the ROS wave coincides with the spatial axis of the calcium wave. The physiological calcium concentration in the extracellular matrix and in the vacuole is also similarly high at around 10 mM. The increase in intracellular calcium is now additionaly achieved by calcium triggering ROS-sensitive channels parallel to the TPC1 channels, which release calcium into the cytosol via extracellular ROS diffusion. Due to the higher diffusion speed of ROS, the propagation speed of the wave is now determined by ROS, only slowed down by the ROS-calcium-ROS exchange. In our type of simulation along a one-dimensional spatial axis, all channels are located on this axis. The relative position of all three channel types to one another is therefore decisive for the propagation speed of the wave, as is the respective trigger threshold value for calcium or ROS. If RBOHD is closer to the ROS-sensitive calcium channel and/or is more sensitive to calcium than TPC1, a simulation scenario is possible in which the ROS wave also runs without the presence of TPC1 and the vacuolar ion channel has no effect on the speed of propagation.

In our model, however, TPC1 should have a significant effect on the calcium wave, whereas ROS should serve as an amplifier of the TPC1-controlled calcium wave. Therefore, we decided on a different scenario in which the spatial distance between RBOHD and the ROS-

sensitive calcium channel is so large that the calcium release by TPC1 is essential for the propagation of the ROS wave.

The density of the RBOHD proteins in the plasma membrane is higher than the density of the TPC1 channels in the vacuolar membrane (Peiter et al., 2005; Hao et al., 2014). We parameterized the distance between two adjacent RBOHDs in our model with 0.2 µm. The distance between two ROS-sensitive calcium channels in the plasma mebrane is assumed to be the same as the TPC1 channel distance im *Arabidopsis* wild type, namely 1 µm. The amount of released calcium ions or ROS molecules, the so-called 'release strength', was set to 1 arbitrary unit of calcium for all three channels. The threshold values of the calcium-sensitive protein RBOHD was chosen to be 180 a.u. of calcium, a value quite higher than the threshold of the TPC1 channel to ensure that ROS assistance is only activated at a high level of calcium. The threshold for the ROS-sensitive calcium channel was set to 270 a.u. of ROS. Compared to the original model without ROS assistance, all existing parameters were retained. The starting point was also chosen at 1000 µm distance from the tip, since the cell size is definitely maximum here and the wave can run at maximum speed in the direction of the shoot.

The simulation runs of the extended model show the following result: in the wild type, the observed speed of 370.4 µm/s is slightly slower than in the pure CICR model. This is due to the fact that at the same time as the introduction of ROS support and calcium release from the extracellular matrix, the vacuolar calcium release was reduced. Nevertheless, the results fit well with the 400 µm/s described in the literature. When simulating the TPC1 overexpression scenario with a channel spacing of 0.6 µm, the wave reaches a speed of around 700 µm/s in direction to the shoot (Figure 19D), which is similar to the speed described by Choi et al. (Choi et al., 2014). It is interesting here that the decreasing cell size in the direction of the root tip has only a small influence on the speed, i.e. the support from extracellular ROS can help to overcome the braking effect of the cell-to-cell transitions in the calcium wave. With the help of our model adapted to the different cell sizes, we can conclude along with Evans et al. that a ROS-supported calcium wave is a possible explanation for the observed speeds of the calcium wave in response to salt stimulation.

Table 4: Averaged propagation speed of the calcium wave in the pure CICR-based model.

cell type	starting position [µm]	velocity rootward [µm/s]	velocity shootward [µm/s]
wild type	0.25	218.2	423.5
TPC1 overexpressor	0.25	236.1	502.2
wild type	0.5	280.6	440.5
TPC1 overexpressor	0.5	310.6	523.1
wild type	1	415.0	440.5
TPC1 overexpressor	1	455.8	526.1

Averaged velocity was calculated with respect to the propagated distance within 2 minutes after start of the wave.

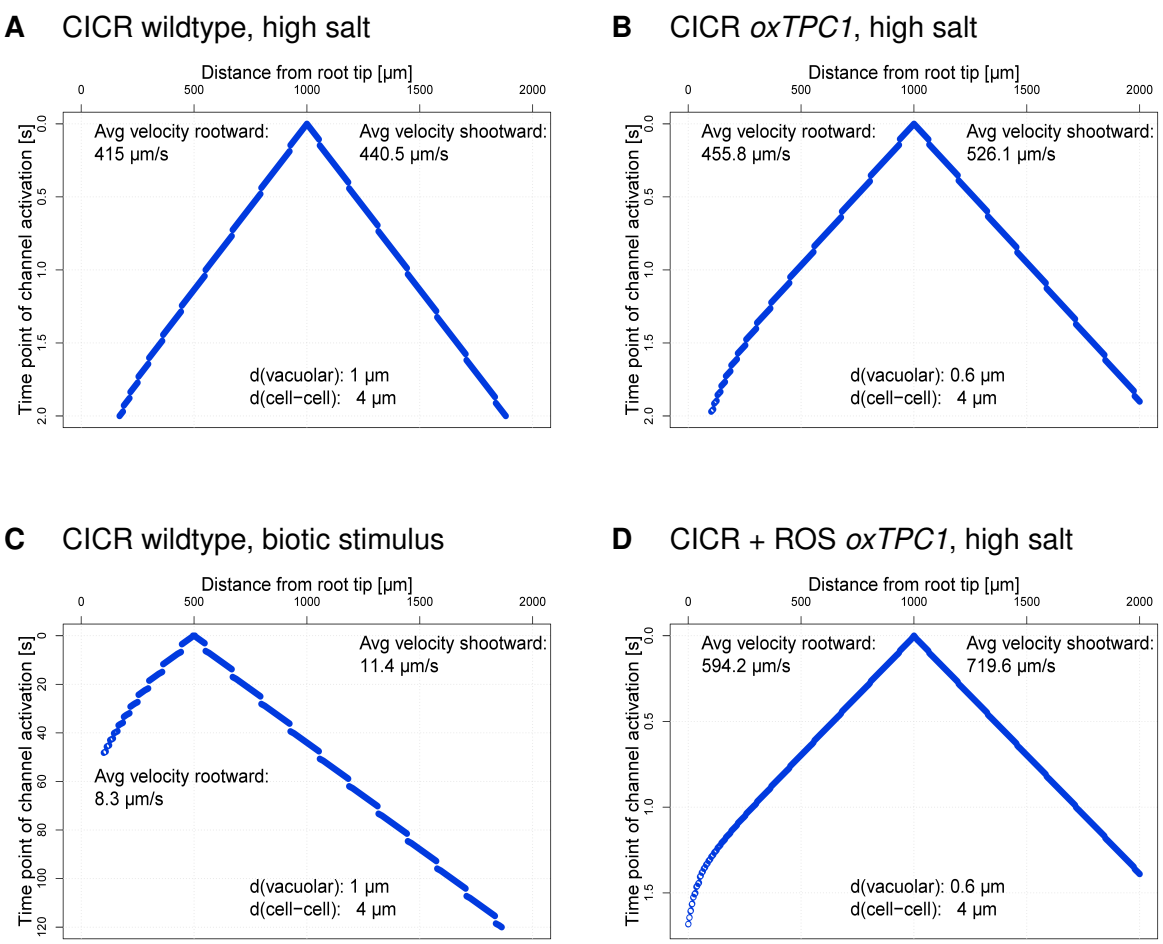

Figure 19. Kymographs based on a fire-diffuse-fire model of the calcium-induced calcium release (CICR) under different conditions. The simulation results were displayed by plotting the opening time points of the individual TPC1 channels as dots in the space-time diagram. The gaps in the curve mark the cell-cell connections by plasmodesmata in which there are no TPC1 channels. The simulation was started by controlled opening of one channel at a defined position 1000 µm from the root tip (biotic stimulus: simultaneous opening of 10 adjacent channels at position 500 µm from the root tip) **(A)** Simulation of a calcium wave based on pure CICR after stimulation with high salt of the *Arabidopsis* wild type; Simulation parameters: distance between adjacent channels: dTPC1(vacuolar) = 1 µm, dTPC1(cell-to-cell) = 4 µm; calcium concentration threshold for opening: thresTPC1 = 0.35 a.u. **(B)** Simulation of a calcium wave based on pure CICR after stimulation with high salt in the *Arabidopsis*-TPC1-Overexpressor *oxTPC1*; Simulation parameters: dTPC1(vacuolar) = 0.6 µm, dTPC1(cell-to-cell) = 4 µm, thresTPC1 = 0.35 a.u. **(C)** Simulation of a calcium wave based on pure CICR after stimulation with a biotic stimulus in the *Arabidopsis*-TPC1-overexpressor *oxTPC1*; Simulation parameters: dTPC1(vacuolar) = 1 µm, dTPC1(cell-to-cell) = 4 µm, thresTPC1 = 55 a.u. **(D)** Simulation of a calcium wave based on ROS-assisted CICR after stimulation with high salt in the *Arabidopsis*-TPC1-overexpressor *oxTPC1*; Simulation parameters: dTPC1(vacuolar) = 0.6 µm, dTPC1(cell-to-cell) = 4 µm, thresTPC1 = 0.35 a.u., thresRBOHD = 180 a.u., thresROSsensitiveCaChannel = 270 a.u. Explanation of the parameters: dTPC1(vacuolar) = channel-to-channel distance between adjacent TPC1 channels on the vacuolar membrane, dTPC1(cell-to-cell) = channel-to-channel distance between the last TPC1 channel of one cell and the first TPC1 channel of the next cell, thresTPC1 = threshold value for the concentration of intracellular calcium that must be exceeded for the channel to open.

5.6 Simulating calcium dynamics using a cellular automaton

It turned out that the modeling of a calcium wave based on a one-dimensional diffusion equation does not cover all aspects of calcium signaling. It was difficult to choose the correct value for the diffusion coefficient, since the unhindered diffusion of calcium in the cell is slowed down by buffer proteins and molecular crowding. Since it can be assumed that these obstacles occur evenly throughout the cytosol, it was justified to simply include them as a factor in the diffusion coefficient. However, the situation is different with the diffusion from cell to cell through the plasmodesmata. Plasmodesmata are narrow tubes approx. 50-60 nm in diameter and 300-400 nm in length, which connect the cytosol of a cell with the cytosol of its neighboring cells (Sager and Lee, 2018). More precisely, a Plasmodesma is a tube with a tube running through it, since the ER runs through the plasmodesma as another tube. The density of the plasmodesmata is about 1 - 10 per μm^2. It is also known that the cell can regulate the opening width of the plasmodesmata (Sun et al., 2019). Plasmodesmata therefore represent a sieve-like bottleneck for the diffusion of calcium ions and it cannot be assumed that the diffusion through the plasmodesmata takes place at the same speed as in the open cytosol.

At first, I had no idea how particles behave in such a narrow point. Was the influence really negligible? I wanted to clearly visualize the situation in the plasmodesmata. My aim was to simulate the diffusion in a way in which different spatial constellations can be modeled quickly and easily and which can also be represented graphically very well. So the idea of using a cellular automaton came up. One of the strengths of the cellular automaton is that it can show emergent behavior, i.e. complex patterns can emerge on the basis of simple rules. Furthermore, a simulation with a cellular automaton can provide the basis for a follow-up mathematical model based on differential equations.

So I designed a cellular automaton based on a stochastic set of rules to simulate diffusion, which I will describe in more detail in the following. I used the same principle in a further step in an abstract form to simulate the entire calcium wave (see Section 5.7).

For simulating the movement of individual particles based on a stochastic cellular automaton I applied a parallel random walk of a certain number of particles in a cellular grid. The release of calcium through a channel was modelled by 5000 particles which do a random walk of a certain number of steps. Each particle starts its walk at the same position at the assumed center of the channel. In each step the particle can randomly move to one of its eight neighboring cells (Moore-neighborhood). Following the assumption that particles in a liquid medium are subject to Brownian motion, the particle must always be in motion here too. The particle has to move, its not allowed to stay in the same cell, however it might move back to its original cell in the next but one step. Figure 20 shows an example of a random-walk based calcium release from a point-shape channel using 5000 particles after 100 steps per particle.

In the next step, I placed barriers in the simulation grid next to the channels, each of which only had two small gaps with a width of 4 cells. The barriers should symbolize the cell walls and plasmodesmata. During the simulation, it turned out that the cell walls were a very large obstacle. After 100 development steps, only a few particles made it into the neighboring cell (Figure 21A). After 300 development steps the number of particles that had moved into the neighboring cell was still very low at 20 out of 5000 (Figure 21B). Judging by the simulation, cell walls and plasmodesmata do represent a major obstacle to the calcium wave.

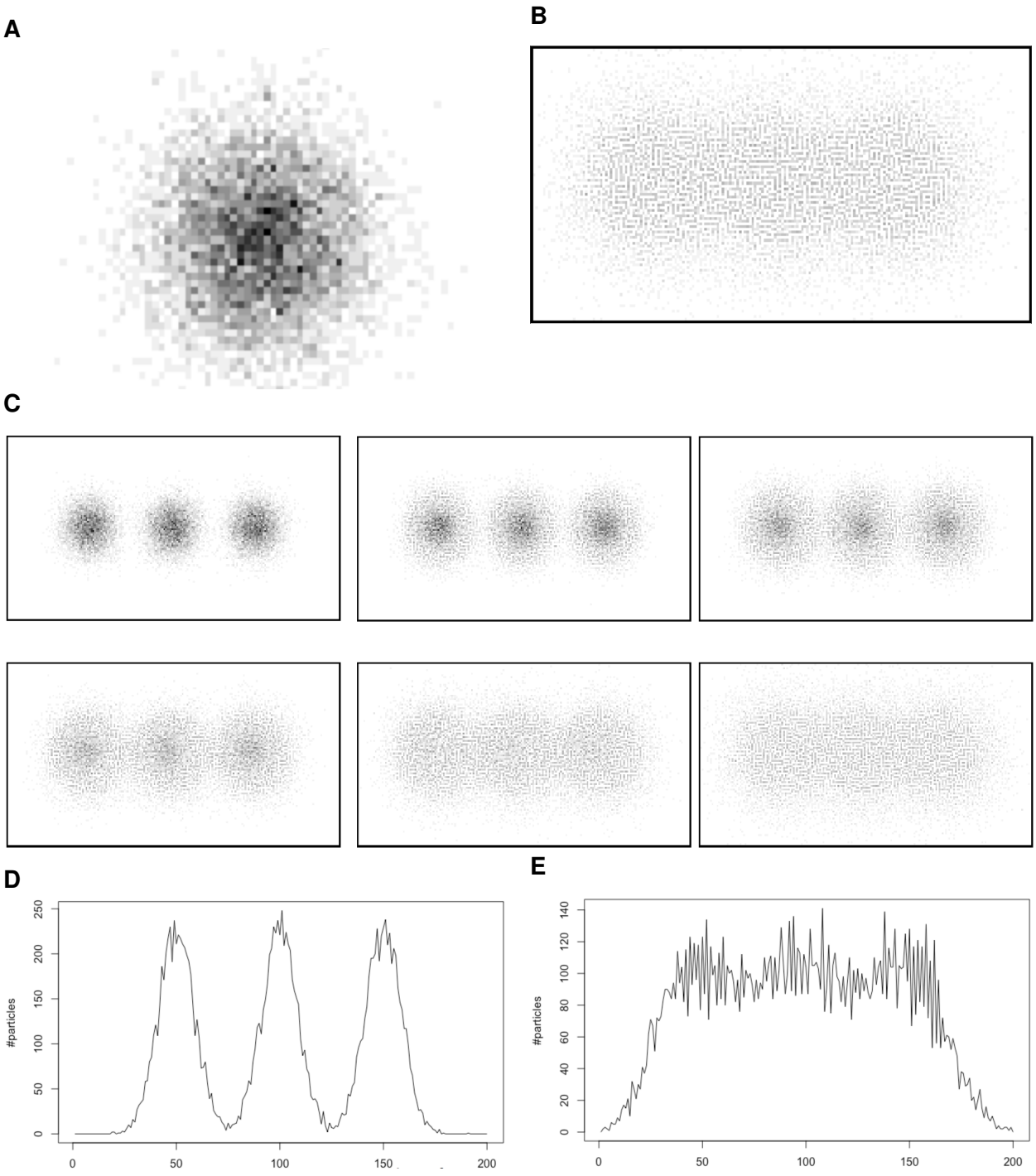

Figure 20. Simulation of calcium diffusion after release of a channel as a randow walk of single ions: random walk of 5000 particles all starting in parallel from the center position. Panel **A** shows a state after 100 steps per particle, in each step each particle can randomly move to one of its eight neighboring cells. After a long simulation time, the particles are distributed evenly in the simulation space (**B**). In a simulation three channels were triggered opening in parallel thereby releasing 5000 particles each (**C**). The panels show the diffusion after 100, 200, 300, 400, 500 and 600 time steps (left to right). After 600 time steps all particles are almost equally distributed all over the grid. The color code represents the number of particles per cell (cell here means the spatial unit of the cellular automaton, not a cell in the biological sense): white = 0 particles/cell, black = 250 particles/cell. Panel **D** and **E** show the particle concentration along the x-axis 100 time steps after release (**D**) and 500 time steps after release (**E**).

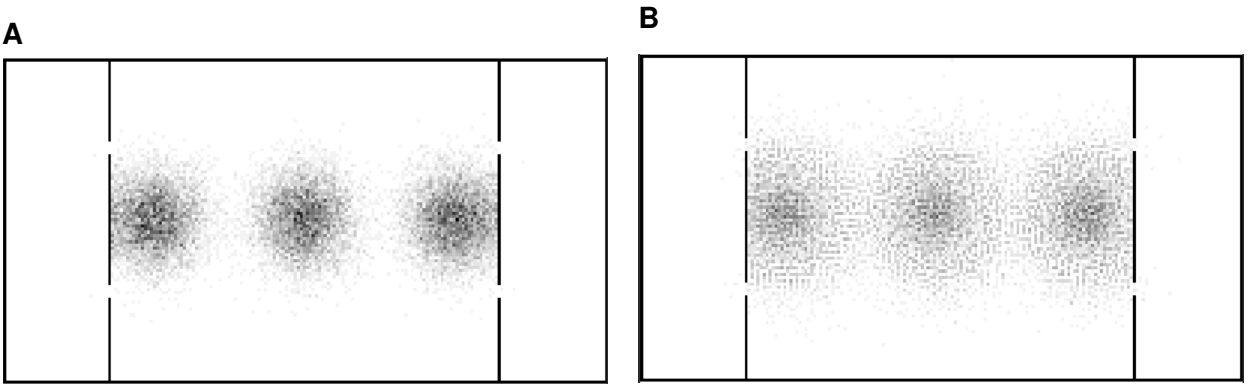

Figure 21. Simulation of calcium diffusion through plasmodesmata. A calcium release of three calcium channels based on a random walk of 5000 particles is simulated. The color code represents the number of particles per cell (the term cell here refers to the cellular automaton and not to a biological cell): white = 0 particles/cell, black = 250 particles/cell. The panels show the distribution of the particles at different points in time: 100 time steps after particle release, only 2 to 3 individual particles made it through the plasmodesmata (**A**), 300 time steps after release there are 15-20 particles that have moved through the plasmodesmata (**B**).

5.7 Modeling the calcium wave using a cellular automaton

The superior research goal concerning calcium waves in plants is to decipher and understand the biological background. My work focuses on the question of how these waves propagate across the individual cells from the starting point to the end point and how these waves of increased concentrations of intracellular calcium overcome the cell wall border. One approach to answering this question was to create a stochastic model that simulates the propagation of the calcium wave with simple rules. A cellular automaton is ideal for this: the cellular automaton is based on simple rules and the information is passed on at local level from one unit to the next. Therefore, in a first step I tried to reproduce the experimental test results that are shown in the kymograph with a one-dimensional cellular automaton. The cellular automaton cell does not necessarily have to depict a biological cell since the resolution of the camera used does not allow investigations at the level of individual cells. The first task was to see whether the results can be reproduced with a cellular automaton.

The aim of this first model was to recreate the kymograph of a stimulation experiment. A typical stimulation with a biotic stimulus such as flg22 or chitin should be the reference. Since it was not possible to determine the actual biological cell boundaries, the cell size of the cellular automaton was chosen in such a way that a cell represents a pixel of the kymograph (when the term "cell" is used in the following, this means a cell of the cellular automaton). A temporal development step of the cellular automaton thus corresponds to a single image of the experiment. Since I did not find any suitable examples in the literature on how the experimental data of the calcium wave can be converted into a model of a cellular automaton, I tried different approaches and empirically determined the rules and parameters that could represent a calcium wave in a cellular automaton.

I used the following rules and parameters for my first model: Each cell can assume exactly two states, low calcium concentration and high calcium concentration, simulated in the model by states 0 and 1 or in the graphical representation by the colors blue and yellow. A cell with low calcium, whose neighboring cells are low in calcium, will also be low in calcium in the next step. A cell that has one or two neighboring cells with a lot of calcium has a 90 % probability that it will have a lot of calcium in the next development step. If a cell has high calcium then its condition is independent of its neighboring cells for a certain number of development steps and behaves like a state machine. A cell with a lot of calcium maintains this state for 18 developmental steps, after which it automatically switches to the low calcium state and also maintains this state for a further 50 developmental steps independently of its neighboring cells. Only then does it react again to the state of its neighboring cells. This scheme is intended to simulate the biological behavior of the cell: If a biological cell has a high calcium concentration in the cytosol due to the opening of calcium channels, this concentration is only maintained for a short time until the ion pumps have carried the calcium out of the cell into the intercellular space or the ER or the vacuole. Thereafter, the calcium concentration in the cytosol remains at the low level for a minimum time due to the refractory period of the calcium channels, which only allow reopening after a minimum waiting period. This also serves to protect the cell, since a constantly high calcium concentration is dangerous for the cytosol and would destroy the functionality of the cell. In addition, the closure of the channels with the subsequent refractory period prevents self-excitation of the cell with calcium-controlled calcium channels. Otherwise these channels would keep themselves permanently open due to the incoming calcium and would be useless. At the beginning of the simulation, all cells of the cellular automaton have a low calcium concentration. In order

for a wave to develop at all, after a certain number of development steps (time before the application of the stimulus plus delay time after the stimulation), a number of connected cells were set to a high calcium concentration. The kymograph representation of this simple cellular automaton model, in which the cells can only hold two states, low and high calcium, shows a roof-shaped structure of two thick tilted lines, which represent the course of the wave in both directions (Figure 22A).

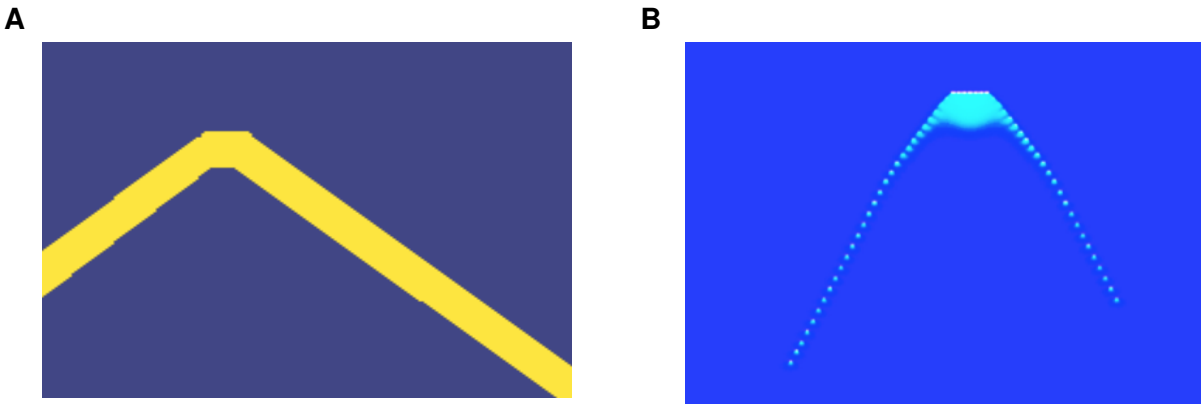

Figure 22. Simple stochastic model of calcium signatures based on a cellular automaton generating a kymograph (**A**). For generating a more realistic kymograph result (**B**) similar to the experimental data additional rules were necessary.

At first glance, the results of the simulation do not have much in common with the kymograph of the experimental data. The graphical output of the simulation simply consists of two thick oblique lines. Nevertheless, this result is very informative and gives an indication that complex processes take place in the background with the calcium wave. But first let's see what the differences are. Two significant differences emerge: on the one hand, the intensities vary greatly in the original kymograph, the calcium concentration along the root is not completely uniform even in the unstimulated state. In the stimulated state, the differences increase: the closer a position is to the starting point, the greater the intensity. On the other hand, the propagation in the original data does not have an exactly linear course as in the simulation, in particular the propagation velocities of the wave towards the tip and the branch are different.

Therefore, I expanded the cellular automaton model. I introduced different intensity states for the individual cells of the cellular automaton. So the cells have different intensities according to their position along the root even in the unstimulated state. More precisely, there is an area at the tip of the root that always has a very high basic intensity and an area in the elongation zone that has a slightly higher basic intensity. If a cell is excited by its neighboring cell, the intensity slowly increases to a maximum, remains there for a certain number of developmental steps and then slowly decreases again. In order to take into account the different wave speeds in the direction to the tip and to the shoot, I used different excitation probabilities of excitation for the right and left neighboring cells: if the cell with the high concentration is to the left of a cell with the low concentration, it is more likely to be excited than if the cell with the high concentration is to the right of the cell with the low concentration. This results in different slopes in the simulation, i.e. the wave spreads out towards the shoot with a higher speed than towards the tip. Figure 23B shows the result of the simulation, which was parameterized on the basis of experimental data from a stimulation with flg22 (Figure 23A).

This simulation also shows only limited similarity with the experimental data. I decided to expand the rules of the cellular automaton again. As a reference I chose a data set from a C8 experiment, which shows a particularly clear wave propagation and where the non-linearity of the wave propagation is clearly visible in the kymograph (Figure 23C). It can be described approximately with a quadratic function. I also chose this example because it can be clearly seen here that the maximum intensity of the wave does not necessarily have to be at the start position of the wave, but in an area between the start position and the tip of the root. Obviously, the maximum intensity of the calcium wave depends on the basic intensity that is already present without stimulation. The maximum intensity at a position also depends on the distance from the starting position, with increasing distance the wave weakens. With a number of additional rules I extended the cellular automaton so that a simulation very similar to the original resulted (Figure 23D).

With this extended set of rules it was possible for me to approximately reproduce a kymograph. However, there are some fundamental issues. The idea of the cellular automaton is to generate complex behavior with simple rules. Here, however, complex behavior is simulated with complex rules. The question is whether a cellular automaton is the right choice of model. In addition, the cellular automaton is based on the fact that the same rules apply to all cells and the complex behavior only emerges due to the different conditions in the environment. When simulating the wave, however, the intensity seems to be related to the basic intensity in any case, so not all cells are fundamentally the same.

Another problem arose from the fact that the intensity of the wave decreases with the distance from the starting point. In order to simulate such behavior, either a global variable must be measurable, e.g. each cell must be able to measure its distance from the starting point of the wave. Alternatively, the information about the distance from the starting point has to be passed on with the wave, as I programmed it in my model. Each cell commits the next cell a value indicating how far it is from the starting point. The receiving cell increases this value by one and then passes it on again. In this way, each cell knows its distance from the starting point and can adjust the intensity of its excitation accordingly. Such a system seems unrealistic in practice.

For the aforementioned reasons, it seems to make sense not to pursue the modeling of the calcium wave by means of a cellular automaton. Instead, it makes sense to first see whether the observed properties of the calcium wave such as the decrease in the speed of propagation etc. cannot be better linked to global structures such as the cell size or the positioning of the calcium channels based on CICR.

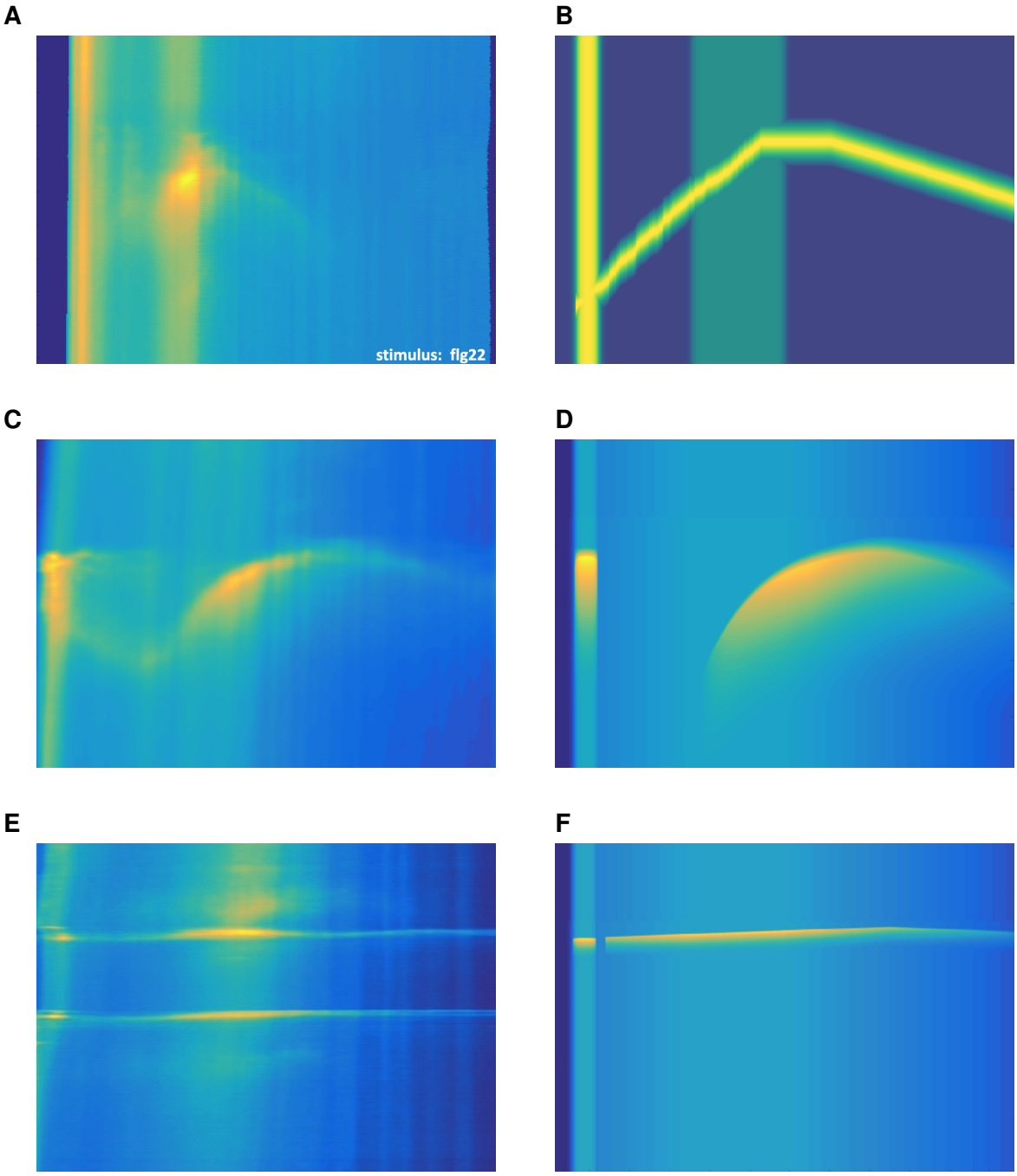

Figure 23. Cellular automaton modeling of the calcium wave using an extended set of rules. Adding different intensities and propagation probabilities (**B**) is not sufficient to reproduce a kymograph of a stimulation with flg22 (**A**). Only a massively extended set of rules gives a realistic simulation result of a kymograph (**D**) based on experimental data of a stimulation with C8 (**C**). For a stimulation with NaCl (**E**) the cellular automaton model output is just a thin horizontal line (**F**).

6 Differential regulation of CPK proteins in guard cells as an example for downstream effects of a calcium-triggered plant response

6.1 Chapter introduction

Plants regulate the aperture of the stomata depending on the environmental conditions. Various stimuli can trigger the closure of the stomata. The guard cells of the stomata must therefore process information from many different sources and convert it into an opening or closing command. It is known that calcium and calcium-dependent CPK proteins play an important role here by targeting the ion channel SLAC1 which induces stomata closure (Vahisalu et al., 2008). To transport different information to varying receivers it is necessary that the decoders have specific sensitivity to the intracellular level of calcium. Calcium is able to encode information not only by the concentration level itself but also by modifying the shape of the level over time, e.g. by oscillations or spikes or bursts (Larsen and Kummer, 2003; Smedler and Uhlén, 2014).

The fact that sustained elevated levels of intracellular calcium are toxic to the cell, may also play a role here and might have coerced the calcium signal only appearing in short pulses. My initial analysis focused on the different regulation of calcium-dependent protein kinases in plants by different concentration levels of calcium assuming a chemical steady state - still aware that calcium dynamics may induce a far broader range of signaling response.

6.2 CPKs are regulated by calcium

There are three known classes of calcium-dependent proteins that can be found in plants: calmodulin interacting with calcium-calmodulin-dependent kinases (CCaMKs), calcineurin B-like (CBL) calcium sensor proteins interacting with CBL-interacting Protein Kinases (CIPKs) and calcium-dependent protein kinases (CDPKs) (Yang and Poovaiah, 2003). In the model plant *Arabidopsis thaliana* CDPKs are called CPKs. Furthermore, there are CDPK-related kinases (CRKs) that have degenerated binding sites for calcium and therefore cannot bind calcium anymore. CDPKs are calcium-binding serine/threonine protein kinases which combine a calcium sensor protein and an effector protein in one molecule. CDPKs are not available in animals and fungi, but can be found in plants and in Apicomplexa (protists) e.g. *Plasmodium falciparum* (Billker et al., 2009; Valmonte et al., 2014).

Arabidopsis thaliana has 34 isoforms of CPKs (Cheng et al., 2002). Typically, a CPK protein can be divided into five domains: N, K, J, CaM-LD and C (Figure 24). The C-terminal end of the catalytic domain of the kinase (K) is connected via a junction (J) with a regulatory calmodulin-like domain (CaM-LD) with usually four binding sites for calcium, also known as EF hands. The junction consists of an autoinhibitor serving as pseudo-substrate and a binding site for the CaM-LD. CPKs are a member of the superfamily of EF hand calcium-binding proteins. This superfamily is named after its calcium-binding structure E-helix-loop-F-helix first described in the protein parvalbumin (Kretsinger and Nockolds, 1973). Most CPKs have four EF hand calcium-binding motifs which can be split into two independent domains, one N-terminal domain with the cooperative calcium-binding sites EF1 and EF2 and one C-terminal domain with binding sites EF3 and EF4.

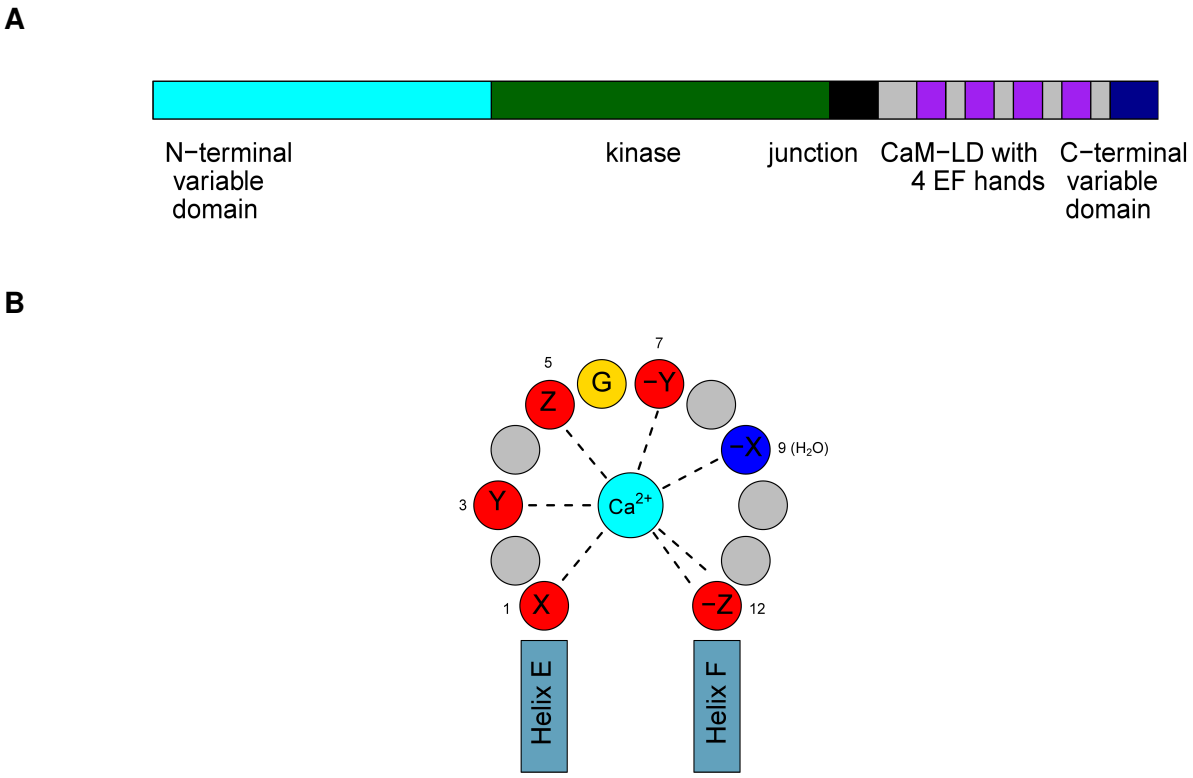

Figure 24. Scheme of conserved CPK protein structure (**A**) and calcium-binding EF hand motif (**B**). All CPK proteins reveal a uniform structure: N-terminal variable domain (cyan), kinase domain (green), autoinhibitory junction domain (black), the calmodulin-like domain (CaM-LD; gray) with four EF hand motifs (purple), and the C-terminal variable domain (dark blue). The calcium-binding EF hand motif has a E-helix-loop-F-helix structure. The loop is formed by 12 amino acids, which are usually described by the formula X ∗ Y ∗ Z G -Y ∗ -X ∗ ∗ -Z. Calcium binds to the amino acids that are marked with X, Y, Z, -Y, and -Z. These amino acids provide oxygen atoms for calcium binding (red circle). The amino acid at position 9 (-X) forms a hydrogen bond to a water molecule, which in turn binds to calcium via its oxygen atom (blue circle). At position 6 there is glycin which is strongly conserved due to a stable conformation of the loop (yellow circle). The geometry of the loop is formed by a pentagonal double pyramid.

An analysis of the amino acid sequence of the CPK proteins CPK21 and CPK23 showed that both proteins contain four EF hand binding sites for calcium (Table 6). In CPK23 one of the four EF hands is degenerated: in the sequence of EF hand 1 there is glutamine (one letter code: Q) at position 12 instead of glutamic acid (one letter code: E). It is therefore assumed that this EF hand has only a weak affinity for calcium (Geiger et al., 2010).

It is known, that the binding of calcium ions to the EF hands occurs in a cooperative manner, i.e. the binding of one ion influences the binding of further ions to the other binding sites (Nelson et al., 2001). Most calcium-dependent proteins show positive cooperativity, so if one ion is already bound, the next one binds with higher affinity. The fraction of calcium occupied protein to the total amount of protein as a function of the concentration of free calcium reveals a sigmoidal shape. Cooperativity in steady state can be described quite comfortably with only two parameters using the Hill equation, which represents a simple empirical concentration-response relationship without a priori knowledge of the underlying

mechanisms being necessary (Hill, 1910; Gesztelyi et al., 2012).

The crucial parameters of the Hill equation are the dissociation constant K_d which represents the ligand concentration at half-maximum occupancy of the molecule and the Hill coefficient h which represents the steepness of the binding curve. Then the response f of a biochemical system can be calculated as the function of the concentration of the ligand x where basal represents the basic response unrelated to binding of the ligand:

$$f(x) = v_{\max} \cdot \frac{x^h}{{K_d}^h + x^h} + \text{basal} \tag{14}$$

In a publication from 2010, the researchers around Dietmar Geiger in Würzburg examined the activity of the proteins CPK21 and CPK23 as a function of varying concentrations of calcium (Geiger et al., 2010). In an in vitro kinase (IVK) assay, the relative phosphorylation activity in steady state was determined by radioactivity measurements of radio-labeled [γ^{32}]-ATP from gel slices containing N-terminal protein fragments of SLAC1 (NT-SLAC1). With the kind permission of Dietmar Geiger, I used the results of the IVK assay experiments as the basis for my modeling of CPK proteins and for further analysis (Figure 25).

Values were taken from figure 4B of the publication by Geiger et al. (2010). The experimental data consisted of two data series each for CPK21 and CPK23. Fitting these data to a Hill equation revealed a Hill coefficient of around 20 for CPK21 and around 0.5 for CPK23. Given the fact that CPK21 has only four binding sites for calcium and the maximum cooperativity therefore is limited to 4 I set an upper limit of 4 for the Hill coefficient (Table 5). In the fitting algorithm the relative phosphorylation was not limited to a maximum of 1, which in case of CPK23 resulted in a parameter set that can exceed 1 for high concentrations of calcium (v_{max} + basal > 1).

Table 5: Function parameters of a Hill function describing the phosphorylation activity of CPK21 and CPK23.

protein	K_d	$v_{\max}$	h	basal
CPK21	275	0.976	4	0.0236
CPK23	761	0.828	0.495	0.4626

The parameters were calculated by fitting a Hill function to experimental in vitro assay data. The Hill coefficient h was limited to a maximum of 4.

6.3 Modeling the phosphorylation activity of CPK proteins

For a better understanding of the molecular processes involved in the activation of the CPK proteins, I wanted to design a model based on the experimental steady-state data from the lab of Dietmar Geiger in Würzburg that also describes the kinetics of the calcium-binding. For this purpose I used a simplified version of a Monod-Wyman-Changeux (MWC) model first described for the cooperative binding of calcium to calretinin (Faas et al., 2007). In a MWC model, also called symmetry model, it is assumed that binding of one calcium ion

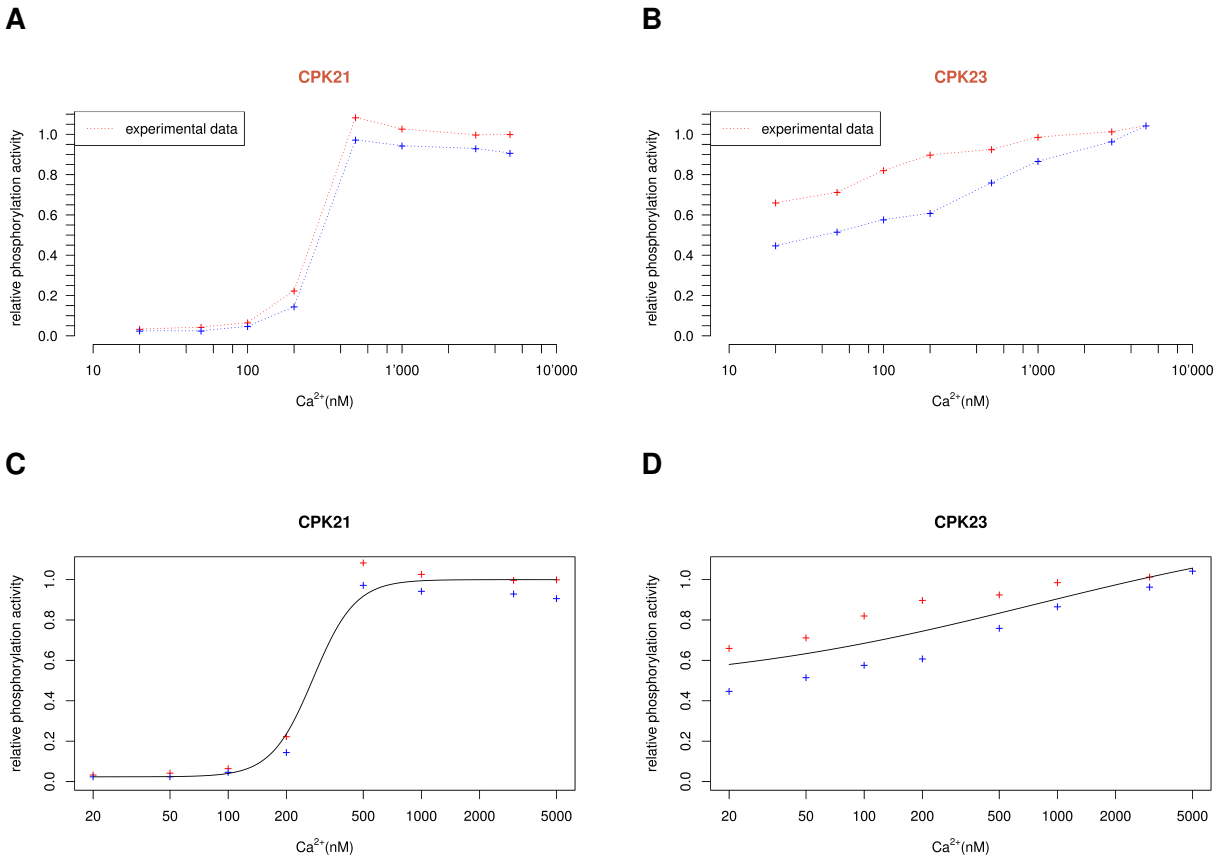

Figure 25. Relative phosphorylation activity of the proteins CPK21 and CPK23. Phoyphorylation was measured in steady state using SLAC1 as a substrate (**A**, **B**). Experiments were performed by the Geiger Lab in Würzburg and published in 2010 (Geiger et al., 2010). Data were fitted using the Hill equation $f(x) = v_{\max} \cdot x^h/(K_d^h + x^h) + \text{basal}$ with a maximum Hill coefficent of $h = 4$ (**C**, **D**). See Equation 5 for the estimated parameters of the Hill curve resulting from the fitting procedure.

to a binding site instantaneously changes the affinity of the cooperative binding site. The states of the binding sites in a MWC model are termed T-state (tense state, low affinity) and R-state (relaxed state, high affinity). In the apoprotein no calcium is bound and all sites are in the T-state. Binding of calcium to a binding site immediately switches this site as well as the corresponding cooperative site to the R-state and increases its affinity for further binding.

The sequence analysis of the CPK proteins shows that they each have 4 binding sites for calcium, so-called EF hands (Table 6). Therefore, in a first step, I created a model that includes five biomolecular variants of the protein: the apoprotein without calcium, the protein occupied with one calcium ion, and protein occupied with two, three and four calcium ions (CPK_ca0 to CPK_ca4). The assumption was that if there are several unoccupied binding sites, the one with the highest affinity is always occupied first. Therefore I did not differentiate which of the four binding sites were occupied, but only the number of occupied binding sites was relevant.

In this model, the total phosphorylation activity was given by the sum of the phosphorylation activities of the individual variants, each of which was included in the total activity with a weighting factor w_i (Equation 15). The weighting factor of the unoccupied protein w_0 was

Table 6: Sequence characteristics of the binding sites for calcium (EF hands) of CPK proteins CPK21 and CPK23. For each EF hand, the associated amino acid sequence is listed in one-letter code. Data were taken from UniProt, retrieved 30 June 2020 (Apweiler et al., 2004; The UniProt Consortium, 2019)

Protein (token)	Protein (full name)	UniProt name	UniProt ID	Ordered locus name
CPK21	Calcium-dependent protein kinase 21	CDPKL_ARATH	Q9ZSA2	At4g04720
CPK23	Calcium-dependent protein kinase 23	CDPKN_ARATH	Q9M101	At4g04740

Protein	EF hand 1 N-terminal site	EF hand 2	EF hand 3	EF hand 4 C-terminal site
CPK21	DTDKSGTITYEE	DVDGNGTIDYYE	DKDNSGHITRDE	DTDNDGRINFEE
CPK23	DTNRSGTITYEQ	DVDGNGTIDYYE	DKDKNGHITRDE	DTDNDGKINFEE

set to the relative activity value (mean value of both data series) at the lowest concentration of calcium which is 20 nM. The weighting factor of the protein fully occupied with four calcium ions w_4 was set to 1 assuming that the fully occupied protein is the most active form. The relative phosphorylation activity was calculated by the ratio of the active protein to the total protein concentration:

$$\text{activity} = \frac{\sum_{i=0}^{4} w_i \cdot [\text{CPK\_ca}_\text{i}]}{\sum_{i=0}^{4} [\text{CPK\_ca}_\text{i}]} \tag{15}$$

The parameters w_0 to w_4 in this equation indicate the weight with which the respective protein variant contributes to the total activity.

The transition from one protein variant to the next was simulated by means of a mass reaction, with a dissociation constant for the forward reaction and a dissociation constant for the reverse reaction. This resulted in 11 parameters that had to be determined: 4×2 dissociation constants of the individual reactions and 3 weighting factors for the proteins with one, two or three calcium ions.

Since in the steady state only the ratio of the dissociation constants from the back and forth reaction is essential and the absolute values are only relevant for the speed of the reaction, the constants for the reverse reaction (k_{off1}, k_{off2}, k_{off3}, k_{off4}) were fixed at 0.1 reducing the number of unknown parameters to seven. In a deterministic model like this, the volume has no effect on the concentrations of the proteins. A volume of 1 liter was used as the default

value for all simulations. The reaction equations of the model are:

$$
\begin{aligned}
\frac{d([\text{CPK\_ca0}]\cdot V)}{dt} &= -V\cdot k_{\text{on1}}\cdot[\text{CPK\_ca0}]\cdot[\text{Ca}] + V\cdot k_{\text{off1}}\cdot[\text{CPK\_ca1}] \\
\frac{d([\text{CPK\_ca1}]\cdot V)}{dt} &= +V\cdot k_{\text{on1}}\cdot[\text{CPK\_ca0}]\cdot[\text{Ca}] - V\cdot k_{\text{on2}}\cdot[\text{CPK\_ca1}]\cdot[\text{Ca}] \\
&\quad - V\cdot k_{\text{off1}}\cdot[\text{CPK\_ca1}] + V\cdot k_{\text{off2}}\cdot[\text{CPK\_ca2}] \\
\frac{d([\text{CPK\_ca2}]\cdot V)}{dt} &= +V\cdot k_{\text{on2}}\cdot[\text{CPK\_ca1}]\cdot[\text{Ca}] - V\cdot k_{\text{on3}}\cdot[\text{CPK\_ca2}]\cdot[\text{Ca}] \\
&\quad - V\cdot k_{\text{off2}}\cdot[\text{CPK\_ca2}] + V\cdot k_{\text{off3}}\cdot[\text{CPK\_ca3}] \\
\frac{d([\text{CPK\_ca3}]\cdot V)}{dt} &= +V\cdot k_{\text{on3}}\cdot[\text{CPK\_ca2}]\cdot[\text{Ca}] - V\cdot k_{\text{on4}}\cdot[\text{CPK\_ca3}]\cdot[\text{Ca}] \\
&\quad - V\cdot k_{\text{off3}}\cdot[\text{CPK\_ca3}] + V\cdot k_{\text{off4}}\cdot[\text{CPK\_ca4}] \\
\frac{d([\text{CPK\_ca4}]\cdot V)}{dt} &= +V\cdot k_{\text{on4}}\cdot[\text{CPK\_ca3}]\cdot[\text{Ca}] - V\cdot k_{\text{off4}}\cdot[\text{CPK\_ca4}]
\end{aligned}
\tag{16}
$$

6.4 Parameter estimation

In order to determine the seven unknown parameters I ran a parameter estimation using the software tool COPASI/CoRC. I chose the differential evolution algorithm as the method for parameter estimation because this method makes few assumptions about the underlying estimation problem and can search through large parameter spaces (Storn and Price, 1997). The disadvantage of this method is that there is no guarantee that the optimal solution will be found. I overcome this disadvantage by repeating the estimation runs many times on a compute cluster. The parameter estimation was repeated around 6200 times for each model, each run starting with random starting values for the parameters. The starting values were uniformly distributed in a range between 10^{-6} and 10^{6}. Figure 26 shows a histogram view of the parameter estimation results.

In order to further limit the large number of parameter sets, I sorted the results in ascending order according to the estimation error, i.e. according to the quality of the parameter estimation. Then I took a closer look at around 1 percent of the best parameter sets (Figure 27). It is noticeable that 5 of the 7 parameters have almost an identical value for all parameter sets. In the CPK21 model, only the binding rates k_{on3} and k_{on4} show larger variations within the different parameter estimation results. In the CPK23 model the binding rates k_{on1} and k_{on2} vary considerably. It is also noticeable that the first intermediate is weighted with 0 in both models (parameter w_1). To see whether there is a dependency between the varying parameters, I plotted the two most strongly varying parameters against each other: these are k_{on3} and k_{on4} for CPK21 and k_{on1} and k_{on2} for CPK23. The scatter plot reveals that for CPK21 there is a pretty clear dependency between k_{on3} and k_{on4}, the graph shows an almost linear even slightly quadratic or exponential dependency (Figure 28A). For CPK23, the dependency is less pronounced, but a certain linearity can be seen (Figure 28B). From the parameter sets with the lowest estimation error, I selected a representative parameter set for each protein (Table 7).

With this model, the dynamic behavior of the CPK proteins could be investigated. Figure 29 shows as an example a simulation of reaction kinetics in which the calcium concentration increases linearly with time from 0 to 1000 nM.

A CPK21

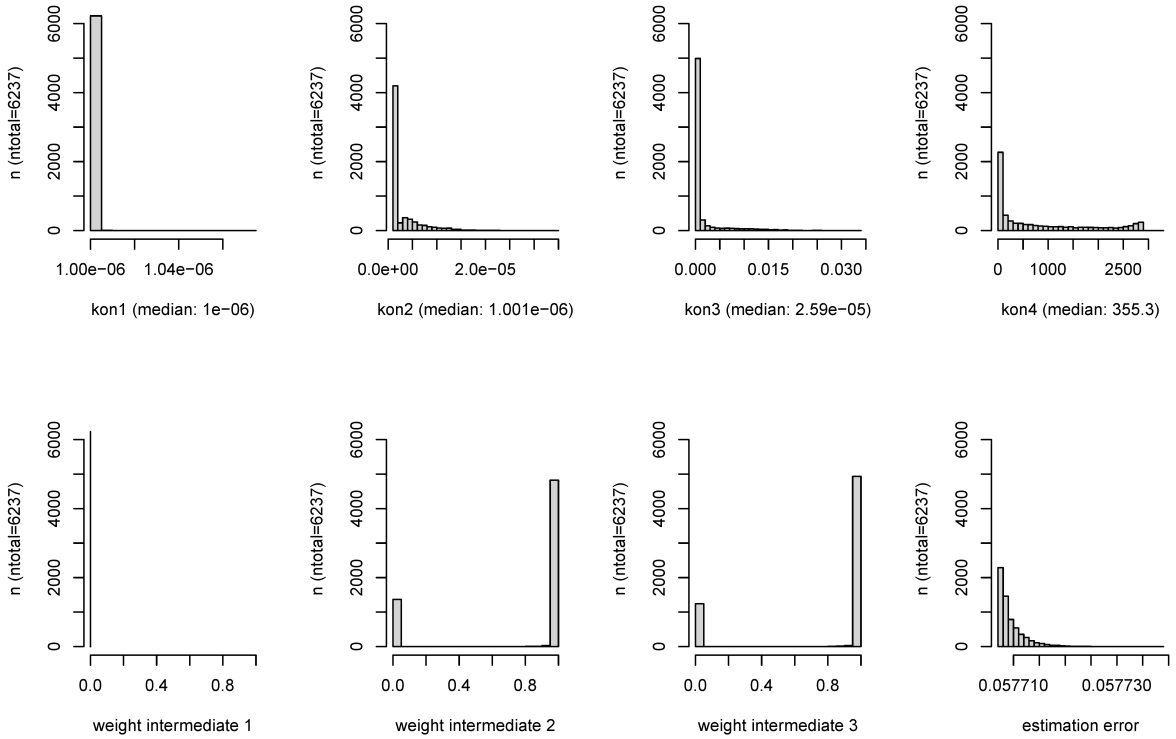

B CPK23

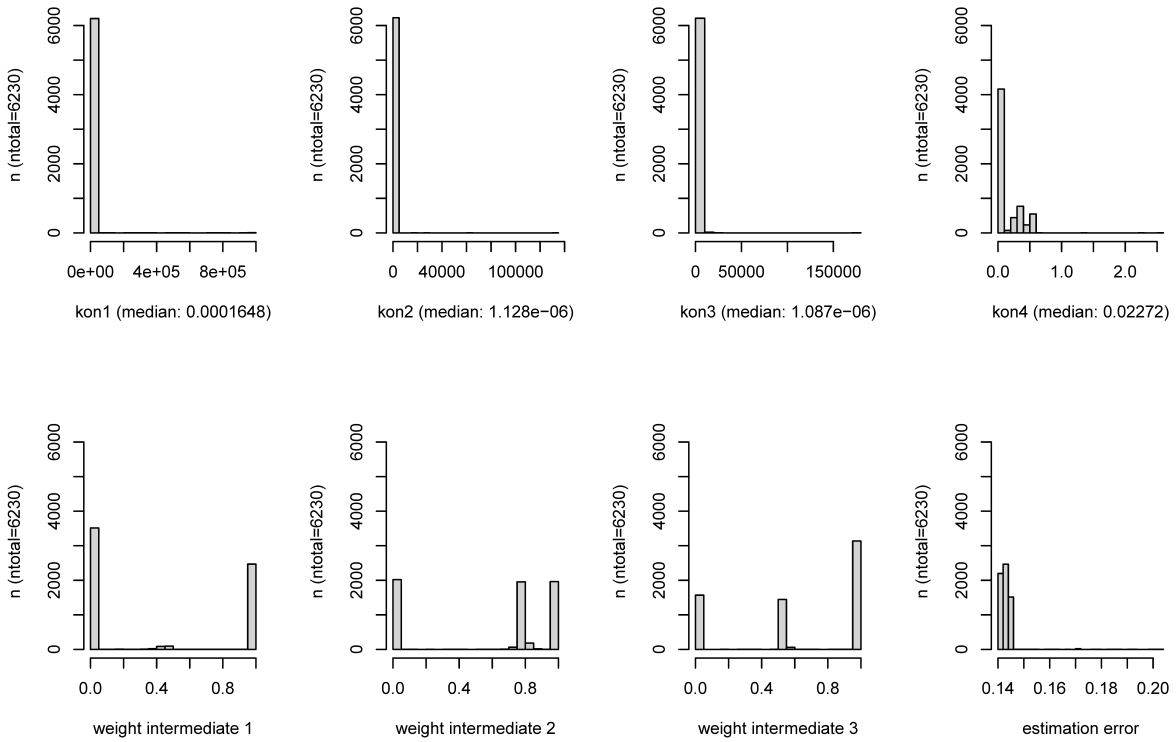

Figure 26. Histograms of the parameter estimation run of the models for CPK21 (**A**) and CPK23 (**B**) based on the steady state data of the Geiger Lab in Würzburg. Number of parameter sets: CPK21: n=6237, CPK23: n=6230.

A CPK21

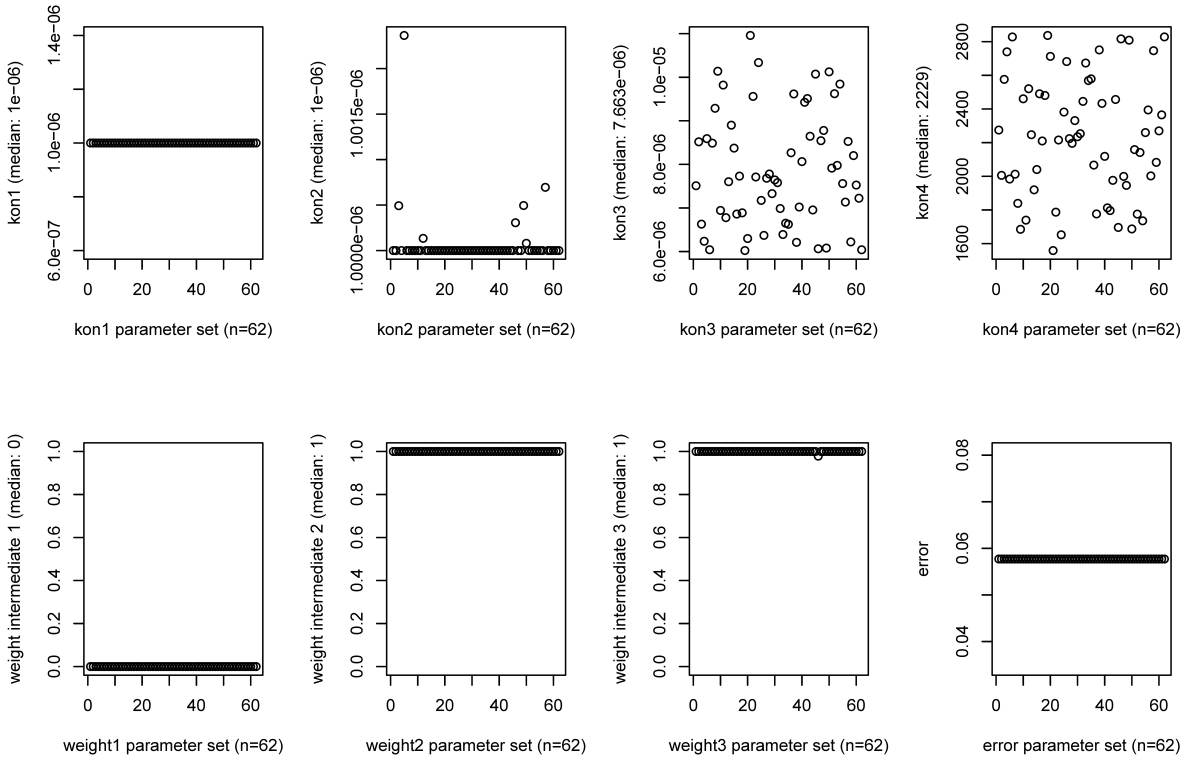

B CPK23

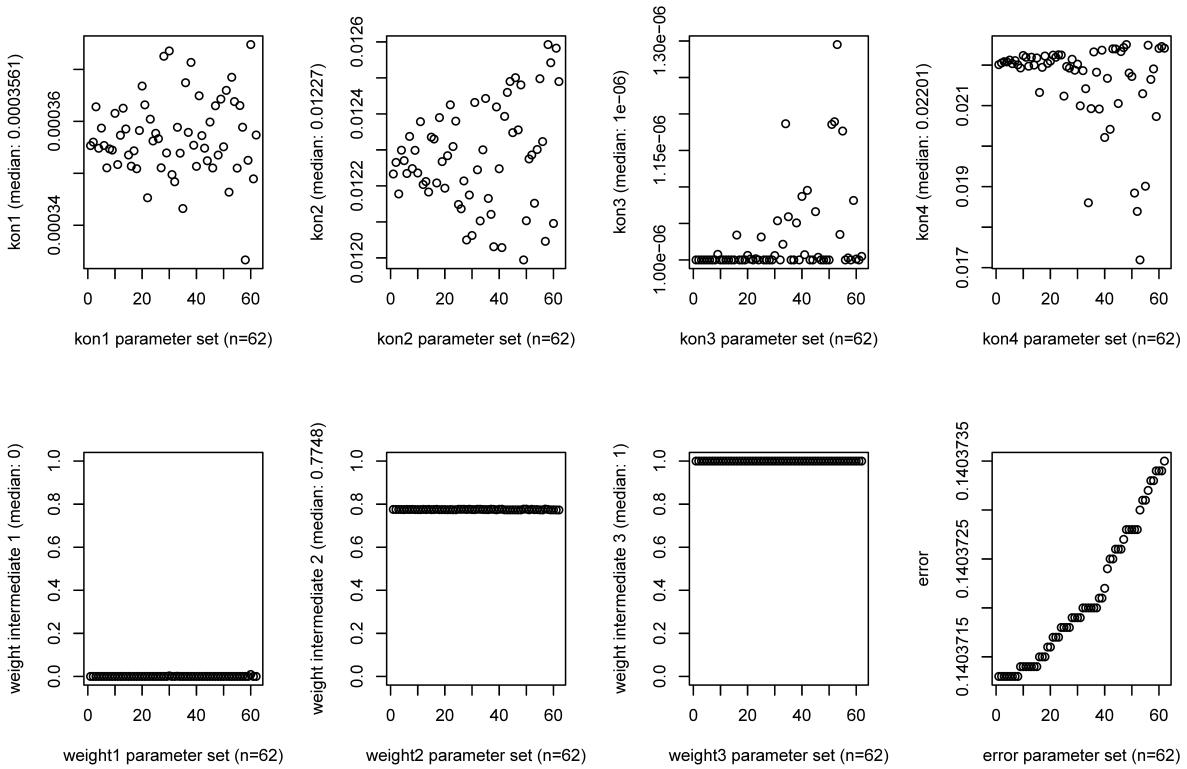

Figure 27. Selected parameter sets for modeling CPK21 (**A**) and CPK23 (**B**) based on the steady state data of the Geiger Lab in Würzburg. Of all data sets, the 1 % with the lowest estimation error were selected. Number of parameter sets: CPK21: n=62, CPK23: n=62.

A CPK21 **B CPK23**

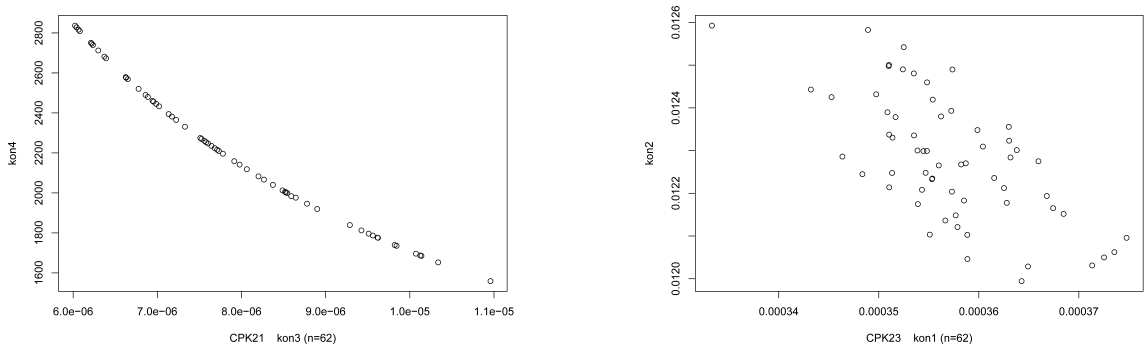

Figure 28. Parameter dependencies of the estimation results between the activation rates k_{on3} and k_{on4} for CPK21 (**A**) and k_{on1} and k_{on2} for CPK23 (**B**). Data are based on the steady state data of the Geiger Lab in Würzburg. Number of parameter sets: CPK21: n=62, CPK23: n=62.

Table 7: Model parameters for CPK21 and CPK23.

protein	k_{on1}	k_{on2}	k_{on3}	k_{on4}	k_{off}	w_0	w_1	w_2	w_3	w_4
CPK21	1e-6	1e-6	6.943e-6	2460.426	0.1	0.0294	0	1	1	1
CPK23	0.000355	0.0122	1e-06	0.0220	0.1	0.5543	0	0.775	1	1

The parameters w_0, w_1, w_2, w_3, w_4 denote the activity weighting of the protein with 0, 1, 2, 3, 4 calcium ions bound. The corresponding rates for unbinding calcium k_{off1}, k_{off2}, k_{off2}, k_{off4} were set to 0.1.

A **CPK21**

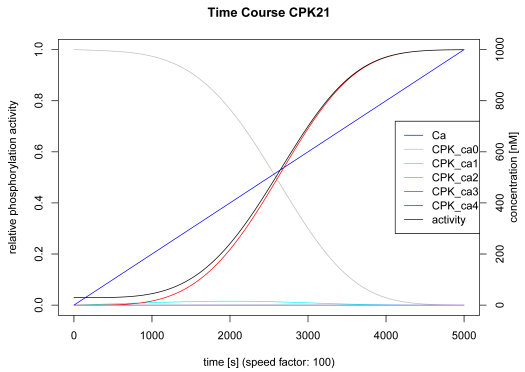

B **CPK23**

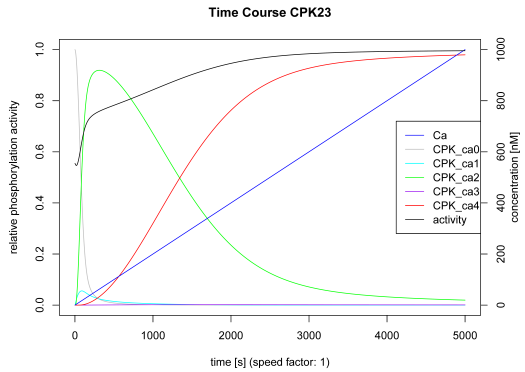

C **CPK21**

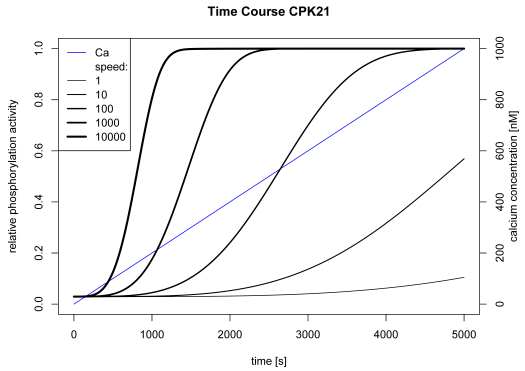

D **CPK23**

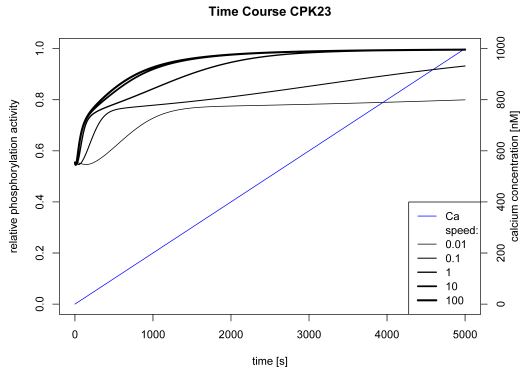

Figure 29. Reaction kinetics of the CPK proteins CPK21 (**A**) and CPK23 (**B**) in response to a linearly increasing calcium concentration from 0 to 1000 nM within a time period of 5000 seconds. The choice of the speed factor influences the dynamics of the phosphorylation activity as shown here for CPK21 (**C**) and CPK23 (**D**). The dynamic CPK model, which was described in Equation 16 and was parameterized according to Table 7, served as a basis. The relative phosphorylation activity was calculated accordind to Equation 15. The speed factor, which is the factor by which all binding and unbinding rates are multiplied, was chosen to be 100 for CPK21 and 1 for CPK23. At the beginning of the simulation, the concentration of the unoccupied protein CPK_ca0 was 1000 nM, the concentration of all other variants of the CPK protein was 0. The simulations were run using COPASI/CoRC.

6.5 Stimulation of guard cells and epidermal cells

In the previous sections, I used experimental data to model the activity behavior of CPK21 and CPK23. I modeled the activity by means of a Hill function as well as a more sophisticated kinetic model. In the next step, I deployed this model to simulate the stress response in guard cells of stomata. As an input for the model, I used experimental calcium time series provided by Melanie Krebs, a researcher from the Schumacher Lab in Heidelberg. These data have already been published in an article (Keinath et al., 2015). The leaves of *Arabidopsis* plants that express the calcium sensor R-GECO1 were stimulated with flg22 and chitin and recorded using a microscope camera. The calcium concentration of different cell types, guard cells and epidermal cells, was determined based on the fluorescence intensity. The recording time was approximately 70 minutes in total, 30 minutes before and approximately 40 minutes after the stimulation. It turned out, that the intracellular calcium concentration increased in multiple short pulses after the stimulation (Figure 30).

A closer look at the calcium data revealed that the base concentration after disapperance of the calcium pulses is approximately 50 nM, which is considerably lower than before the stimulation (approximately 70 nM). This is not only surprising, but also raises a general problem: The prerequisite for a differential regulation of the CPK proteins by calcium is that these react very sensitively to the intracellular concentration of calcium. In consequence, a lower basal concentration of calcium after the stimulation leads to lower overall activity of the CPK protein compared to the activity before the stimulation. The short activity peak as a direct result of the stimulation cannot compensate for this decrease. My assumption was that the drift of the basal concentration is an artifact from the measurement procedure and that the drift can be mathematically eliminated from the concentration. Assuming that the basal concentration in an ideal test arrangement has to be constant over the entire test period, I calculated the deviation from the basal concentration for each concentration value c_i and corrected the data accordingly:

$$c_i^* = c_i - b_i + b_{\text{const}} \tag{17}$$

Here, c_i^* represents the corrected concentration for data point i at time t_i. The smoothed baseline of the calcium concentration excluding the peaks is depicted by b_i. The value b_i at data point i is estimated by the median of all measured concentration values in the range 5 min before to 5 min after time t_i. Mathematically, b_i corresponds to a sliding median with a window size of 10 minutes (corresponding to 120 data points with a period of 5 seconds). Since the duration of a calcium peak is approximately 2 minutes, i.e. a small fraction of the window size, the basal concentration can also be estimated quite well at the peaks. For calculating the corrected concentration c_i^*, the basal concentration b_i derived from the measurement data is replaced by a fixed offset b_{const} that reflects the constant basal concentration in an unbiased system. I determined the parameter b_{const} by calculating the mean of the baseline values b_i between timepoint -15 min and time point 0 min. Figure 30 shows a comparison of the data before and after correction: the raw data are depicted in black, the baseline in red and the corrected data in blue. All further investigations were based on the corrected calcium data.

Another assumption of my model was that the molecular structure of the cell with respect to the CPK proteins in guard cells and epidermal cells is identical. I used the same model

for simulating the activity of the CPK proteins for both cell types. From a mathematical point of view, the only difference between the simulation of guard cells and epidermal cells was that different calcium time series were used as input for the model.

In a first step, I used a suitably parameterized Hill function as a model for the simulation of the guard and epidermal cells (see Equation 14 and Table 5). This function was fitted to the experimental steady state data and is equivalent to a dynamic model that instantaneously adapts the concentration of the CPK protein to the calcium input. To quantify the effect of the calcium peaks on the activity of the CPK proteins, I calculated the ratio of the activity before and after the stimulation. The mean value of all data points in the range of 15 minutes before the stimulation until start of the stimulation was used as the reference for the activity without stimulation. The mean value of all measured values from the start of the stimulation until 30 minutes after stimulation was rated as the activity after stimulation. In this model, the stimulation led to a distinguishable increase in activity between CPK21 and CPK23 (Figure 31). While the activity of CPK21 was increased very strongly by the calcium pulses, CPK23 showed only a small change in activity. There were also differences between guard cells and epidermal cells: while an increase of up to 250 percent could be measured in the guard cells when stimulated with flg22, the activity in the epidermal cells only increased by around 100 percent. A similar picture emerged with the stimulation with chitin, however the increase in CPK21 wass smaller overall: in the guard cells CPK21 wass increased by approx. 160 percent and in the epidermal cells by approx. 80 percent.

In summary, I got the following result: stimulation of plant cells with flg22 or chitin leads to an increased activity of CPK21 via calcium signaling. CPK23 is only slightly dependent on calcium. The increase in activity due to stimulation is particularly pronounced in guard cells, which is based on an elevated calcium signaling.

As the calcium signal consisted of several short pulses, it was evident that the reaction speed played a role. In order to test the dependence of the stress response on the speed of calcium binding, I added a speed factor s to the model (Equation 18). I introduced the speed factor as a multiplier by which the reaction rate for binding a calcium ion and the reaction rate for unbinding calcium are multiplied. Thus, the steady state of the reaction is not affected. For convenience, I chose the same factor for all binding and unbinding reactions. For the other parameters of CPK21 and CPK23, I used the values from Table 7 as before. The increase in activity is strongly dependent on the reaction speed (Figure 31C, 31D). The theoretical increase in activity calculated using the Hill function with an assumed instantaneous response is only achieved if the calcium binding takes place very fast overall, in my model at a speed factor of around 10000.

The reaction equations of the extended model incorporating the speed factor s are:

$$
\begin{aligned}
\frac{d([\text{CPK\_ca0}]\cdot V)}{dt} &= -V\cdot s\cdot k_{\text{on1}}\cdot[\text{CPK\_ca0}]\cdot[\text{Ca}] + V\cdot s\cdot k_{\text{off1}}\cdot[\text{CPK\_ca1}] \\
\frac{d([\text{CPK\_ca1}]\cdot V)}{dt} &= +V\cdot s\cdot k_{\text{on1}}\cdot[\text{CPK\_ca0}]\cdot[\text{Ca}] - V\cdot s\cdot k_{\text{on2}}\cdot[\text{CPK\_ca1}]\cdot[\text{Ca}] \\
&\quad - V\cdot s\cdot k_{\text{off1}}\cdot[\text{CPK\_ca1}] + V\cdot s\cdot k_{\text{off2}}\cdot[\text{CPK\_ca2}] \\
\frac{d([\text{CPK\_ca2}]\cdot V)}{dt} &= +V\cdot s\cdot k_{\text{on2}}\cdot[\text{CPK\_ca1}]\cdot[\text{Ca}] - V\cdot s\cdot k_{\text{on3}}\cdot[\text{CPK\_ca2}]\cdot[\text{Ca}] \\
&\quad - V\cdot s\cdot k_{\text{off2}}\cdot[\text{CPK\_ca2}] + V\cdot s\cdot k_{\text{off3}}\cdot[\text{CPK\_ca3}] \\
\frac{d([\text{CPK\_ca3}]\cdot V)}{dt} &= +V\cdot s\cdot k_{\text{on3}}\cdot[\text{CPK\_ca2}]\cdot[\text{Ca}] - V\cdot s\cdot k_{\text{on4}}\cdot[\text{CPK\_ca3}]\cdot[\text{Ca}] \\
&\quad - V\cdot s\cdot k_{\text{off3}}\cdot[\text{CPK\_ca3}] + V\cdot s\cdot k_{\text{off4}}\cdot[\text{CPK\_ca4}] \\
\frac{d([\text{CPK\_ca4}]\cdot V)}{dt} &= +V\cdot s\cdot k_{\text{on4}}\cdot[\text{CPK\_ca3}]\cdot[\text{Ca}] - V\cdot s\cdot k_{\text{off4}}\cdot[\text{CPK\_ca4}] \\
\text{activity} &= \frac{\sum_{i=0}^{4} w_i\cdot[\text{CPK\_ca}_\text{i}]}{\sum_{i=0}^{4}[\text{CPK\_ca}_\text{i}]}
\end{aligned}
\tag{18}
$$

A **flg22**

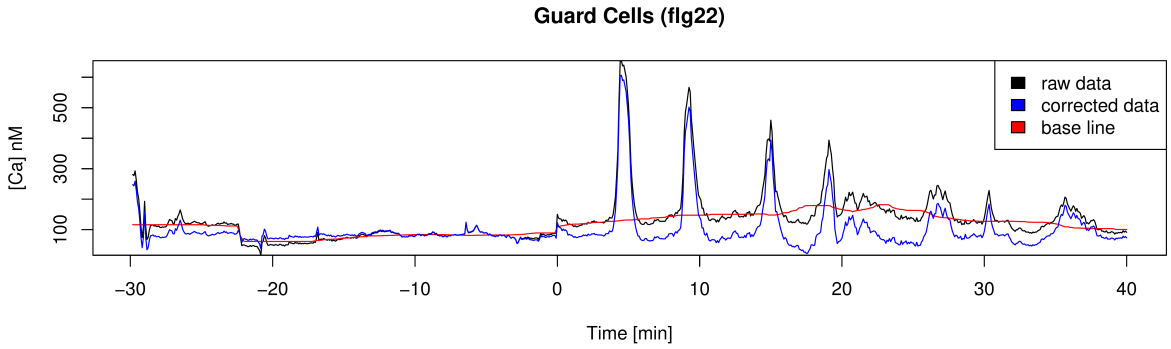

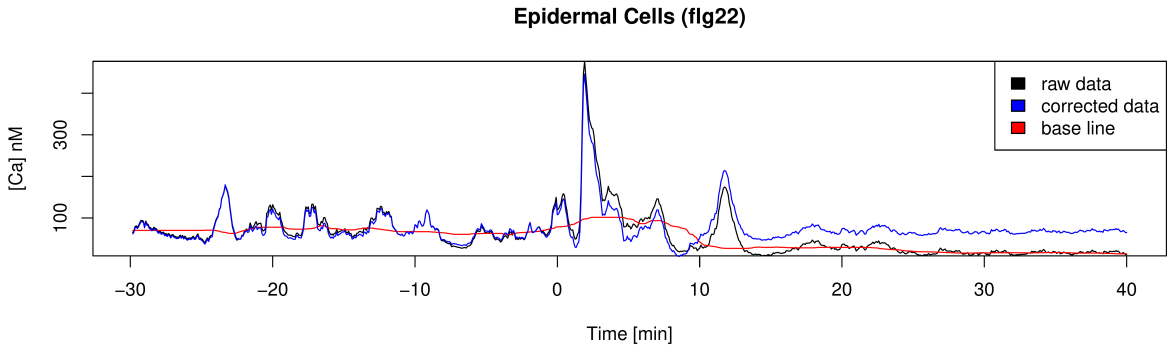

B **chitin**

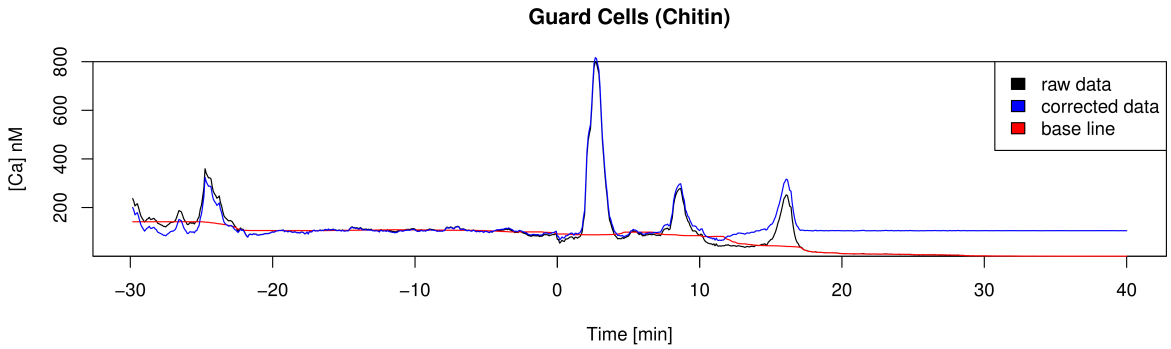

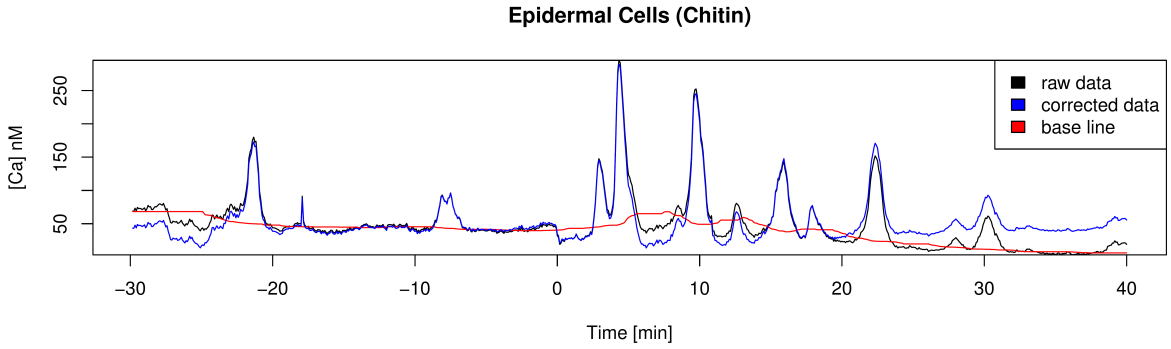

Figure 30. Calcium signaling in response to flg22 (**A**) and chitin (**B**) in guard cells and epidermal cells. The stimulus was applied 30 minutes after starting the data acquisition (time point 0). The graphs show the time-dependent concentration of intracellular calcium before (black line) and after (blue line) drift correction. Assuming a slight drift in the base concentration, data were corrected by subtracting the base line from raw data and adding a fixed offset. The base line was calculated by applying a sliding median with a window width of 10 minutes (red line). The offset was calculated as the mean of the base line between timepoint -15 min and time point 0 min.

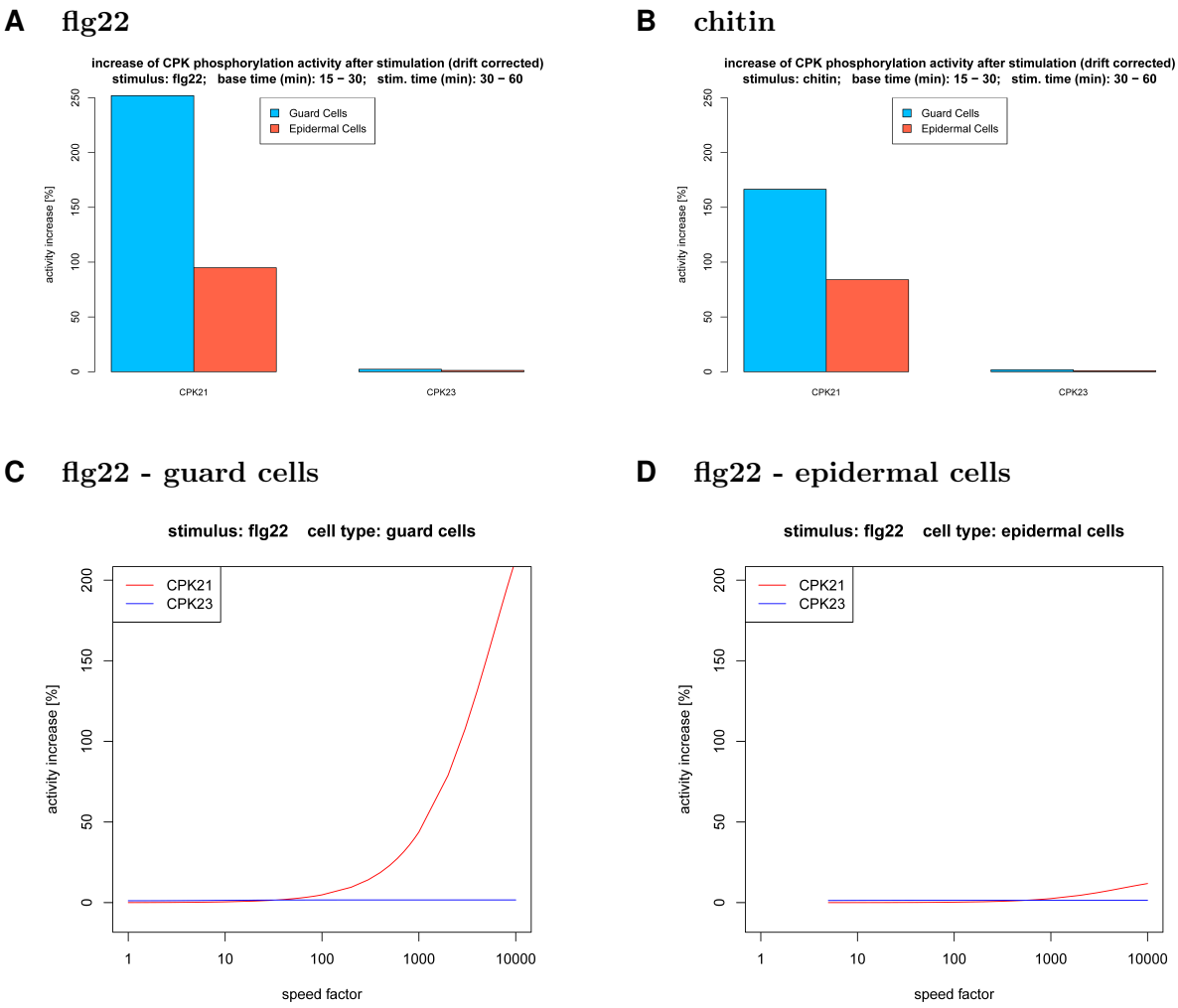

Figure 31. CPK activity increase in response to different stimuli in guard cells and epidermal cells. Panel **A**, **B**: activity increase assuming an instantaneous response of the CPK protein after stimulation with flg22 (**A**) and chitin (**B**). The activity was calculated using a Hill function fitted to the experimental data (see Equation 14 and Figure 25C and 25D). Panel **C**, **D**: activity increase depending on the reaction speed of the calcium binding process simulated by a kinetic binding model of a stimulation with flg22 using differential equations (see Equation 16). For testing different reaction speeds, the binding and unbinding rates of the reaction equations were multiplied with a speed factor in the range from 1 to 10000 (5 to 10000 for the epidermal cells). The increase of the relative phosphorylation activity was calculated as the ratio between base activity (mean activity between timepoint -15 min to 0 min) and activity during stimulation (mean activity between timepoint 0 min to 30 min).

IV Discussion

7 Discussion

7.1 Image analysis

A fundamental component of the image analysis in this project is the object recognition of the root. State-of-the-art object recognition processes use (deep) machine learning and convolutional neural networks (Dollar et al., 2009; Felzenszwalb et al., 2010; Girshick et al., 2014; Redmon et al., 2016; Xiao et al., 2020). In my work I decided to use a more classical object recognition method based on edge detection by thresholding (Vikram Mutneja, 2015). There are several reasons for this: on the one hand, the use of machine learning requires a certain minimum number of data records. Training and test data are required for each type of model. For my analyzes I only had a handful of data sets available for each type of experiment. In addition, deep learning algorithms can easily be misled and may detect non-existent objects in the noise (Nguyen et al., 2015).

Another argument is that although machine learning often finds a good solution, the decision-making process is usually very difficult to understand (Ching et al., 2018). Machine learning can deliver surprisingly good final results in decision-making questions, but it often cannot explain in humanly understandable language why this decision was made. However, it was important to me to be able to understand all the analyzes in as much detail as possible in order to understand as much as possible about the biological background. It was also important to me to understand which results are based on measurement errors or systemic errors and which results are actually due to a biological effect. I learned a lot in the process and was able to evaluate the data in great detail and examine it from various points of view, which only emerged through dealing with the evaluation algorithm. In this sense, the way to the result is often more helpful than the result itself.

7.2 Data quality and biological variability

A major issue in automated data analysis is the assessment of the data quality and the detection and quantification of noise. Experienced lab scientists can easily detect artifacts in the data. In contrast to human analysts, machines have trouble with distinguishing between the original biological data and data which are biased by artifacts and the data acquisition equipment. There are several ways to deal with this problem. The obvious way is to take efforts in improving the data quality and assure that only high quality data is delivered to the analysis process. But for various reasons one has to cope with medium or low quality data: technical and monetary restrictions, lack of time, already existing data from former experiments and so on. Therefore it is crucial to check the data quality before analyzing it.

In the best case scenario, the quality check is done by the analysis software itself. The response to the quality check can be performed in two ways: either the software rejects bad data or it tries to correct the data. For sure, the easiest way is to reject bad data, however, sometimes one also wants to analyze the bad data as far as possible accepting a lower degree of accuracy. Therefore, a fair compromise is, to measure and print the quality of the data but also print the corrections which were applied to the data.

7.3 Analysis of calcium signatures in plants

The aim of this work was to answer the question whether information about the stimulus can be found in the calcium signal with which plants respond to stress. A follow-up question was whether the calcium signal acts as an information carrier that encodes the information about the stimulus into a calcium wave that propagates through the plant and is decoded at the recipient sites in order to trigger stimulus-specific reactions. In short: is there information in the calcium wave and if so, does the plant use it? As expected, the questions could not be answered with absolute certainty. Nevertheless, the answer to the first question is a sound yes, and in my opinion the answer to the second question is rather a no. I will explain this in a little more detail now.

First, with the automated image evaluation and the various display options of the calcium wave as a kymograph, surface plot and crestline plot, there is the ability not only to present this calcium wave in a visually concise manner but also to track it quantitatively and to compare different experiments with one another. The unbiased observer can already see from the individual graphical representations that there is quite a difference. There is a big difference between the stimulation with bacterial peptides or cell wall components of fungi and the stimulation with high salt, or in general: between the stimulation with biotic and abiotic stimuli.

While with the biotic stimuli the course of the wave from the starting point is quite clearly recognizable in many cases, the wave in response to the stimulation with salt is a mystery: the reaction to salt starts immediately with the stimulation, but is only extremely short, and one can see a similar reaction immediately after the stimulus is withdrawn. Because the reaction to salt is so fast and short, further evaluation of the image data does not lead any further. The image data are not even clear enough to claim that the calcium is moving in the form of a wave. However, there is literature showing the occurrence of a calcium wave in response to stimulation with salt (Choi et al., 2014). The key point here is that this wave moves through the plant at an extremely high speed of around 400 µm/s, which can even be almost doubled by overexpression of vacuolar calcium channels. This high speed could explain why the wave can only be partially captured with our experimental setup and the sampling rate of our microscope camera, which is not designed for these speeds.

However, observing a high-speed wave raises new questions: first, what kind of system can the plant use to achieve such a speed at the molecular level, and second, if there are different systems for generating different waves: how do they differ and how and why is one activated and not the other? These observations and considerations have led to a rough classification of the calcium signaling in response to stress into two types of waves: a slow local wave in response to biotic stimuli and a fast global wave in response to abiotic stimuli. I went for a more accurate characterization of the local wave using the experimental data from my collaboration partner in order to identify further stimulus-specific properties. For the global wave, there have already been detailed studies in the literature. In particular, the hypothesis was made that this wave cannot be explained by calcium-induced calcium release alone, but that a combined ROS-calcium wave would be a possible explanation (Evans et al., 2016). I resumed this model and expanded it. Then I checked if this model could also be brought into accordance with the local wave I had extensively investigated.

7.4 Different stimuli provoke different plant responses

One aim of this work was to find out whether and if so how the plant encodes information about the stimulus in a calcium wave. Such a hypothesis is not entirely fallacious. It is known that calcium pulses accomplish such an effect in the nervous system of animals. However, the nervous system is also specially optimized for this function: From a functional point of view, neurons are long cables that are designed for the rapid transmission of information from a specific transmitter to a specific receiver. The structure of the neuron ensures that the information is not lost on the way and that it arrives at exactly the right recipient. Plants, on the other hand, do not have a nervous system. There is also a compartmentalization and various channel systems that supply the different parts of the plant with water and nutrients, but essentially all parts of the plant are connected to one another. The lack of separate information channels leads to the hypothesis that the information must be encoded in the signal itself. And since a pulsed signal can carry information per se and calcium signals occur in pulses or waves, the question is: is the calcium signal such an information carrier? To find out, *Arabidopsis* plants equipped with built-in calcium sensors were stimulated with different stimuli.

What you see at first glance when looking at the kymograph is striking: the response to salt is completely different from the response to flg22 or chitin. The calcium signal immediately follows the stimulation with high intensity and vanishes completely after just a few seconds. Interestingly, a similar signal appears with a slightly reduced intensity directly after removal of the stimulus. This detail is suspicious and raises the reasonable question of whether there is actually a calcium wave in the sense of a biological signal or just a purely physical or electrochemical reaction, which can be traced back to a change in turgor pressure as a result of a changed concentration gradient, for example. This consideration is also supported by the shortness of the calcium response and the fact that the signal occurs simultaneously at all points of the root as far as they are in the visual range of the microscope.

Another point is that after the signal disappears, almost no further reactions can be observed, although the stimulus is still fully present. Only when the stimulus is removed the calcium signal reappears. So if you only look at the first few millimeters of the root and compare it with the reactions to the other stimuli, there is initially much pointing to an artifact or a physical or chemical reaction. Nevertheless, there is a notable reaction in any case. Moreover, from the literature it is known that a calcium signal is actually triggered that runs through the plant at very high speed and can be perceived in more distant parts of the plant (Choi et al., 2014). This excludes that it is an artifact. However, how the calcium signal is generated at the molecular level and how it can propagate at this high speed remains unclear. Due to the frame rate limitations of the microscope camera, it is not possible to examine the calcium signal in more detail and to make further conclusions from the experimental data. I therefore focused on simulating the propagation of this fast wave in a model (see chapter 5.3).

The outcome of the simulation of a fast calcium wave suggests that additional components are involved in the signal propagation, even if their role is still unclear. The observation that the calcium wave is suppressed by adding calcium channel blockers, but a change in the concentration of specific stress markers can still be observed in the distant parts of the plant, supports this assumption (Choi et al., 2014). The role of calcium in this scenario is unclear as well. The plant might react to salt stress on several levels and with several messenger agents, one of which is calcium. It can also be assumed that these different agents are related

to one another and support or reinforce one another. Exactly which substances are involved and how the connection to the calcium signal is, remains a task for future research.

In the stimulation experiments with biotic stimuli the plant roots were systematically exposed to the bacterial peptide flg22, the component of the fungal cell wall chitin and a purified form of chitin, C8. Chitin, chemical formula $(C_8H_{13}O_5N)_n$, is a mixture of polysaccharides that consist of a chain with different numbers of N-acetylglucosamine units. C8 is a synthetic variant of this molecule, which consists of exactly 8 monosaccharide units. With the stimulation with flg22 an attack by bacteria, with chitin or C8 an attack by fungi should be imitated. The basic idea here was to see whether the plant can distinguish between these two different attackers and whether this information is also reflected in the calcium signal.

My intention was to expand the automatic analysis of the calcium response to include a classification of the analysis data in order to draw conclusions about the molecular processes of the stress response based on stimulus-specific parameters. Because chitin and C8 have similar chemical properties and it is to be expected that that there is less variation in the results for C8 due to the uniform molecular structure, most of the evaluations in the following refer only to C8. If there are noticeable differences between chitin and C8, I will explicitly mention this.

The analysis results of the automated evaluation of biotic stimulation show a lot of properties in common when comparing the results of flg22 and C8 (Figure 16). The starting time and position are in a similar range and the speeds of the wave in both directions are also comparable. Taking into account the systemic variation of the different experiments, no significant difference can be determined. At least one can conclude that these two stimuli trigger similar processes at the level of the calcium signal. If you look at the kymographs and crestline plots of the experiments with the bare eye, the results seem to be quite different. However, the differences are not that easy to put into words or mathematical formulas. It's a bit like looking at different people's faces. You can tell immediately that they are different, but clearly describing the difference is not that easy. It is reasonable that different molecular compositions trigger different molecular reactions at the very first level of stimulus detection. The question is whether this is still clearly recognizable in the calcium signaling or whether the differences there are no longer obvious. In other words, are the differences big enough to maintain a stimulus-specific reaction from the plant? For now I do not have a final answer to this question. It might be that the parameters I examined with regard to the calcium wave are not sufficient for assessing the triggering stimuli. Perhaps there are other connections that cannot be captured with the existing analysis methods. For example, different stimuli could affect different cell types. The current evaluation averages the calcium concentration across all cells at a specific position along the root. A machine learning based approach for example could reveal further differences, but a larger number of experimental test data is necessary for a meaningful use of machine learning.

The variation of the results between individual test series of the same stimulus is very high. Therefore it is questionable whether the recipient cells of the calcium signal are competent for stimulus-specific reactions. It might be that the cells through which the wave runs simply react with a universal non-specific defense response. I cannot finally disprove this hypothesis with the results presented here. However, it is known that calcium signaling within the individual cell often consists of very short pulses in series and can show very different shapes and intervals (Figure 30). With the current setup it was not possible to accomplish the required high resolution of the signal at the single cell level. In my analysis

I averaged the concentration across several cells. It is possible that the stimulus-specific information is hidden here.

The fact that the calcium signal is generated by a large number of single calcium channels and pumps, which are basically able to generate different wave forms of the signal, enables the possibility that the information is definitely contained in the signal. It might be that it can be deciphered using an analysis with a higher spatial and temporal resolution. Still, there is potential for further investigations and analyzes.

7.5 Modeling calcium-induced calcium release

The starting point for my investigations was the paper by Evans et al., who came to the conclusion that the high speed of the response to salt cannot be explained by pure CICR (Evans et al., 2016). The model calculations showed that an additional faster element is required: ROS. From the experimental data of stimulation with flg22 and chitin/C8 the question arose: if CICR is not sufficient for the calcium wave in response to the stimulation by salt, maybe this slower form of propagation is sufficient for supporting the slower local wave in response to biotic stimuli? My motivation was, to set up a CICR model according to Evans et al., reproduce its results and then apply it to the experimental data. Therefore, The first step was to create a model of calcium-induced calcium release and use it for measuring the propagation speed of a calcium wave.

I will start with a few basic thoughts about the propagation of a wave: To put it simply, any particle that does not move in a vacuum requires energy to keep moving. This applies not only to physically moving particles but also to information that is encoded in these particles or coupled to these particles in some form, i.e. also for a wave. The contact with the environment causes frictional losses or other disturbances. Thereby the movement is inhibited and the information is lost. The movement and the propagation of the information must therefore be ensured by means of active use of amplifier elements or, in physical terms, by supplying energy. This applies to technical systems such as the internet or cell phone communication as well as to biological systems. Specificially, a wave based on an increased intracellular calcium concentration must be actively supported.

Due to the physical properties of the calcium ion and the molecular properties of the cytosol, it is quite clear that pure diffusion is insufficient: too slow and too weak. A common model of calcium propagation is therefore the so-called fire-diffuse-fire model of calcium-induced calcium release. It is based on the fact that calcium-dependent calcium channels pass the signal on from point to point by reinforcing an increased calcium concentration through repeated release of calcium thereby preventing the calcium level from dropping to the base level. Basically, this is a biological variant of the well-known domino effect, in which a chain reaction of falling dominoes is set in motion when the first domino is hit. While in dominoes the distance between two elements is bridged by the mechanical tilting movement of one domino, in CICR this is done through the diffusion of calcium ions. The path of propagation is determined by the position of the calcium channels, the speed by the diffusion coefficient of calcium, the distance between two adjacent channels, the trigger threshold of the calcium channel and the amount of calcium ions emitted. One can already see here that the knowledge of several parameters is necessary for correct parameterization of the model. While the diffusion coefficient of calcium in the cytosol and the distance between

two vacuolar TPC1 channels can be determined quite well experimentally, it becomes difficult with respect to the other parameters. These parameters can only be estimated.

This is where modeling comes in. Model simulations can be run assuming different parameter values. It is a specific strength of modeling, that one can try out different assumptions and compare the simulation results to the experimental results. Since increasing the amount of calcium ions emitted in a single opening event of a single channel, here referred to as release strength, has an effect similar to lowering the trigger threshold, I set the release strength to a fixed value. Different molecular constellations could then be simulated by changing the trigger threshold. In theory, by lowering the trigger threshold, the speed of the wave can be increased to the intended value.

Therefore, I chose the trigger threshold in the model appropriately to hit the speed values reported by Choi et al. of around 400 µm/s. But if I used this model for simulating the wave in a TPC1 overexpressor mutant, in which the channel spacing between two adjacent TPC1 channels on the vacuolar membrane is reduced from 1 µm to 0.6 µm, I could only get a speed of 530 µm/s instead of the experimentally observed 700 µm/s. Just like Evans et al. I came to the conclusion that CICR cannot be responsible for the observed effects, at least not alone.

Since the experiments with biotic stimuli revealed much slower speeds in the range of 5 µm/s, I wanted to see whether simulation of pure CICR might be suitable for this wave propagation. However, the speed values resulting from this simulation were still too high given this parameterization, even taking into account the shortened cell sizes in the root tip and the associated longer running time due to the larger number of "slow travel" gaps between the cells. Therefore I revised the assumptions of the model, especially the assumption that the diffusion between two cells can occur completely unhindered through the plasmodesmata. These reflections and results are discussed in the following sections.

The simple model of CICR as well as the ROS-assisted model is based on the calcium release through the channel TPC1 located in the vacuolar membrane. Although it is a well-founded fact that the opening incident of this channel depends on the cytosolic calcium concentration, it is unclear whether this channel actually releases calcium from the vacuole into the cytosol (Hedrich and Neher, 1987; Hedrich et al., 2018). However, it is proved that the number of TPC1 channels present on the membrane surface has an influence on the speed of the calcium wave: it is slower in the TPC1 knockout mutant, and faster in the TPC1 overexpressor mutant than in the wild type (Choi et al., 2014). This makes a proper classification of the TPC1 channel so difficult: the wave apparently also runs without TPC1, but TPC1 definitely influences its speed. So what role does the ion channel TPC1 actually play?

One common hypothesis claims: TPC1 is the only carrier of the calcium wave by means of CICR. The calcium wave observed in the TPC1 knockout mutant might be an artifact or a substitute reaction of the mutant. An argument against this hypothesis is the fact, that my model equivalent to the model of Evans et al. cannot sufficiently reproduce the observed speeds. In addition, such speeds could only be achieved if either the calcium output of the single TPC1 channel, the release strength, was set very high or the trigger threshold was set very low. A very low trigger threshold does not make sense from a biological point of view, since even a tiny increase in the calcium concentration would trigger the wave and the response system of the plant would react very sensitively. A very large outflux of calcium ions per opening event is also very unlikely, especially since the TPC1 channel is a slowly

opening channel, which I did not take into account in my model for optimizing the speed of the wave. However, it is conceivable that the slow wave observed in the experiments with biotic stimuli is based on pure CICR. It is also conceivable that another element is involved in the calcium wave and the TPC1 channel is only used to fine-tune the wave. I will outline this aspect in more detail when discussing the ROS-assisted model (see Section 7.8).

7.6 Modeling approaches

My mathematical simulation of the calcium wave using the fire-diffuse-fire model is based just like the model by Evans et al. on the diffusion equation. For the primary model, which I developed together with the master's student Jonas Löffler, I first chose a numerical approach using the finite difference method for the solution of the partial differential equation. When developing and parameterizing a model it is advantageous if the calculations do not take much time. With the finite difference method we had a method at hand with which we could control the accuracy of the calculation and thus the computing time. We also used this approach for the extended model involving ROS-assisted CICR.

An advantage of this approach was that the calcium release of a single channel could be simulated as a rectangular area of a fixed calcium concentration, graphically representing a calcium microdomain. This method in turn also had disadvantages, as we found out in the further development of the model. Firstly, the rectangular calcium release had to be in line with the spatial resolution of our model. Secondly, there were difficulties of modeling very small cells around 5 µm in size, in which the vacuole due to numeric limitations houses only one or two TPC1 channels. As a workaround, we reduced the cell wall thickness and thus increased the vacuole so that the calcium release could still be properly calculated by the algorithm. It was also a coding-related challenge in the extended model to place the ROS-producing proteins and ROS-sensitive calcium channels regularly, since the relative position of the individual channels is very important in this model. For the calculations in my thesis, I later switched this approach to the fundamental solution of the diffusion equation, in which calcium release is modeled as an exact point source.

7.7 Velocity calculation and channel positioning

For quantitatively comparing the model simulation with the values observed in the literature, we had to calculate the mean propagation speed of the calcium wave. However, since the speed of the wave changes regularly as it travels through cells of different cell sizes, we had to define the calculation algorithm of the average speed. Since it is a diffusion-based wave with a continuous range of values, we also had to define a minimum concentration for calcium which we considered the "wave arrived" concentration. We solved these challenges as follows: We defined the threshold value at which a channel is triggered for opening as the "wave arrived" concentration. Then we could conveniently use the opening time point of a channel for calculating the wave speed. Hence, to calculate the average speed, we used the position and the opening time of the channel that was opened first after a fixed time period of 2 seconds, and calculated the speed as the ratio of position and time. This value corresponds to the speed value of a constant wave that would need this time to reach this channel.

Another mathematical issue was the positioning of the channels at fixed intervals, especially with regard to the position of the first and last channel of a cell. Ideally, the distances between all channels are constant and the last channel is at the very end of the vacuole while the first channel of the next cell is at the very beginning of the next cell. However, the ideal case can only be applied if the cell size is a common multiple of the vacuole spacing and the channel spacing or, to put it simply, if the cell is in line with the same grid as the channels. But this is not the case for variable cell sizes. I solved the problem in such a way that I first rounded the cell sizes in the model to whole micrometers. As a result, there were no problems at least in the wild type with its 1 µm channel grid. For the TPC1 overexpressor, I simply placed an additional channel at the very end of the vacuole, in case there wasn't one there. The additional channel then had a reduced distance of 0.2 µm or 0.4 µm to the next channel instead of the regular 0.6 µm, but the effect of this additional channel on the speed should be minimal. In any case it would not lead to a reduction of the speed but rather to an increase.

7.8 Modeling ROS-assisted calcium-induced calcium release

With the model that I created together with the master's student Jonas Löffler, we could reproduce the results of Evans et al. and understand that the experimentally observed speeds cannot be achieved with pure CICR. Therefore, like Evans we expanded our model to include ROS-assistance. The difficulty was to parameterize the newly added channels so that the wave runs faster. Essentially, that would be quite easy if the speed would be determined only by the ROS-producing proteins and ROS-sensitive calcium channels and the TPC1 channels would play no role at all. This is because the diffusion coefficient of ROS with around 1000 $\mu m^2/s$ is quite high. The challenge was to parameterize the model in such a way that the speed additionally depends on the TPC1 channel density. In other words, the ROS-based wave has to amplify the pure CICR wave in some way so that the wave runs faster overall than without ROS-assistance. There are basically two possibilities for this: either the ROS proteins and channels simply amplify the local calcium concentration generated by the TPC1 channels thereby triggering the TPC1 channels earlier than without ROS. Or the ROS-based wave generates a high calcium concentration at a point where the TPC1-controlled calcium wave has not yet arrived, and thus ensures that the ROS-supported wave is "leading", meaning is ahead of the pure TPC1-based wave.

A closer look reveals that these two possibilities cannot be separated from each other: If, as in our model, one assumes an even distribution of channels and a quite high density of calcium-sensitive ROS channels, then that means that the opening of a ROS channel coercively triggers the closest ROS-sensitive calcium channel first. The calcium release of this channel in turn increases the calcium concentration at this position, which is already quite high because it has caused the ROS channel to open. A "leading" ROS-driven wave would only be obtained if ROS-producing proteins and ROS-sensitive channels were placed alternately and a kind of "zigzag" wave could be generated. The model scheme in figure 6 of the publication of Evans et al. depicting an alternating sequence of channels suggests such a wave (Evans et al., 2016). However, on a two-dimensional surface such as the plasma membrane it is more likely that the different channel types are rather randomly or evenly distributed. In our model with a one-dimensional path and a ratio of ROS-producing proteins to ROS-sensitive calcium channels of 5:1, this means that in exactly the same position as a ROS-producing protein there is also a ROS-sensitive calcium channel. This will also be

the first to trigger after the ROS "channel" has opened and thus increase the intracellular calcium concentration at exactly this position.

The situation is different at the transition from cell to cell: At this point it is possible that an increase in the calcium concentration does not significantly speed up the propagation of the wave due to the lack of calcium channels. Here the calcium wave is accelerated by the extracellular ROS wave rushing ahead. The extracellular ROS wave is responsible for the rapid opening of the first TPC1 channel of the next cell. In a nutshell: there is an increase in the local calcium concentration solely due to the presence of the ROS-producing proteins and the ROS-sensitive calcium channels. However, at the cell boundaries the high diffusion coefficient of ROS might lead to a speed advantage compared to the diffusion of calcium only.

With the addition of two other channel types, additional parameters were added with which the wave simulation can be tuned: these are the release strength and trigger threshold of the two additional channel types and also the relative positioning of the channels to one another. Since the aim of this extended ROS model was simply to increase the wave speed, I essentially looked at the ROS assistance from the perspective of the amplification effect on the individual calcium channel. From this point of view, the effect of additional ROS support is simply an overall increased calcium concentration in the cytosol, so that the concentration level necessary for triggering the closest TPC1 channel is reached earlier. In this scenario, the TPC1 channels would still control the speed of the wave. The ROS assistance would be included in the speed regulation as a boost factor. The easiest way is, to apply this approach to the original pure CICR model setup, with a wave speed in the TPC1 wild type of around 440 µm/s and in the TPC1 overexpressor of only around 526 µm/s. Basically, this means that I will boost the wild type with a factor of 1 (equivalent to: not at all), but the TPC1 overexpressor with a factor of 1.3. In any case, the amplification in the case of the overexpressor must be greater than that of the wild type. With the least amount of effort, this can be achieved in this way that the calcium concentration required to activate the ROS channel is only reached in the TPC1 overexpressor. The additional ROS components work like a kind of a switchable booster, which is activated above a certain calcium concentration, thereby further increasing the concentration of calcium. With this in mind, I parameterized the extended model of ROS-assisted CICR and thus achieved the observed propagation speeds in my simulation runs.

One aspect that should also be mentioned is the model assumption that ROS-producing proteins and TPC1 channels are located on the same spatial axis. In fact, however, the ROS proteins are located in the plasma membrane and the TPC1 channels in the vacuolar membrane, so they are at least 10 µm apart from each other (I estimated this value by measuring microscopy images of plant cells). This a multiple of the distance between two adjacent TPC1 channels. The calcium signal has to cover this distance by means of diffusion, which also takes time. To take this into account in the model, the channels would have to be re-parameterized in order to achieve the observed high speed of the wave. The large distance between the ROS-producing protein and the TPC1 channel could be compensated for by a lower calcium threshold for activation of the ROS-producing protein. The great distance between the ROS-sensitive calcium channels, which are also located in the plasma membrane, and the TPC1 channels could be compensated for by a higher outflux of calcium ions per release event compared to the TPC1 channels.

Finally, it is questionable whether the processes in the cell actually take place in the way

as proposed by the ROS-assisted model. The basic problem here is the following: on the one hand, a purely TPC1-supported calcium diffusion system is much too slow, on the other hand, the TPC1 channels influence the speed. Basically, this dilemma can only be solved by assuming a calcium concentration boost e.g. through ROS. Of course, there are still many unanswered questions here, but the ROS hypothesis offers at least one possible solution.

At the end of this chapter, I would like to make a very fundamental consideration: The discovery that calcium is able to accept innumerable waveforms and to encode information in these waveforms, and the observation that calcium moves in waves through the organism, leads to the conclusion that calcium picks up this information from the sensor and transmits it to the recipient. But this does not necessarily have to be the case and it can lead to a wrong path. The problem that the observed speed of the calcium wave cannot be reproduced in the pure CICR model raises doubts. It is possible to achieve this speed with the help of a further - faster - component. But then, as a consequence, the information would also have to be transmitted when the two components interact. That seems unlikely. Rather, I think that calcium is not the carrier of information across cell boundaries, but that calcium is the interpreter of the stimulus after the stress response. All different stimuli converge in the calcium signal and are translated into one global signal. This signal then triggers an appropriate reaction at the cellular level. This hypothesis could also explain the different kymographs of the experiments investigated in this work with different stimuli.

7.9 Modeling slow local waves based on CICR

The model of pure CICR that I investigated together with the master's student Jonas Löffler according to the publication by Evans et al. was mainly considered under the aspect of whether it can achieve the observed high wave speeds after stimulation with salt of around 400 µm/s for the *Arabidopsis* wild type and around 700 µm/s for the TPC1 overexpressor *oxTPC1* (Choi et al., 2014; Evans et al., 2016). That was not the case. Now the question arose whether the model of pure CICR could be suitable for the slow local wave observed as a response to biotic stimuli.

Therefore, I parameterized the model by increasing the TPC1 threshold value in such a way that the speed of propagation was roughly in the targeted range. The TPC1 Overexpressor *oxTPC1* was not taken into account here, since the experimental data of my collaboration partner were generated only with the wild type. Since the speed of the local wave with a maximum of 10 µm/s is considerably lower than the approximately 400 µm/s, I had to increase the trigger threshold of the TPC1 channel by a few orders of magnitude. Interestingly enough, this had as a consequence that the wave could no longer be started with the targeted opening of one single channel, the amount of calcium release was too weak for that. In order to generate a propagating calcium wave, I had to trigger at least 10 adjacent channels at the same time. The result of the simulation run comes very close to the kymograph created from experimental data, and the speed of propagation is in a similar range (Figure 19C; compare e.g. with Figure 15A).

Another factor that slows down the speed of the wave could be found in the cell-cell transitions. In the model use here it was assumed that the plasmodesmata do not constitute any additional hurdle for diffusion except that the channel spacing is increased. But if this is the case, as I demonstrated in my simulation of diffusion using a cellular automaton (see Section 5.6), then this might further reduce the speed of propagation. Interestingly, the gaps

in the cell-cell transitions, which can be clearly seen in the simulation (Figure 19), cannot be seen in the experimental data by visual inspection. This could be related, for example, to the fact that the wave actually spreads in several parallel cells and not just in a single chain of cells lined up as in the simulation. Microscopic images with a higher resolution could also provide better insights here. Furthermore, the removal of the increased calcium level from the cytosol by means of calcium pumps was not taken into account in this model. This could also play a role in the time scale of the local wave and possibly be responsible for the fading of the local wave, that finally leads to the limitation of the wave to a local area.

Despite the fact that not all physiological factors could be taken into account in this model, the model shows a fairly clear agreement with the experimental data, so that one can assume that the slow local wave in response to stimulation with biotic stimuli is actually based on pure calcium-induced calcium release through TPC1 channels.

If we act on the hypothesis of two independent waves, a slow, purely CICR-based one and a fast ROS-assisted one, then the question still arises, how do the waves differ with respect to the molecular conditions? Or to put it another way: why isn't every wave ROS-assisted? For my simulations of a purely CICR-based and a ROS-assisted wave, I set the threshold of the TPC1 channels differently, but a change in sensitivity is not feasible in reality. Of course, it could be that the different waves run in different cells. An additional component that influences the speed of the wave may also play a role here. In any case, there are still many unanswered questions on this topic. Further experiments - in vivo or in silico - are required to answer them.

7.10 Simulating calcium dynamics using a cellular automaton

The mathematical model described in the previous sections, which was used to calculate the propagation speed of the calcium wave, is based on the diffusion along a one-dimensional path. One assumption here was that the diffusion across the cell boundary is not hindered by the cell wall and the plasmodesmata. In this model, there was a delay of the wave when passing through the plasmodesmata, only because the channel spacing between two adjacent channels was greater at the cell-cell transition than within the cell. That seemed plausible to me for a one-dimensional environment in which the diffusing particles can only move to the right or to the left from their place of origin, but not for a two- or multi-dimensional environment. So I wanted to check qualitatively how a constriction like the plasmodesmata affects the diffusion.

The simulation with a two-dimensional cellular automaton model provided a promising setup for this because it gave a visual impression of the processes in the cell. The movement of individual particles on a two-dimensional grid of cells was simulated using very simple rules. In each time step, each particle moved a distance of one cell. It was randomly chosen in which of the adjacent cells each individual particle moved. In this model, the cell walls and plasmodesmata were represented as lines drawn into the grid with small gaps. The advantage of such a simulation is that one can visualize the movement of calcium ions in a solution that collide with large molecules as they travel through the cytosol and thereby change their directions of movement. Of course, the results of such a simulation are mainly of a qualitative nature, since it is not possible to determine the real movement profile of an individual calcium ion experimentally and one can only estimate movement parameters. Nevertheless, my model

could also be evaluated quantitatively. I could calculate the concentration of calcium ions under different conditions at certain positions and compare them with one another.

To find out whether cell walls and plasmodesmata are an obstacle to diffusion, I ran simulations with and without cell walls. At first glance, when comparing the results with and without a cell wall, I saw that only a few particles made it through the cell wall in the simulation time, while the particles in the scenario without a cell wall were distributed almost evenly over the simulation area. This is not surprising, because the directions of movement of the particles close to the cell wall were severely restricted, except at a few positions where the plasmodesmata were located. In contrast to the model assumptions in the one-dimensional CICR model, it can be hypothesized that the plasmodesmata represent a considerable obstacle to diffusion and thus significantly reduce the propagation speed of the wave.

When talking about plasmodesmata and permeability in literature, most publications mention that plasmodesmata are impermeable to large molecules but permeable to small molecules and ions (Sager and Lee, 2018). In most cases, however, the issue of how quickly small molecules can get through the plasmadomesmata is neglected. If one considers the total size of the plasmodesmata in relation to the size of the cell wall, then it becomes intuitively clear that the cells can exchange small molecules through them, but they are not particularly suitable for rapid exchange.

If one wants to determine the influence of the plasmodesmata on the diffusion of calcium in the cytosol more precisely and more quantitatively, it would be necessary to carry out further experiments. The measurement of the passive particle flux through the plasmodesmata is also made more difficult by the fact that plasmodesmata are apparently very dynamic structures in terms of opening width. On the one hand, plasmodesmata can almost completely close the opening, on the other hand it is known that they can open so wide that even large molecules such as RNA or viral RNA-virus complexes can fit through (Niehl and Heinlein, 2011). In any case, the results of my simulation support the hypothesis that a high speed of a calcium wave cannot be achieved with pure symplastic CICR. In contrast, the issue of diffusion inhibition by plasmodesmata does not exist with the extended model of a ROS-assisted CICR, since the cell wall barrier is overcome with the help of extracellular ROS.

7.11 Differential regulation of CPK proteins

As an example of a stress response downstream of calcium signaling, I chose the CPK-mediated regulation of the stomata by means of CPK21 and CPK23 (Geiger et al., 2010). CPK proteins respond to the binding of calcium ions with increased phosphorylation activity. In the guard cells of the stomata, the activation of the CPK proteins initiates the closure of the pore (Li et al., 1998; Valmonte et al., 2014). I was able to show that CPK21 and CPK23 reveal a different activation curve with respect to calcium. Slight differences in the amino acid sequence of CPKs lead to a slightly different sensitivity for calcium and different levels of activation.

The fact that the proteins CPK21 and CPK23 show different calcium dependencies can already be concluded from the experimental steady state data. Both proteins reveal four binding sites for calcium with an EF hand motif. However, one EF hand of CPK23 slightly

differs from the common EF hand sequence (Q at position 12 instead of E). This could be an explanation for the weak sensitivity to calcium.

Calcium-binding proteins are known to show positive cooperativity, therefore I fitted the experimental data to a Hill function. For CPK23, the Hill coefficient was less than 1, so there is more of a linear dependence on calcium. For CPK21, there was initially a very high Hill coefficient without applying a limit for the fitted parameter. This is due to the fact that the experimental data show a very steep increase in activity when the calcium concentration is increased from 200 nM to 500 nM, and the activity then drops again at higher calcium concentrations which is very abnormal and unexpected. Taking the well-studied activity curves of other enzymes as a reference, it can be assumed that these effects are due to deficiencies in the measurement setup. Such data cannot be properly fit with a sigmoidal function like the Hill function, since the value of a sigmoidal function is always monotonically increasing. In order to compensate for these effects, I limited the parameter range for fitting the Hill coefficient to 4, since in a protein with four binding sites the cooperativity value can reasonably be a maximum of 4.

Assuming cooperativity of calcium binding, the activity curve for CPK21 makes sense. The question arises, why CPK23 has only a weak calcium dependence with at least three functional binding sites. It might be possible that only the two N-terminal calcium binding sites are decisive for the activation of the protein, whereas the C-terminal binding sites are not. Christodoulou et al. showed in a study on CPK1 that the C- and N-terminal calcium binding sites have different roles in the activation of the CPK protein (Christodoulou et al., 2004). According to their findings, the C-terminal EF hands have a very high affinity and bind calcium already at physiological calcium concentrations around 100 nM maximum. The CPK protein nevertheless remains almost inactive, since the autoinhibitor sequence contained in the J domain acts as a pseudosubstrate binding to the kinase domain. This conformation is also maintained when calcium binds to the C-terminal binding sites. Only when the calcium concentration increases and calcium also binds to the N-terminal EF hands a conformational change of the calmodulin-like domain occurs and the autoinhibitor detaches from the kinase thus activating the CPK protein. From this it can be concluded, that only the two N-terminal binding sites, i.e. EF hand 1 and 2, are relevant for the activation of CPK proteins. Studies on mutants of CPK21 reveal a similar result, in which the inactivation of the N-terminal EF hands by point-mutations completely inhibits the protein activity, while after inactivation of the C-terminal EF hands the protein still shows residual activity (Franz et al., 2011).

These findings could explain the weak calcium sensitivity of CPK23, assuming that only one of the relevant binding sites is functional. However, the hypothesis does not match the strong calcium dependence on CPK21 that we see in the experimental data. In particular, the sigmoidal increase in activity with increasing calcium concentrations indicates a positive cooperativity of all four binding sites. Obviously, additional parameters are involved here. Perhaps there are differences within the CPK proteins with regard to the affinity of the calcium binding sites or the mode of activation. It would be helpful to obtain more experimental data, in order to make sure that the assumptions are not based on inadequate or incorrect measurements.

The response curve of CPK21 to increasing concentrations of calcium demonstrates that CPK proteins can react very sensitively. The experiments are based on steady state data, there is little knowledge about the protein kinetics. In order to simulate the effects of calcium signaling on the activity of the CPK proteins under dynamic conditions, I used

experimental data of calcium time series as an input for my CPK model and analyzed the phosphorylation activity. The experimental calcium data comprises only a few short pulses. Using a Hill function based CPK model under the assumption of an instantaneous protein response, there was an increase in activity for CPK21, while the activity of CPK23 remained almost unchanged. The activity increase for CPK21 was more pronounced in guard cells than in epidermal cells, which is related to the corresponding different calcium signals that define the different cell types in my simulation. This result could be expected, since the increased activity and the associated closure of the stomata is a crucial function of the guard cells within the stress response of the plant.

The reaction speed, i.e. the speed of calcium binding, plays an important role in the activation of CPK proteins. It can be assumed that the maximum phosphorylation activity is only achieved if all four binding sites are occupied. This assumption was also supported by the experiments of Christodoulou et al. (2004). I took this into account in my model by weighting the fully occupied protein with 1 for the relative phosphorylation activity. This means that the time until all four binding sites are occupied cannot not be ignored. Therefore, I ran simulations of my model using different speed factors which represented the multiplier of the binding and unbinding rates of calcium to the binding sites. The simulation revealed that the speed factor must be quite high in order to achieve a full occupancy of the binding sites if the input signal consists of several short pulses. Using slower reaction rates, the calcium pulse has passed before all binding sites could be occupied. This finding is very important with regard to the differential regulation of the CPK protein: small differences in the binding properties can lead to one protein being activated and the other not being activated at a given calcium signal. Hence, the reaction kinetics is very important. This result is an example for the power of modeling. Experimentally obtained data can be fed into a computer-based model running simulations under different conditions, from which various hypotheses can be derived. However, in order to verify or falsify them, further laboratory experiments and data are necessary.

7.12 Concluding remarks

The aim of this work was to analyze calcium signatures of stimulation experiments in plants following the hypothesis that the type of stimulus is encoded in the calcium wave and can be decoded by the plant. The very first idea was to simulate the calcium wave using a cellular automaton and evaluate the simulation data using an information-theoretical analysis. In the next step, a biochemical model with as many molecular details as possible should be created. Finally, it was the hope of being able to answer the question of whether plants make decisions in response to stress stimulation centrally or decentrally.
I used a typical kymograph (see Figure 4A) as a sample for my work. First I binarized this kymograph, i.e. converted it into a black and white image based on a threshold value for the intensity (Figure 17A). I tried to recreate this binarized kymograph using a cellular automaton. The first simulation runs simply showed two thick straight lines, a result that does not necessarily require the skills of a cellular automaton (emergence, complex pattern formation from simple rules). Even the introduction of a stochastic component did not lead to the desired approximation of the simulation results to the experimental data, but essentially only added noise to the simulation data. So I decided to go back a step and reprogram the generation of the kymograph from the raw data, which turned out to be a challenging task.

The computer-based analysis of the experimental data resulted in an R script for the automatic evaluation of the raw data that, in addition to an improved kymograph, outputs two helpful plots: On the one hand, the surface plot, i.e. a quasi 3D plot of the kymograph, which gives a good impression of the actual proportions of the calcium concentrations. And on the other hand, the so-called crestline plot, which condenses the calcium wave into a clearly recognizable line, that can be easily measured and evaluated automatically. Furthermore, I was able to reproduce two kymographs from a publication (figure 6C and 6D of Keinath et al., 2015). Since I did not have the raw data available, I recalculated the data using reverse engineering of pseudo raw data from heatmap videos, which were accessible for automated analysis.

My next step was to use the improved kymograph as a basis for modeling with a cellular automaton. I selected a kymograph, which provided a relatively clear view (little noise, no artifacts) and basically consisted of a hill-shaped curved line with different slopes in the direction of the tip and of the shoot. The challenge was, to create a model that can reproduce the characteristic shape of the kymograph. In order to achieve a realistic simulation result, I had to apply a variety of complicated rules. Some of these rules required a kind of memory of the individual cells, at least if all cells were to have identical properties from the start. The hill-like shape in the kymograph and crestline plot arises from the fact that the wave propagates faster at the beginning and then weakens, but generally spreads faster in the direction of the tip than in the direction of the shoot. In order to form this hill, the cells had to somehow "know" there position relative to the hill. In other words, they had to know how many cells the wave had passed through before. This, in turn, was only possible if the cells counted by remembering the number of involved precursors and adding one to it, and passed this information on from cell to cell.

This model did not satisfy me. The complicated rules seemed to contradict the basic idea of a cellular automaton, namely simple rules. At this point I had doubts whether my approach was the right choice. The approach was based on the assumption that all cells had identical

properties, especially with regard to their position in the root. Therefore, I tried to approach the problem from a different angle. I tried to extract as much information as possible about the calcium wave from the kymograph.

Together with the master's student Janos Löffler, I focused on a prominent property of the wave: the high speed of propagation when stimulated with salt. Based on a model described in the literature, which suggests a coupling of calcium and ROS waves (Evans et al., 2016), we made an effort to answer the following questions: How do the different cell sizes in the root affect the speed of propagation? Do plasmodesmata significantly reduce the speed of propagation? It turned out that it is quite a challenge for the plant to achieve such high speeds.

In order to round off the idea of the "universal messenger calcium" and show downstream effects of calcium signaling, I designed a model of calcium binding to CPK proteins in *Arabidopsis*. At a first glance, the dependencies here are not as complex and ambiguous as with the calcium waves in the root tip after stimulation. Plant stress caused by drought or parasite attacks triggers a calcium burst which usually consists of three or four peaks. Averaged over time, the overall intracellular concentration of calcium increases slightly. As has been shown by in vitro steady state measurements, the CPK proteins CPK21 and CPK23 react differently to this increase. With respect to a given concentration of intracellular calcium, CPK21 and CPK23 are active to different degrees. Furthermore, in the response curves the differing cooperativity of calcium binding is reflected very nicely, since CPK21 shows a sigmoid gradient with a Hill coefficient of approx. 4 (corresponding to a positive cooperativity of four binding sites for calcium) and CPK23 shows almost no cooperativity.

In summary, it can be stated that the question of whether and how the plant transmits information by means of a calcium wave has not yet been finally clarified. My script for automated wave analysis enabled a new way of detailed characterization of the calcium wave. My model simulations gave an insight into how the wave could propagate across the cell boundaries from the root to the shoot and initiate cellular responses such as the closing of the stomata.

8 References

Adamec, L. (1997). Mineral nutrition of carnivorous plants: A review. *The Botanical Review*, 63:273–299.

Adami, C. (2004). Information theory in molecular biology. *Physics of Life Reviews*, 1:3–22.

Agapie, A., Andreica, A. and Giuclea, M. (2014). Probabilistic Cellular Automata. *Journal of computational biology : a journal of computational molecular cell biology*, 21.

Ali, F. and Kwan, A. C. (2020). Interpreting in vivo calcium signals from neuronal cell bodies, axons, and dendrites: a review. *Neurophotonics*, 7.

Allbritton, N. L., Meyer, T. and Stryer, L. (1992). Range of messenger action of calcium ion and inositol 1,4,5-trisphosphate. *Science*, 258:1812–1815.

Allen, G. J., Chu, S. P., Harrington, C. L., Schumacher, K., Hoffmann, T., Tang, Y. Y., Grill, E. and Schroeder, J. I. (2001). A defined range of guard cell calcium oscillation parameters encodes stomatal movements. *Nature*, 411:1053–1057.

Altschul, S. F., Gish, W., Miller, W., Myers, E. W. and Lipman, D. J. (1990). Basic local alignment search tool. *Journal of Molecular Biology*, 215:403–410.

Anderson, J. P., Badruzsaufari, E., Schenk, P. M., Manners, J. M., Desmond, O. J., Ehlert, C., Maclean, D. J., Ebert, P. R. and Kazan, K. (2004). Antagonistic Interaction between Abscisic Acid and Jasmonate-Ethylene Signaling Pathways Modulates Defense Gene Expression and Disease Resistance in Arabidopsis. *The Plant Cell*, 16:3460–3479.

Apweiler, R., Bairoch, A., Wu, C. H., Barker, W. C., Boeckmann, B., Ferro, S., Gasteiger, E., Huang, H., Lopez, R., Magrane, M., Martin, M. J., Natale, D. A., O'Donovan, C., Redaschi, N. and Yeh, L. L. (2004). UniProt: the Universal Protein knowledgebase. *Nucleic Acids Research*, 32:D115–D119.

Atkinson, N. J. and Urwin, P. E. (2012). the interaction of plant biotic and abiotic stresses: from genes to the field | Journal of Experimental Botany | Oxford Academic. *Journal of Experimental Botany*, 63:3523–3544.

Balachandran, S., Hurry, V. M., Kelley, S. E., Osmond, C. B., Robinson, S. A., Rohozinski, J., Seaton, G. G. R. and Sims, D. A. (1997). Concepts of plant biotic stress. Some insights into the stress physiology of virus-infected plants, from the perspective of photosynthesis. *Physiologia Plantarum*, 100:203–213.

Bar-On, Y. M., Phillips, R. and Milo, R. (2018). The biomass distribution on Earth. *Proceedings of the National Academy of Sciences*, 115:6506–6511.

Barker, A., Belyaeva, I., Black, N., Govaerts, R., Lindon, H., Lughadha, E. N., Nicolson, N. and Paton, A. (2016). State of the World's Plants 2016.

Batistič, O. and Kudla, J. (2012). Analysis of calcium signaling pathways in plants. *Biochimica et Biophysica Acta (BBA) - General Subjects*, 1820:1283–1293.

Beck, E. H., Heim, R. and Hansen, J. (2004). Plant resistance to cold stress: Mechanisms and environmental signals triggering frost hardening and dehardening. *Journal of Biosciences*, 29:449–459.

Belongie, S., Malik, J. and Puzicha, J. (2002). Shape matching and object recognition using shape contexts. *IEEE Transactions on Pattern Analysis and Machine Intelligence*, 24:509–522.

Bennett, R. N. and Wallsgrove, R. M. (1994). Secondary metabolites in plant defence mechanisms. *New Phytologist*, 127:617–633.

Berridge, M. J. (1993). Inositol trisphosphate and calcium signalling. *Nature*, 361:315–325.

Berridge, M. J., Bootman, M. D. and Lipp, P. (1998). Calcium - a life and death signal. *Calcium - a life and death signal. Nature*, 395:645–648.

Berridge, M. J., Lipp, P. and Bootman, M. D. (2000). The versatility and universality of calcium signalling. *Nature Reviews Molecular Cell Biology*, 1:11–21.

Beyhl, D., Hörtensteiner, S., Martinoia, E., Farmer, E. E., Fromm, J., Marten, I. and Hedrich, R. (2009). The fou2 mutation in the major vacuolar cation channel TPC1 confers tolerance to inhibitory luminal calcium. *The Plant Journal*, 58:715–723.

Bhattacharjee, S. (2012). The Language of Reactive Oxygen Species Signaling in Plants.

Billker, O., Lourido, S. and Sibley, L. D. (2009). Calcium-Dependent Signaling and Kinases in Apicomplexan Parasites. *Cell Host & Microbe*, 5:612–622.

Bohnert, H., Nelson, D. and Jensen, R. (1995). Adaptations to Environmental Stresses. *The Plant Cell*, 7:1099–1111.

Borghans, J. M., Dupont, G. and Goldbeter, A. (1997). Complex intracellular calcium oscillations A theoretical exploration of possible mechanisms. *Biophysical Chemistry*, 66:25–41.

Bose, J., Pottosin, I., Shabala, S. S. S., Palmgren, M. G. and Shabala, S. (2011). Calcium Efflux Systems in Stress Signaling and Adaptation in Plants. *Frontiers in Plant Science*, 2.

Bouligand, Y. (1986). Fibroblasts, Morphogenesis and Cellular Automata. In E. Bienenstock, F. F. Soulié and G. Weisbuch, editors, *Disordered Systems and Biological Organization*, NATO ASI Series, pages 367–379. Springer, Berlin, Heidelberg.

Braam, J. (1992). Regulated expression of the calmodulin-related TCH genes in cultured Arabidopsis cells: induction by calcium and heat shock. *Proceedings of the National Academy of Sciences of the United States of America*, 89:3213–3216.

Bricchi Irene, Occhipinti Andrea, Bertea Cinzia M., Zebelo Simon A., Brillada Carla, Verrillo Francesca, De Castro Cristina, Molinaro Antonio, Faulkner Christine, Maule Andrew J. and Maffei Massimo E. (2012). Separation of early and late responses to herbivory in Arabidopsis by changing plasmodesmal function. *The Plant Journal*, 73:14–25.

Bugrim, A., Fontanilla, R., Eutenier, B. B., Keizer, J. and Nuccitelli, R. (2003). Sperm Initiate a Ca2+ Wave in Frog Eggs that is More Similar to Ca2+ Waves Initiated by IP3 than by Ca2+. *Biophysical Journal*, 84:1580–1590.

Burl, M. C., Weber, M. and Perona, P. (1998). A probabilistic approach to object recognition using local photometry and global geometry. In *Computer Vision — ECCV'98*, Lecture Notes in Computer Science, pages 628–641. Springer, Berlin, Heidelberg.

Burrone, Juan, Neves, Guilherme, Gomis, Ana, Cooke, Anne and Lagnado, Leon (2002). Endogenous Calcium Buffers Regulate Fast Exocytosis in the Synaptic Terminal of Retinal Bipolar Cells. *Neuron*, 33:101–112.

Cheer, A., Vincent, J.-P., Nuccitelli, R. and Oster, G. (1987). Cortical activity in vertebrate eggs I: The activation waves. *Journal of Theoretical Biology*, 124:377–404.

Chen, Q. and Yang, G. (2020). Signal Function Studies of ROS, Especially RBOH-Dependent ROS, in Plant Growth, Development and Environmental Stress. *Journal of Plant Growth Regulation*, 39:157–171.

Cheng, H. and Lederer, W. J. (2008). Calcium Sparks. *Physiological Reviews*, 88:1491–1545.

Cheng, S., Willmann, M. R., Chen, H. and Sheen, J. (2002). Calcium Signaling through Protein Kinases. The Arabidopsis Calcium-Dependent Protein Kinase Gene Family. *Plant Physiology*, 129:469–485.

Chinchilla, D., Zipfel, C., Robatzek, S., Kemmerling, B., Nürnberger, T., Jones, J. D. G., Felix, G. and Boller, T. (2007). A flagellin-induced complex of the receptor FLS2 and BAK1 initiates plant defence. *Nature*, 448:497–500.

Ching, T., Himmelstein, D. S., Beaulieu-Jones, B. K., Kalinin, A. A., Do, B. T., Way, G. P., Ferrero, E., Agapow, P.-M., Zietz, M., Hoffman, M. M., Xie, W., Rosen, G. L., Lengerich, B. J., Israeli, J., Lanchantin, J., Woloszynek, S., Carpenter, A. E., Shrikumar, A., Xu, J., Cofer, E. M., Lavender, C. A., Turaga, S. C., Alexandari, A. M., Lu, Z., Harris, D. J., DeCaprio, D., Qi, Y., Kundaje, A., Peng, Y., Wiley, L. K., Segler, M. H. S., Boca, S. M., Swamidass, S. J., Huang, A., Gitter, A. and Greene, C. S. (2018). Opportunities and obstacles for deep learning in biology and medicine. *Journal of The Royal Society Interface*, 15:20170387.

Choi, W.-G., Toyota, M., Kim, S.-H., Hilleary, R. and Gilroy, S. (2014). Salt stress-induced Ca2+ waves are associated with rapid, long-distance root-to-shoot signaling in plants. *Proceedings of the National Academy of Sciences*, 111:6497–6502.

Christmann, A., Grill, E. and Huang, J. (2013). Hydraulic signals in long-distance signaling. *Current Opinion in Plant Biology*, 16:293–300.

Christodoulou, J., Malmendal, A., Harper, J. F. and Chazin, W. J. (2004). Evidence for Differing Roles for Each Lobe of the Calmodulin-like Domain in a Calcium-dependent Protein Kinase. *Journal of Biological Chemistry*, 279:29092–29100.

Clapham, D. E. (2007). Calcium Signaling. *Cell*, 131:1047–1058.

Clarkson, D. T. (1984). Calcium transport between tissues and its distribution in the plant. *Plant, Cell & Environment*, 7:449–456.

Conn, S. J., Gilliham, M., Athman, A., Schreiber, A. W., Baumann, U., Moller, I., Cheng, N.-H., Stancombe, M. A., Hirschi, K. D., Webb, A. A., Burton, R., Kaiser, B. N., Tyerman, S. D. and Leigh, R. A. (2011). Cell-Specific Vacuolar Calcium Storage Mediated by CAX1 Regulates Apoplastic Calcium Concentration, Gas Exchange, and Plant Productivity in Arabidopsis[W][OA]. *The Plant Cell*, 23:240–257.

Conrath, U. (2006). Systemic Acquired Resistance. *Plant Signaling & Behavior*, 1:179–184.

Costa, A., Luoni, L., Marrano, C. A., Hashimoto, K., Köster, P., Giacometti, S., Michelis, D., Ida, M., Kudla, J. and Bonza, M. C. (2017). Ca2+-dependent phosphoregulation of the plasma membrane Ca2+-ATPase ACA8 modulates stimulus-induced calcium signatures. *Journal of Experimental Botany*, 68:3215–3230.

Cun, Y. L. (1986). Learning Process in an Asymmetric Threshold Network. In *Disordered Systems and Biological Organization*, NATO ASI Series, pages 233–240. Springer, Berlin, Heidelberg.

Cuthbertson, K. S. R. and Chay, T. R. (1991). Modelling receptor-controlled intracellular calcium oscillators. *Cell Calcium*, 12:97–109.

Dadacz-Narloch, B., Beyhl, D., Larisch, C., López-Sanjurjo, E. J., Reski, R., Kuchitsu, K., Müller, T. D., Becker, D., Schönknecht, G. and Hedrich, R. (2011). A Novel Calcium Binding Site in the Slow Vacuolar Cation Channel TPC1 Senses Luminal Calcium Levels. *The Plant Cell*, 23:2696–2707.

Darwin, C. R. (1880). *The power of movement in plants. London: John Murray.* London: John Murray.

Dawson, S. P., Keizer, J. and Pearson, J. E. (1999). Fire–diffuse–fire model of dynamics of intracellular calcium waves. *Proceedings of the National Academy of Sciences*, 96:6060–6063.

DeFalco, T. A., Bender, K. W. and Snedden, W. A. (2009). Breaking the code: Ca2+ sensors in plant signalling. *Biochemical Journal*, 425:27–40.

Delormel, T. Y. and Boudsocq, M. (2019). Properties and functions of calcium-dependent protein kinases and their relatives in Arabidopsis thaliana. *New Phytologist*, 224:585–604.

Demir, F., Horntrich, C., Blachutzik, J. O., Scherzer, S., Reinders, Y., Kierszniowska, S., Schulze, W. X., Harms, G. S., Hedrich, R., Geiger, D. and Kreuzer, I. (2013). Arabidopsis nanodomain-delimited ABA signaling pathway regulates the anion channel SLAH3. *Proceedings of the National Academy of Sciences*, 110:8296–8301.

Diaz, M., Sanchez-Barrena, M. J., Gonzalez-Rubio, J. M., Rodriguez, L., Fernandez, D., Antoni, R., Yunta, C., Belda-Palazon, B., Gonzalez-Guzman, M., Peirats-Llobet, M., Menendez, M., Boskovic, J., Marquez, J. A., Rodriguez, P. L. and Albert, A. (2016). Calcium-dependent oligomerization of CAR proteins at cell membrane modulates ABA signaling. *Proceedings of the National Academy of Sciences*, 113:E396–E405.

Dietrich, P., Sanders, D. and Hedrich, R. (2001). The role of ion channels in light-dependent stomatal opening. *Journal of Experimental Botany*, 52:1959–1967.

Ding, Y., Shi, Y. and Yang, S. (2019). Advances and challenges in uncovering cold tolerance regulatory mechanisms in plants. *New Phytologist*, 222:1690–1704.

Dodd, A. N., Kudla, J. and Sanders, D. (2010). The Language of Calcium Signaling. *Annual Review of Plant Biology*, 61:593–620.

Dollar, P., Tu, Z., Perona, P. and Belongie, S. (2009). Integral Channel Features. In *Proc. BMVC*, pages 91.1–91.11.

Dolmetsch, R. E., Xu, K. and Lewis, R. S. (1998). Calcium oscillations increase the efficiency and specificity of gene expression. *Nature*, 392:933–936.

Dubiella, U., Seybold, H., Durian, G., Komander, E., Lassig, R., Witte, C.-P., Schulze, W. X. and Romeis, T. (2013). Calcium-dependent protein kinase/NADPH oxidase activation circuit is required for rapid defense signal propagation. *Proceedings of the National Academy of Sciences*, 110:8744–8749.

Dupont, G., Combettes, L., Bird, G. S. and Putney, J. W. (2011). Calcium Oscillations. *Cold Spring Harbor Perspectives in Biology*, 3.

Dupont, G. and Dumollard, R. (2004). Simulation of calcium waves in ascidian eggs: insights into the origin of the pacemaker sites and the possible nature of the sperm factor. *Journal of Cell Science*, 117:4313–4323.

Emery, L., Whelan, S., Hirschi, K. D. and Pittman, J. K. (2012). Protein Phylogenetic Analysis of Ca2+/cation Antiporters and Insights into their Evolution in Plants. *Frontiers in plant science*, 3.

Endo, M. (1977). Calcium release from the sarcoplasmic reticulum. *Physiological Reviews*, 57:71–108.

Erb, M. and Kliebenstein, D. J. (2020). Plant Secondary Metabolites as Defenses, Regulators, and Primary Metabolites: The Blurred Functional Trichotomy. *Plant Physiology*, 184:39–52.

Evans, M. J., Choi, W.-G., Gilroy, S. and Morris, R. J. (2016). A ROS-Assisted Calcium Wave Dependent on the AtRBOHD NADPH Oxidase and TPC1 Cation Channel Propagates the Systemic Response to Salt Stress. *Plant Physiology*, 171:1771–1784.

Faas, G. C., Schwaller, B., Vergara, J. L. and Mody, I. (2007). Resolving the Fast Kinetics of Cooperative Binding: Ca2+ Buffering by Calretinin. *PLOS Biology*, 5:e311.

Falcke, M. (2004). Reading the patterns in living cells —the physics of ca2+ signaling. *Advances in Physics*, 53:255–440.

Falcke, M., Bär, M., Lechleiter, J. D. and Hudson, J. L. (1999). Spiral breakup and defect dynamics in a model for intracellular Ca2+ dynamics. *Physica D: Nonlinear Phenomena*, 129:236–252.

Felle, H. H. and Zimmermann, M. R. (2007). Systemic signalling in barley through action potentials. *Planta*, 226:203.

Felzenszwalb, P. F., Girshick, R. B., McAllester, D. and Ramanan, D. (2010). Object Detection with Discriminatively Trained Part-Based Models. *IEEE Transactions on Pattern Analysis and Machine Intelligence*, 32:1627–1645.

Franz, S., Ehlert, B., Liese, A., Kurth, J., Cazalé, A.-C. and Romeis, T. (2011). Calcium-Dependent Protein Kinase CPK21 Functions in Abiotic Stress Response in Arabidopsis thaliana. *Molecular Plant*, 4:83–96.

Förster, J., Bergmann, F. T. and Pahle, J. (2021). CoRC: the COPASI R Connector. *Bioinformatics*.

García, A. V. and Hirt, H. (2014). Salmonella enterica induces and subverts the plant immune system. *Frontiers in Microbiology*, 5.

Gardiner, B., Berry, P. and Moulia, B. (2016). Review: Wind impacts on plant growth, mechanics and damage. *Plant Science*, 245:94–118.

Gardner, M. (1970). Mathematical Games. *Scientific American*, 223:120–123.

Geiger, D., Scherzer, S., Mumm, P., Marten, I., Ache, P., Matschi, S., Liese, A., Wellmann, C., Al-Rasheid, K. A. S., Grill, E., Romeis, T. and Hedrich, R. (2010). Guard cell anion channel SLAC1 is regulated by CDPK protein kinases with distinct Ca2+ affinities. *Proceedings of the National Academy of Sciences of the United States of America*, 107:8023–8028.

Geilfus, C.-M. (2017). The pH of the Apoplast: Dynamic Factor with Functional Impact Under Stress. *Molecular Plant*, 10:1371–1386.

Geisler, M., Frangne, N., Gomès, E., Martinoia, E. and Palmgren, M. G. (2000). The ACA4 Gene of Arabidopsis Encodes a Vacuolar Membrane Calcium Pump That Improves Salt Tolerance in Yeast. *Plant Physiology*, 124:1814–1827.

Geisler, Markus, Axelsen, Kristian B., Harper, Jeffrey F. and Palmgren, Michael G. (2000). Molecular aspects of higher plant P-type Ca2+-ATPases. *Biochimica et Biophysica Acta (BBA) - Biomembranes*, 1465:52–78.

Gesztelyi, R., Zsuga, J., Kemeny-Beke, A., Varga, B., Juhasz, B. and Tosaki, A. (2012). The Hill equation and the origin of quantitative pharmacology. *Archive for History of Exact Sciences*, 66:427–438.

Giehl, R. F. H. and Wirén, N. v. (2014). Root Nutrient Foraging. *Plant Physiology*, 166:509–517.

Gilroy, S., Read, N. D. and Trewavas, A. J. (1990). Elevation of cytoplasmic calcium by caged calcium or caged inositol trisphosphate initiates stomatal closure. *Nature*, 346:769–771.

Girshick, R., Donahue, J., Darrell, T. and Malik, J. (2014). Rich Feature Hierarchies for Accurate Object Detection and Semantic Segmentation. In *2014 IEEE Conference on Computer Vision and Pattern Recognition*, pages 580–587.

Gong, Z., Xiong, L., Shi, H., Yang, S., Herrera-Estrella, L. R., Xu, G., Chao, D.-Y., Li, J., Wang, P.-Y., Qin, F., Li, J., Ding, Y., Shi, Y., Wang, Y., Yang, Y., Guo, Y. and Zhu, J.-K. (2020). Plant abiotic stress response and nutrient use efficiency. *Science China Life Sciences*, 63:635–674.

Gonzalez, R. C. and Woods, R. E. (2017). *Digital Image Processing*. Pearson, New York, NY, 4. edition edition.

Grossmann, G., Guo, W.-J., Ehrhardt, D. W., Frommer, W. B., Sit, R. V., Quake, S. R. and Meier, M. (2011). The RootChip: An Integrated Microfluidic Chip for Plant Science. *The Plant Cell*, 23:4234–4240.

Gruber, B. D., Giehl, R. F. H., Friedel, S. and Wirén, N. v. (2013). Plasticity of the Arabidopsis Root System under Nutrient Deficiencies. *Plant Physiology*, 163:161–179.

Gundlach, H., Müller, M. J., Kutchan, T. M. and Zenk, M. H. (1992). Jasmonic acid is a signal transducer in elicitor-induced plant cell cultures. *Proceedings of the National Academy of Sciences of the United States of America*, 89:2389–2393.

Guo, J., Zeng, W., Chen, Q., Lee, C., Chen, L., Yang, Y., Cang, C., Ren, D. and Jiang, Y. (2016). Structure of the voltage-gated two-pore channel TPC1 from Arabidopsis thaliana. *Nature*, 531:196–201.

Hanley, M. E., Lamont, B. B., Fairbanks, M. M. and Rafferty, C. M. (2007). Plant structural traits and their role in anti-herbivore defence. *Perspectives in Plant Ecology, Evolution and Systematics*, 8:157–178.

Hao, H., Fan, L., Chen, T., Li, R., Li, X., He, Q., Botella, M. A. and Lin, J. (2014). Clathrin and Membrane Microdomains Cooperatively Regulate RbohD Dynamics and Activity in Arabidopsis. *The Plant Cell*, 26:1729–1745.

Harper, J. F., Breton, G. and Harmon, A. (2004). Decoding Ca2+ signals through plant protein kinases. *Annual Review of Plant Biology*, 55:263–288.

Hashimoto, K. and Kudla, J. (2011). Calcium decoding mechanisms in plants. *Biochimie*, 93:2054–2059.

He, M. and Ding, N.-Z. (2020). Plant Unsaturated Fatty Acids: Multiple Roles in Stress Response. *Frontiers in Plant Science*, 11.

He, M., He, C.-Q. and Ding, N.-Z. (2018). Abiotic Stresses: General Defenses of Land Plants and Chances for Engineering Multistress Tolerance. *Frontiers in Plant Science*, 9.

Hedrich, R., Flügge, U. I. and Fernandez, J. M. (1986). Patch-clamp studies of ion transport in isolated plant vacuoles. *FEBS Letters*, 204:228–232.

Hedrich, R. and Marten, I. (2011). TPC1 – SV Channels Gain Shape. *Molecular Plant*, 4:428–441.

Hedrich, R., Mueller, T. D., Becker, D. and Marten, I. (2018). Structure and Function of TPC1 Vacuole SV Channel Gains Shape. *Molecular Plant*, 11:764–775.

Hedrich, R. and Neher, E. (1987). Cytoplasmic calcium regulates voltage-dependent ion channels in plant vacuoles. *Nature*, 329:833–836.

Hedrich, Rainer, Mueller, Thomas D., Becker, Dirk and Marten, Irene (2018). Structure and Function of TPC1 Vacuole SV Channel Gains Shape. *Molecular Plant*, 11:764–775.

Heil, M. and Ton, J. (2008). Long-distance signalling in plant defence. *Trends in Plant Science*, 13:264–272.

Hetherington, A. M. and Brownlee, C. (2004). The generation of Ca2+ signals in plants. *Annual Review of Plant Biology*, 55:401–427.

Hill, A. V. (1910). The possible effects of the aggregation of the molecules of haemoglobin on its oxygen dissociation curve – ScienceOpen. *The Journal of Physiology*, 60:4–7.

Hooft, G. t. (2016). *The Cellular Automaton Interpretation of Quantum Mechanics*. Fundamental Theories of Physics. Springer International Publishing.

Hoops, S., Sahle, S., Gauges, R., Lee, C., Pahle, J., Simus, N., Singhal, M., Xu, L., Mendes, P. and Kummer, U. (2006). COPASI—a COmplex PAthway SImulator. *Bioinformatics*, 22:3067–3074.

Hopfield, J. J. (1982). Neural networks and physical systems with emergent collective computational abilities. *Proceedings of the National Academy of Sciences*, 79:2554–2558.

Houart, G., Dupont, G. and Goldbeter, A. (1999). Bursting, chaos and birhythmicity originating from self-modulation of the inositol 1,4,5-trisphosphate signal in a model for intracellular Ca2+ oscillations. *Bulletin of Mathematical Biology*, 61:507–530.

Howe, G. A. and Jander, G. (2008). Plant Immunity to Insect Herbivores. *Annual Review of Plant Biology*, 59:41–66.

Huang, S., Waadt, R., Nuhkat, M., Kollist, H., Hedrich, R. and Roelfsema, M. R. G. (2019). Calcium signals in guard cells enhance the efficiency by which abscisic acid triggers stomatal closure. *New Phytologist*, 224:177–187.

Hutcheson, S. W. (1998). Current Concepts of Active Defense in Plants. *Annual Review of Phytopathology*, 36:59–90.

Hutton, T. J. (2010). Codd's Self-Replicating Computer. *Artificial Life*, 16:99–117.

Iida, K., Seki, M., Sakurai, T., Satou, M., Akiyama, K., Toyoda, T., Konagaya, A. and Shinozaki, K. (2004). Genome-wide analysis of alternative pre-mRNA splicing in Arabidopsis thaliana based on full-length cDNA sequences. *Nucleic Acids Research*, 32:5096–5103.

Isah, T. (2019). Stress and defense responses in plant secondary metabolites production. *Biological Research*, 52.

Jaffe, L. F. (2008). Calcium waves. *Philosophical Transactions of the Royal Society B: Biological Sciences*, 363:1311–1317.

Kabała, K. and Kłobus, G. (2005). Plant Ca2+-ATPases. *Acta Physiologiae Plantarum*, 27:559–574.

Kanchiswamy, C. N., Malnoy, M., Occhipinti, A. and Maffei, M. E. (2014). Calcium Imaging Perspectives in Plants. *International Journal of Molecular Sciences*, 15:3842–3859.

Kaplan, B., Davydov, O., Knight, H., Galon, Y., Knight, M. R., Fluhr, R. and Fromm, H. (2006). Rapid Transcriptome Changes Induced by Cytosolic Ca2+ Transients Reveal ABRE-Related Sequences as Ca2+-Responsive cis Elements in Arabidopsis. *The Plant Cell*, 18:2733–2748.

Keinath, N. F., Waadt, R., Brugman, R., Schroeder, J. I., Grossmann, G., Schumacher, K. and Krebs, M. (2015). Live Cell Imaging with R-GECO1 Sheds Light on flg22- and Chitin-Induced Transient [Ca2+]cyt Patterns in Arabidopsis. *Molecular Plant*, 8:1188–1200.

Kiep Victoria, Vadassery Jyothilakshmi, Lattke Justus, Maaß Jan-Peter, Boland Wilhelm, Peiter Edgar and Mithöfer Axel (2015). Systemic cytosolic Ca2+ elevation is activated upon wounding and herbivory in Arabidopsis. *New Phytologist*, 207:996–1004.

Kintzer, A. F. and Stroud, R. M. (2018). On the Structure and Mechanism of Two-Pore Channels. *The FEBS journal*, 285:233–243.

Klessig, D. F., Choi, H. W. and Dempsey, D. A. (2018). Systemic Acquired Resistance and Salicylic Acid: Past, Present, and Future. *Molecular Plant-Microbe Interactions®*, 31:871–888.

Klüsener, B., Young, J. J., Murata, Y., Allen, G. J., Mori, I. C., Hugouvieux, V. and Schroeder, J. I. (2002). Convergence of Calcium Signaling Pathways of Pathogenic Elicitors and Abscisic Acid in Arabidopsis Guard Cells. *Plant Physiology*, 130:2152–2163.

Knight, H., Trewavas, A. J. and Knight, M. R. (1997). Calcium signalling in Arabidopsis thaliana responding to drought and salinity. *The Plant Journal*, 12:1067–1078.

Ko, D., Kang, J., Kiba, T., Park, J., Kojima, M., Do, J., Kim, K. Y., Kwon, M., Endler, A., Song, W.-Y., Martinoia, E., Sakakibara, H. and Lee, Y. (2014). Arabidopsis ABCG14 is essential for the root-to-shoot translocation of cytokinin. *Proceedings of the National Academy of Sciences of the United States of America*, 111:7150–7155.

Koo, A. J. and Howe, G. A. (2009). The wound hormone jasmonate. *Phytochemistry*, 70:1571–1580.

Krasensky, J. and Jonak, C. (2012). Drought, salt, and temperature stress-induced metabolic rearrangements and regulatory networks. *Journal of experimental botany*, 63:1593–1608.

Kretsinger, R. H. and Nockolds, C. E. (1973). Carp Muscle Calcium-binding Protein II. Structure Determination and General Description. *Journal of Biological Chemistry*, 248:3313–3326.

Kroeger, J. H., Geitmann, A. and Grant, M. (2008). Model for calcium dependent oscillatory growth in pollen tubes. *Journal of Theoretical Biology*, 253:363–374.

Kudla, J., Batistič, O. and Hashimoto, K. (2010). Calcium Signals: The Lead Currency of Plant Information Processing. *The Plant Cell*, 22:541–563.

Kudla, J., Becker, D., Grill, E., Hedrich, R., Hippler, M., Kummer, U., Parniske, M., Romeis, T. and Schumacher, K. (2018). Advances and current challenges in calcium signaling. *The New Phytologist*.

Kummer, U., Krajnc, B., Pahle, J., Green, A. K., Dixon, C. J. and Marhl, M. (2005). Transition from Stochastic to Deterministic Behavior in Calcium Oscillations. *Biophysical Journal*, 89:1603–1611.

Kummer, U., Olsen, L. F., Dixon, C. J., Green, A. K., Bornberg-Bauer, E. and Baier, G. (2000). Switching from simple to complex oscillations in calcium signaling. *Biophysical Journal*, 79:1188–1195.

Lamers, J., Meer, T. v. d. and Testerink, C. (2020). How Plants Sense and Respond to Stressful Environments. *Plant Physiology*, 182:1624–1635.

Langton, C. G. (1984). Self-reproduction in cellular automata. *Physica D: Nonlinear Phenomena*, 10:135–144.

Larsen, A. Z. and Kummer, U. (2003). Information Processing in Calcium Signal Transduction. In M. Falcke and D. Malchow, editors, *Understanding Calcium Dynamics*, number 623 in Lecture Notes in Physics, pages 153–178. Springer Berlin Heidelberg.

Larsen, A. Z., Olsen, L. F. and Kummer, U. (2004). On the encoding and decoding of calcium signals in hepatocytes. *Biophysical Chemistry*, 107:83–99.

Lawlor, D. (2011). Abiotic Stress Adaptation in Plants. Physiological, Molecular and Genomic Foundation. *Annals of Botany*, 107:vii–ix.

Lee, S., Choi, H., Suh, S., Doo, I.-S., Oh, K.-Y., Choi, E. J., Taylor, A. T. S., Low, P. S. and Lee, Y. (1999). Oligogalacturonic Acid and Chitosan Reduce Stomatal Aperture by Inducing the Evolution of Reactive Oxygen Species from Guard Cells of Tomato and Commelina communis. *Plant Physiology*, 121:147–152.

Leigh, R. A. (1997). Solute Composition of Vacuoles. In R. A. Leigh, D. Sanders and J. A.

Callow, editors, *Advances in Botanical Research*, volume 25 of *The Plant Vacuole*, pages 171–194. Academic Press.

Li, J., Julie Lee, Y.-R. and Assmann, S. M. (1998). Guard Cells Possess a Calcium-Dependent Protein Kinase That Phosphorylates the KAT1 Potassium Channel. *Plant Physiology*, 116:785–795.

Lowe, D. G. (1999). Object recognition from local scale-invariant features. In *Proceedings of the Seventh IEEE International Conference on Computer Vision*, volume 2, pages 1150–1157. Institute of Electrical and Electronics Engineers (IEEE).

Lucas, J. R. and Shaw, S. L. (2012). MAP65-1 and MAP65-2 promote cell proliferation and axial growth in Arabidopsis roots. *The Plant Journal*, 71:454–463.

Luit, A. H. v. d., Olivari, C., Haley, A., Knight, M. R. and Trewavas, A. J. (1999). Distinct Calcium Signaling Pathways Regulate Calmodulin Gene Expression in Tobacco. *Plant Physiology*, 121:705–714.

MacRobbie, E. A. C. (2000). ABA activates multiple Ca2+ fluxes in stomatal guard cells, triggering vacuolar K+(Rb+) release. *Proceedings of the National Academy of Sciences*, 97:12361–12368.

Martin, D. R., Fowlkes, C. C. and Malik, J. (2004). Learning to detect natural image boundaries using local brightness, color, and texture cues. *IEEE Transactions on Pattern Analysis and Machine Intelligence*, 26:530–549.

MathWorks (2014). Parula. https://blogs.mathworks.com/steve/2014/10/13/a-new-colormap-for-matlab-part-1-introduction/.

McAinsh, M. R., Brownlee, C. and Hetherington, A. M. (1990). Abscisic acid-induced elevation of guard cell cytosolic Ca 2+ precedes stomatal closure. *Nature*, 343:186–188.

McAinsh, M. R. and Hetherington, A. M. (1998). Encoding specificity in Ca2+ signalling systems. *Trends in Plant Science*, 3:32–36.

McAinsh, M. R. and Pittman, J. K. (2009). Shaping the calcium signature. *New Phytologist*, 181:275–294.

McCulloch, W. S. and Pitts, W. (1943). A logical calculus of the ideas immanent in nervous activity. *The bulletin of mathematical biophysics*, 5:115–133.

Melotto, M., Underwood, W., Koczan, J., Nomura, K. and He, S. Y. (2006). Plant Stomata Function in Innate Immunity against Bacterial Invasion. *Cell*, 126:969–980.

Meyer, T. and Stryer, L. (1988). Molecular model for receptor-stimulated calcium spiking. *Proceedings of the National Academy of Sciences of the United States of America*, 85:5051–5055.

Miller, G., Schlauch, K., Tam, R., Cortes, D., Torres, M. A., Shulaev, V., Dangl, J. L. and Mittler, R. (2009). The Plant NADPH Oxidase RBOHD Mediates Rapid Systemic Signaling in Response to Diverse Stimuli. *Sci. Signal.*, 2:ra45–ra45.

Minsky, M. L. and Papert, j. a., Seymou (1969). *Perceptrons : an introduction to computational geometry*. Cambridge, Mass. : MIT Press.

Monshausen, G. B., Messerli, M. A. and Gilroy, S. (2008). Imaging of the Yellow Cameleon 3.6 Indicator Reveals That Elevations in Cytosolic Ca2+ Follow Oscillating Increases in Growth in Root Hairs of Arabidopsis. *Plant Physiology*, 147:1690–1698.

Mori, I. C., Murata, Y., Yang, Y., Munemasa, S., Wang, Y.-F., Andreoli, S., Tiriac, H., Alonso, J. M., Harper, J. F., Ecker, J. R., Kwak, J. M. and Schroeder, J. I. (2006). CDPKs CPK6 and CPK3 Function in ABA Regulation of Guard Cell S-Type Anion- and Ca2+- Permeable Channels and Stomatal Closure. *PLOS Biology*, 4:e327.

Mousavi, S. A. R., Chauvin, A., Pascaud, F., Kellenberger, S. and Farmer, E. E. (2013). GLUTAMATE RECEPTOR-LIKE genes mediate leaf-to-leaf wound signalling. *Nature*, 500:422–426.

Müller-Reichert, T. (2010). *Electron Microscopy of Model Systems*. Academic Press, Amsterdam, 1 edition.

Nagel, K. and Schreckenberg, M. (1992). A cellular automaton model for freeway traffic. *Journal de Physique I*, 2:2221–2229.

Nap, J.-P. and Bisseling, T. (1990). Developmental Biology of a Plant-Prokaryote Symbiosis: The Legume Root Nodule. *Science*, 250:948–954.

Nelson, M. R., Thulin, E., Fagan, P. A., Forsén, S. and Chazin, W. J. (2001). The EF-hand domain: A globally cooperative structural unit. *Protein Science*, 11:198–205.

Nguyen, A., Yosinski, J. and Clune, J. (2015). Deep neural networks are easily fooled: High confidence predictions for unrecognizable images. In *2015 IEEE Conference on Computer Vision and Pattern Recognition (CVPR)*, pages 427–436.

Nguyen, V., Mathias, R. and Smith, G. D. (2005). A stochastic automata network descriptor for Markov chain models of instantaneously coupled intracellular Ca2+ channels. *Bulletin of Mathematical Biology*, 67:393–432.

Niehl, A. and Heinlein, M. (2011). Cellular pathways for viral transport through plasmodesmata. *Protoplasma*, 248:75–99.

Nägele, T. and Heyer, A. G. (2013). Approximating subcellular organisation of carbohydrate metabolism during cold acclimation in different natural accessions of Arabidopsis thaliana. *New Phytologist*, 198:777–787.

Ogasawara, Y., Kaya, H., Hiraoka, G., Yumoto, F., Kimura, S., Kadota, Y., Hishinuma, H., Senzaki, E., Yamagoe, S., Nagata, K., Nara, M., Suzuki, K., Tanokura, M. and Kuchitsu, K. (2008). Synergistic Activation of the Arabidopsis NADPH Oxidase AtrbohD by Ca2+ and Phosphorylation. *Journal of Biological Chemistry*, 283:8885–8892.

Pahle, J., Green, A. K., Dixon, C. J. and Kummer, U. (2008). Information transfer in signaling pathways: A study using coupled simulated and experimental data. *BMC Bioinformatics*, 9:139.

Paiva, E. A. S. (2019). Are calcium oxalate crystals a dynamic calcium store in plants? *New Phytologist*, 223:1707–1711.

Palusa, S. G., Ali, G. S. and Reddy, A. S. N. (2007). Alternative splicing of pre-mRNAs of Arabidopsis serine/arginine-rich proteins: regulation by hormones and stresses. *The Plant Journal*, 49:1091–1107.

Pandey, S. and Assmann, S. M. (2004). The Arabidopsis Putative G Protein–Coupled Receptor GCR1 Interacts with the G Protein alpha Subunit GPA1 and Regulates Abscisic Acid Signaling. *The Plant Cell*, 16:1616–1632.

Pandey, S., Zhang, W. and Assmann, S. M. (2007). Roles of ion channels and transporters in guard cell signal transduction. *FEBS Letters*, 581:2325–2336.

Pedmale, U. V., Celaya, R. B. and Liscum, E. (2010). Phototropism: Mechanism and Outcomes. *The Arabidopsis Book / American Society of Plant Biologists*, 8.

Peiter, E., Maathuis, F. J. M., Mills, L. N., Knight, H., Pelloux, J., Hetherington, A. M. and Sanders, D. (2005). The vacuolar Ca2+-activated channel TPC1 regulates germination and stomatal movement. *Nature*, 434:404–408.

Petzold, L. (1983). Automatic Selection of Methods for Solving Stiff and Nonstiff Systems of Ordinary Differential Equations. *SIAM Journal on Scientific and Statistical Computing*, 4:136–148.

Pfeifer, B., Kugler, K., Tejada, M. M., Baumgartner, C., Seger, M., Osl, M., Netzer, M., Handler, M., Dander, A., Wurz, M., Graber, A. and Tilg, B. (2008). A Cellular Automaton Framework for Infectious Disease Spread Simulation. *The Open Medical Informatics Journal*, 2:70–81.

Pirayesh, N., Giridhar, M., Ben Khedher, A., Vothknecht, U. C. and Chigri, F. (2021). Organellar calcium signaling in plants: An update. *Biochimica et Biophysica Acta (BBA) - Molecular Cell Research*, 1868:118948.

Plieth, C. (2005). Calcium: Just Another Regulator in the Machinery of Life? *Annals of Botany*, 96:1–8.

Pottosin, I., Wherrett, T. and Shabala, S. (2009). SV channels dominate the vacuolar Ca2+ release during intracellular signaling. *FEBS Letters*, 583:921–926.

Płachno, B. J., Adamec, L. and Huet, H. (2009). Mineral nutrient uptake from prey and glandular phosphatase activity as a dual test of carnivory in semi-desert plants with glandular leaves suspected of carnivory. *Annals of Botany*, 104:649–654.

Qi, X. and Torii, K. U. (2018). Hormonal and environmental signals guiding stomatal development. *BMC Biology*, 16:21.

R Core Team (2020). *R: A Language and Environment for Statistical Computing*. R Foundation for Statistical Computing, Vienna, Austria.

Ranf, S., Wünnenberg, P., Lee, J., Becker, D., Dunkel, M., Hedrich, R., Scheel, D. and Dietrich, P. (2008). Loss of the vacuolar cation channel, AtTPC1, does not impair Ca2+ signals induced by abiotic and biotic stresses. *The Plant Journal*, 53:287–299.

Ranty, B., Aldon, D., Cotelle, V., Galaud, J.-P., Thuleau, P. and Mazars, C. (2016). Calcium Sensors as Key Hubs in Plant Responses to Biotic and Abiotic Stresses. *Frontiers in Plant Science*, 7.

Read, J. and Stokes, A. (2006). Plant biomechanics in an ecological context. *American Journal of Botany*, 93:1546–1565.

Redmon, J., Divvala, S., Girshick, R. and Farhadi, A. (2016). You Only Look Once: Unified, Real-Time Object Detection. *arXiv:1506.02640 [cs]*.

Reiter, C. (2005). A local cellular model for snow crystal growth. *Chaos, Solitons & Fractals*, 23:1111–1119.

Rizzuto, R. and Pozzan, T. (2006). Microdomains of Intracellular Ca2+: Molecular Determinants and Functional Consequences. *Physiological Reviews*, 86:369–408.

Romeis, T. and Herde, M. (2014). From local to global: CDPKs in systemic defense signaling upon microbial and herbivore attack. *Current Opinion in Plant Biology*, 20:1–10.

Ryals, J., Neuenschwander, U., Willits, M., Molina, A., Steiner, H. and Hunt, M. (1996). Systemic Acquired Resistance. *The Plant Cell*, 8:1809–1819.

Sager, R. E. and Lee, J.-Y. (2018). Plasmodesmata at a glance. *Journal of Cell Science*, 131.

Saijo, Y., Loo, E. P.-i. and Yasuda, S. (2018). Pattern recognition receptors and signaling in plant–microbe interactions. *The Plant Journal*, 93:592–613.

Sali, E. and Ullman, S. (1999). Combining Class-Specific Fragments for Object Classification. In *The 10th British Machine Vision Conference (BMVC)*. University of Nottingham.

Salvador-Recatalà Vicenta, Tjallingii W. Freddy and Farmer Edward E. (2014). Real-time, in vivo intracellular recordings of caterpillar-induced depolarization waves in sieve elements using aphid electrodes. *New Phytologist*, 203:674–684.

Scarth, G. W. and Levitt, J. (1937). The frost-hardening mechanism of plant cells. *Plant Physiology*, 12:51–78.

Schneider, T. D. (2010). A brief review of molecular information theory. *Nano communication networks*, 1:173–180.

Schreiber, T. (2000). Measuring Information Transfer. *Measuring Information Transfer. Physical Review Letters*, 85:461–464.

Schulz, P., Herde, M. and Romeis, T. (2013). Calcium-Dependent Protein Kinases: Hubs in Plant Stress Signaling and Development. *Plant Physiology*, 163:523–530.

Schulze, C., Sticht, H., Meyerhoff, P. and Dietrich, P. (2011). Differential contribution of EF-hands to the Ca2+-dependent activation in the plant two-pore channel TPC1. *The Plant Journal*, 68:424–432.

Schuster, S., Marhl, M. and Höfer, T. (2002). Modelling of simple and complex calcium oscillations. *European Journal of Biochemistry*, 269:1333–1355.

Schwaller, B. (2010). Cytosolic Ca2+ Buffers. *Cold Spring Harbor Perspectives in Biology*, 2.

Schönknecht, G. (2013). Calcium Signals from the Vacuole. *Plants*, 2:589–614.

Scrase-Field, S. A. and Knight, M. R. (2003). Calcium: just a chemical switch? *Current Opinion in Plant Biology*, 6:500–506.

Shen, P. and Larter, R. (1995). Chaos in intracellular Ca2+ oscillations in a new model for non-excitable cells. *Cell Calcium*, 17:225–232.

Singh, N. and Pandey, G. K. (2020). Calcium signatures and signal transduction schemes during microbe interactions in Arabidopsis thaliana. *Journal of Plant Biochemistry and Biotechnology*, 29:675–686.

Sivic, J. and Zisserman, A. (2003). Video Google: A Text Retrieval Approach to Object Matching in Videos. In *Proceedings of the Ninth IEEE International Conference on Computer Vision*, volume 2 of *ICCV '03*, pages 1470–1477. IEEE Computer Society, USA.

Slovik, S., Daeter, W. and Hartung, W. (1995). Compartmental redistribution and long-distance transport of abscisic acid (ABA) in plants as influenced by environmental changes in the rhizosphere — a biomathematical model. *Journal of Experimental Botany*, 46:881–894.

Smedler, E. and Uhlén, P. (2014). Frequency decoding of calcium oscillations. *Biochimica et Biophysica Acta (BBA) - General Subjects*, 1840:964–969.

Sneyd, J., Keizer, J. and Sanderson, M. J. (1995). Mechanisms of calcium oscillations and waves: a quantitative analysis. *The FASEB Journal*, 9:1463–1472.

Sobel, I. and Feldman, G. (1968). A 3×3 Isotropic Gradient Operator for Image Processing. *A Talk at the Stanford Artificial Project*, pages 271–272.

Solovey, G., Fraiman, D., Pando, B. and Ponce Dawson, S. (2008). Simplified model of cytosolic Ca2+ dynamics in the presence of one or several clusters of Ca2+ -release channels. *Physical Review. E, Statistical, Nonlinear, and Soft Matter Physics*, 78:041915.

Soto, M., Nogales, J., Pérez-Mendoza, D., Gallegos, M.-T., Olivares, J. and Sanjuán, J. (2011). Pathogenic and mutualistic plant-bacteria interactions: ever increasing similarities. *Open Life Sciences*, 6:911–917.

Staxén, I., Pical, C., Montgomery, L. T., Gray, J. E., Hetherington, A. M. and McAinsh, M. R. (1999). Abscisic acid induces oscillations in guard-cell cytosolic free calcium that involve phosphoinositide-specific phospholipase C. *Proceedings of the National Academy of Sciences*, 96:1779–1784.

Storn, R. and Price, K. (1997). Differential Evolution – A Simple and Efficient Heuristic for global Optimization over Continuous Spaces. *Journal of Global Optimization*, 11:341–359.

Straube, R. and Ridgway, D. (2009). Investigating the effects of molecular crowding on Ca2+ diffusion using a particle-based simulation model. *Chaos: An Interdisciplinary Journal of Nonlinear Science*, 19:037110.

Sun, Y., Huang, D. and Chen, X. (2019). Dynamic regulation of plasmodesmatal permeability and its application to horticultural research. *Horticulture Research*, 6:1–11.

Swaminathan, D., Ullah, G. and Jung, P. (2009). A simple sequential-binding model for calcium puffs. *Chaos: An Interdisciplinary Journal of Nonlinear Science*, 19:037109.

Swarbreck, D., Wilks, C., Lamesch, P., Berardini, T. Z., Garcia-Hernandez, M., Foerster, H., Li, D., Meyer, T., Muller, R., Ploetz, L., Radenbaugh, A., Singh, S., Swing, V., Tissier, C., Zhang, P. and Huala, E. (2008). The Arabidopsis Information Resource (TAIR): gene structure and function annotation. *Nucleic Acids Research*, 36:D1009–D1014.

Takahashi, S. (1992). Self-similarity of linear cellular automata. *Journal of Computer and System Sciences*, 44:114–140.

The UniProt Consortium (2019). UniProt: a worldwide hub of protein knowledge. *Nucleic Acids Research*, 47:D506–D515.

Toescu, E. C. (1995). Temporal and spatial heterogeneities of Ca2+ signaling: mechanisms and physiological roles. *American Journal of Physiology-Gastrointestinal and Liver Physiology*, 269:G173–G185.

Tripathi, D., Raikhy, G. and Kumar, D. (2019). Chemical elicitors of systemic acquired resistance—Salicylic acid and its functional analogs. *Current Plant Biology*, 17:48–59.

Ulam, S. (1962). On some mathematical problems connected with patterns of growth of figures. *Mathematical Problems in the Biological Sciences: Proceedings of Symposia in Applied Mathematics*, 14:215–224.

Ullah, G., Parker, I., Mak, D.-O. D. and Pearsona, J. E. (2012). Multi-Scale Data-Driven Modeling and Observation of Calcium Puffs. *Cell calcium*, 52:152–160.

Umbaugh, S. E. (2017). *Digital Image Processing and Analysis with MATLAB and CVIPtools*. CRC Press, 3 edition.

Urbanek, S. (2013a). *png: Read and write PNG images*.

Urbanek, S. (2013b). *tiff: Read and write TIFF images*.

Vahisalu, T., Kollist, H., Wang, Y.-F., Nishimura, N., Chan, W.-Y., Valerio, G., Lamminmäki, A., Brosché, M., Moldau, H., Desikan, R., Schroeder, J. I. and Kangasjärvi, J. (2008). SLAC1 is required for plant guard cell S-type anion channel function in stomatal signalling. *Nature*, 452:487–491.

Valmonte, G. R., Arthur, K., Higgins, C. M. and MacDiarmid, R. M. (2014). Calcium-Dependent Protein Kinases in Plants: Evolution, Expression and Function. *Plant and Cell Physiology*, 55:551–569.

van Bel, A. J. E., Furch, A. C. U., Will, T., Buxa, S. V., Musetti, R. and Hafke, J. B. (2014). Spread the news: systemic dissemination and local impact of Ca2+ signals along the phloem pathway. *Journal of Experimental Botany*, 65:1761–1787.

van Stroe-Biezen, S. A. M., Everaerts, F. M., Janssen, L. J. J. and Tacken, R. A. (1993). Diffusion coefficients of oxygen, hydrogen peroxide and glucose in a hydrogel. *Analytica Chimica Acta*, 273:553–560.

Vaz Martins, T., Evans, M. J., Woolfenden, H. C. and Morris, R. J. (2013). Towards the Physics of Calcium Signalling in Plants. *Plants*, 2:541–588.

Vestergaard, C. L., Flyvbjerg, H. and Møller, I. M. (2012). Intracellular Signaling by Diffusion: Can Waves of Hydrogen Peroxide Transmit Intracellular Information in Plant Cells? *Frontiers in Plant Science*, 3.

Vikram Mutneja, D. (2015). Methods of Image Edge Detection: A Review. *Journal of Electrical & Electronic Systems*, 04.

Vlot, A. C., Sales, J. H., Lenk, M., Bauer, K., Brambilla, A., Sommer, A., Chen, Y., Wenig, M. and Nayem, S. (2021). Systemic propagation of immunity in plants. *New Phytologist*, 229:1234–1250.

Von Neumann, J. and Burks, A. W. A. W. (1966). *Theory of self-reproducing automata*. Urbana, University of Illinois Press.

Wagner, A. (2017). Information theory, evolutionary innovations and evolvability. *Philosophical Transactions of the Royal Society B: Biological Sciences*, 372:20160416.

Walley, J. W. and Dehesh, K. (2010). Molecular Mechanisms Regulating Rapid Stress Signaling Networks in Arabidopsis. *Journal of Integrative Plant Biology*, 52:354–359.

Wang, Y., Dindas, J., Rienmüller, F., Krebs, M., Waadt, R., Schumacher, K., Wu, W.-H., Hedrich, R. and Roelfsema, M. R. G. (2015). Cytosolic Ca2+ Signals Enhance the Vacuolar Ion Conductivity of Bulging Arabidopsis Root Hair Cells. *Molecular Plant*, 8:1665–1674.

War, A. R., Paulraj, M. G., Ahmad, T., Buhroo, A. A., Hussain, B., Ignacimuthu, S. and Sharma, H. C. (2012). Mechanisms of plant defense against insect herbivores. *Plant Signaling & Behavior*, 7:1306–1320.

Ward, J. M., Mäser, P. and Schroeder, J. I. (2009). Plant Ion Channels: Gene Families, Physiology, and Functional Genomics Analyses. *Annual review of physiology*, 71:59–82.

Ward, J. M. and Schroeder, J. I. (1994). Calcium-Activated K+ Channels and Calcium-Induced Calcium Release by Slow Vacuolar Ion Channels in Guard Cell Vacuoles Implicated in the Control of Stomatal Closure. *The Plant Cell*, 6:669–683.

Wardlaw, I. F. (1972). Responses of Plants to Environmental Stresses. J. Levitt. Academic Press, New York, 1972. xiv, 698 pp., illus. $32.50. Physiological Ecology. *Science*, 177:786–786.

Webb, A. A. R., McAinsh, M. R., Taylor, J. E. and Hetherington, A. M. (1996). Calcium Ions as Intracellular Second Messengers in Higher Plants. In J. A. Callow, editor, *Advances in Botanical Research*, volume 22, pages 45–96. Academic Press.

White, P. J. and Broadley, M. R. (2003). Calcium in Plants. *Annals of Botany*, 92:487–511.

Wolfram, S. (1984). Cellular automata as models of complexity. *Nature*, 311:419–424.

Woods, N. M., Cuthbertson, K. S. and Cobbold, P. H. (1986). Repetitive transient rises in cytoplasmic free calcium in hormone-stimulated hepatocytes. *Repetitive transient rises in cytoplasmic free calcium in hormone-stimulated hepatocytes. Nature*, 319:600–602.

Xiao, L., Carrillo, J., Siemann, E. and Ding, J. (2019). Herbivore-specific induction of indirect and direct defensive responses in leaves and roots. *AoB PLANTS*, 11.

Xiao, Y., Tian, Z., Yu, J., Zhang, Y., Liu, S., Du, S. and Lan, X. (2020). A review of object detection based on deep learning. *Multimedia Tools and Applications*, 79:23729–23791.

Xiong, T. C., Ronzier, E., Sanchez, F., Corratgé-faillie, C., Mazars, C. and Thibaud, J.-B. (2014). Imaging long distance propagating calcium signals in intact plant leaves with the BRET-based GFP-aequorin reporter. *Frontiers in Plant Science*, 5.

Yamaguchi-Shinozaki, K. and Shinozaki, K. (2006). Transcriptional Regulatory Networks in Cellular Responses and Tolerance to Dehydration and Cold Stresses. *Annual Review of Plant Biology*, page 26.

Yang, D.-L., Shi, Z., Bao, Y., Yan, J., Yang, Z., Yu, H., Li, Y., Gou, M., Wang, S., Zou, B., Xu, D., Ma, Z., Kim, J. and Hua, J. (2017). Calcium Pumps and Interacting BON1 Protein

Modulate Calcium Signature, Stomatal Closure, and Plant Immunity. *Plant Physiology*, 175:424–437.

Yang, T. and Poovaiah, B. (2003). Calcium/calmodulin-mediated signal network in plants. *Trends in Plant Science*, 8:505–512.

Yang, Z., Wang, C., Xue, Y., Liu, X., Chen, S., Song, C., Yang, Y. and Guo, Y. (2019). Calcium-activated 14-3-3 proteins as a molecular switch in salt stress tolerance. *Nature Communications*, 10:1199.

Yeats, T. H. and Rose, J. K. C. (2013). The Formation and Function of Plant Cuticles. *Plant Physiology*, 163:5–20.

Young, G. W. D. and Keizer, J. (1992). A single-pool inositol 1,4,5-trisphosphate-receptor-based model for agonist-stimulated oscillations in Ca2+ concentration. *Proceedings of the National Academy of Sciences*, 89:9895–9899.

Zhou, Z. and Neher, E. (1993). Mobile and immobile calcium buffers in bovine adrenal chromaffin cells. *The Journal of Physiology*, 469:245–273.

Zhu, F., Xi, D.-H., Yuan, S., Xu, F., Zhang, D.-W. and Lin, H.-H. (2014). Salicylic Acid and Jasmonic Acid Are Essential for Systemic Resistance Against Tobacco mosaic virus in Nicotiana benthamiana. *Molecular Plant-Microbe Interactions®*, 27:567–577.

Zhu, J.-K. (2016). Abiotic stress signaling and responses in plants. *Cell*, 167:313–324.

Zik, M., Arazi, T., Snedden, W. A. and Fromm, H. (1998). Two isoforms of glutamate decarboxylase in Arabidopsis are regulated by calcium/calmodulin and differ in organ distribution. *Plant Molecular Biology*, 37:967–975.

Zimmermann, M. R., Maischak, H., Mithöfer, A., Boland, W. and Felle, H. H. (2009). System Potentials, a Novel Electrical Long-Distance Apoplastic Signal in Plants, Induced by Wounding. *Plant Physiology*, 149:1593–1600.

Zipfel, C. (2014). Plant pattern-recognition receptors. *Trends in Immunology*, 35:345–351.

V Appendix

List of Figures

List of Tables

List of Abbreviations

ABA	abscisic acid
ABC transporter	ATP-binding cassette transporter
API	application programming interface
ATP	adenosine triphosphate
BAK1	LRR receptor kinase BAK1
C8	chitin polymer with molecular formula $(C_8H_{13}O_5N)_8$
Ca	calcium
Ca^{2+}	calcium ion
CA	cellular automaton
cAMP	cyclic adenosine monophosphate
CBL	calcineurin B-like protein
CICR	calcium-induced calcium release
CIPK	CBL-interacting protein kinase
Cl^-	chloride ion
COPASI	COmplex PAthway SImulator (modeling tool)
COR	cold-responsive gene
CoRC	COPASI R Connector (software tool)
CDPK	calcium-dependent protein kinase
CPK	calcium-dependent protein kinase (in *Arabidopsis thaliana*)
CPK1	calcium-dependent protein kinase 1
CPK3	calcium-dependent protein kinase 3
CPK6	calcium-dependent protein kinase 6
CPK21	calcium-dependent protein kinase 21
CPK23	calcium-dependent protein kinase 23
DIC	differential interference contrast
EF hand	binding site for calcium
flg22	bacterial peptide flagellin 22
GST	glutathione-S-transferase
H_2O_2	hydrogen peroxide
IP_3	inositol trisphosphate
IVK	in vitro kinase assay
LSODA	Livermore Solver for Ordinary Differential equations with Automatic switching for stiff and non-stiff problems
MWC model	Monod-Wyman-Changeux model
NaCl	sodium chloride
NADPH	reduced form of nicotinamide adenine dinucleotide phosphate
NT-SLAC1	N-terminal protein fragments of SLAC1
O_2^-	superoxide ion (reactive oxygen ion)
ODE	ordinary differential equation
OST1	open stomata 1 protein kinase
PDE	partial differential equation
PDF	portable document format (file format)
R	programming language R
RBOHD	respiratory burst oxidase homolog protein D
ROS	reactive oxygen species
SLAC1	guard cell S-type anion channel SLAC1

Kymograph data of stimulation with NaCl or flg22

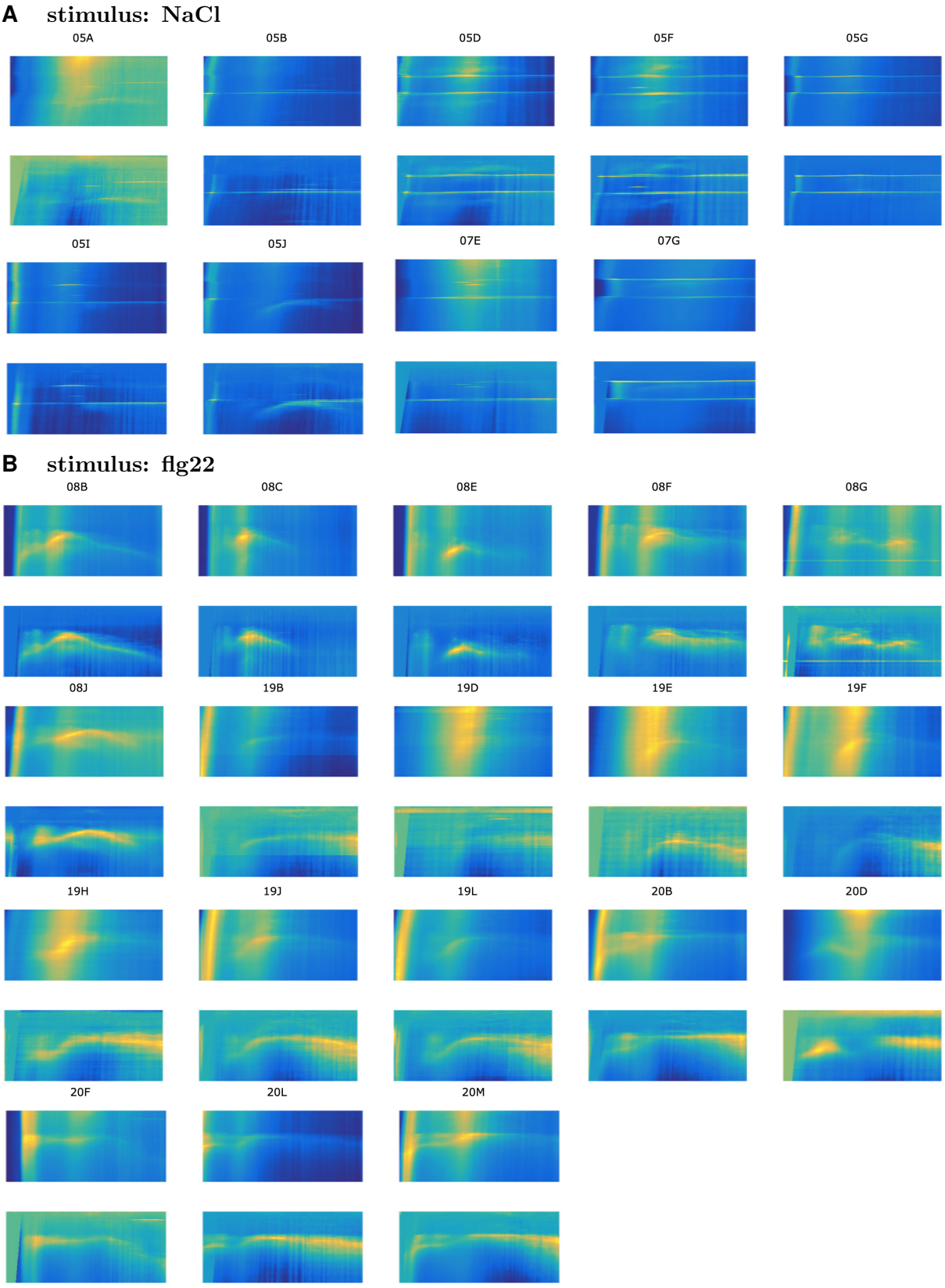

Figure 32. Kymograph data of stimulation experiments with NaCl (**A**) and flg22 (**B**). Panels in the lower row show normalized kymographs with respect to the base concentration before stimulation.